NAVAL POSTGRADUATE SCHOOL

MONTEREY, CALIFORNIA

THESIS

DESIGN AND ANALYSIS OF A MULTICOLOR QUANTUM WELL INFRARED PHOTODETECTOR

by

Fabio Durante Pereira Alves

September 2005

Thesis Advisors: Gamani Karunasiri
                                                    John Powers
                                                    Sherif Michael

Approved for public release; distribution is unlimited

THIS PAGE INTENTIONALLY LEFT BLANK

REPORT DOCUMENTATION PAGE	*Form Approved OMB No. 0704-0188*

Public reporting burden for this collection of information is estimated to average 1 hour per response, including the time for reviewing instruction, searching existing data sources, gathering and maintaining the data needed, and completing and reviewing the collection of information. Send comments regarding this burden estimate or any other aspect of this collection of information, including suggestions for reducing this burden, to Washington headquarters Services, Directorate for Information Operations and Reports, 1215 Jefferson Davis Highway, Suite 1204, Arlington, VA 22202-4302, and to the Office of Management and Budget, Paperwork Reduction Project (0704-0188) Washington DC 20503.

1. AGENCY USE ONLY *(Leave blank)*	**2. REPORT DATE** September 2005	**3. REPORT TYPE AND DATES COVERED** Master's Thesis	
4. TITLE AND SUBTITLE: Design and Analysis of a Multicolor Quantum Well Infrared Photodetector		**5. FUNDING NUMBERS**	
6. AUTHOR(S)			
7. PERFORMING ORGANIZATION NAME(S) AND ADDRESS(ES) Naval Postgraduate School Monterey, CA 93943-5000		**8. PERFORMING ORGANIZATION REPORT NUMBER**	
9. SPONSORING /MONITORING AGENCY NAME(S) AND ADDRESS(ES) N/A		**10. SPONSORING/MONITORING AGENCY REPORT NUMBER**	

11. SUPPLEMENTARY NOTES The views expressed in this thesis are those of the author and do not reflect the official policy or position of the Department of Defense or the U.S. Government.

12a. DISTRIBUTION / AVAILABILITY STATEMENT Approved for public release; distribution unlimited	**12b. DISTRIBUTION CODE**

13. ABSTRACT (maximum 200 words)

Recent military applications have demanded photodetectors with high sensitivity, high selectivity and multispectral capability for detection and identification of the target. These characteristics have been found in quantum well infrared photodetectors (QWIP). Driven by these applications, a QWIP photodetector capable of detecting simultaneously infrared emissions within near infrared (NIR), mid wavelength infrared (MWIR) and long wavelength infrared (LWIR) was studied, modeled, designed and characterized. Using the envelope function approximation, the mathematical model of the quantum phenomena in semiconductor heterostructures was derived. A computational tool was developed to solve self-consistently the Schodinger-Poisson equation using the shooting method, allowing the theoretical evaluation of the absorption coefficient. A three-color (NIR, MWIR and LWIR) GaAs-based QWIP sample and a two-color (NIR and MWIR) InP-based QWIP sample were designed, both comprised of stacks of uncoupled wells for each band detection. The 67 layers of the GaAs sample was grown using molecular beam epitaxy (MBE). Intersubband absorption in the sample was measured for the MWIR and LWIR using Fourier transform spectroscopy (FTIR) and the measured peak positions, found at 5.3 μm, 8.7 μm, and 13.8 μm are within 0.3 μm of the theoretical values, indicating that the model accurately predicts the absorption wavelengths. A two-dimensional ordered grating pattern was selected and optimized separately for both MWIR and LWIR desired peaks. Finally the photodetector device configurations were designed to permit to the measurement of the NIR band through photocurrent spectroscopy and performance analysis. The fabrication and characterization of the prototypes are a matter for future work.

14. SUBJECT TERMS Quantum Well, QWIP, Three-color detection, Infrared detection, Self-consistent Shrodinger-Poisson Solution, Absorption, FTIR.			**15. NUMBER OF PAGES** 117
			16. PRICE CODE
17. SECURITY CLASSIFICATION OF REPORT Unclassified	**18. SECURITY CLASSIFICATION OF THIS PAGE** Unclassified	**19. SECURITY CLASSIFICATION OF ABSTRACT** Unclassified	**20. LIMITATION OF ABSTRACT** UL

NSN 7540-01-280-5500

Standard Form 298 (Rev. 2-89)
Prescribed by ANSI Std. 239-18

THIS PAGE INTENTIONALLY LEFT BLANK

**DESIGN AND ANALYSIS OF A MULTICOLOR QUANTUM WELL INFRARED
PHOTODETECTOR**

Fabio Durante Pereira Alves
Major, Brazilian Air Force
B.S.E.E., Instituto Tecnologico de Aeronautica, 1997

Submitted in partial fulfillment of the
requirements for the degree of

**MASTER OF SCIENCE IN ELECTRICAL ENGINEERING
ELECTRICAL ENGINEER**

from the

**NAVAL POSTGRADUATE SCHOOL
September 2005**

Author: Fabio Durante Pereira Alves

Approved by: Gamani Karunasiri
Thesis Advisor

John Powers
Thesis Advisor

Sherif Michael
Thesis Advisor

Jeffrey B. Knorr
Chairman, Department of Electrical and Computer Engineering

iii

THIS PAGE INTENTIONALLY LEFT BLANK

ABSTRACT

Recent military applications have demanded photodetectors with high sensitivity, high selectivity and multispectral capability for detection and identification of the target. These characteristics have been found in quantum well infrared photodetectors (QWIP). Driven by these applications, a QWIP photodetector capable of detecting simultaneously infrared emissions within near infrared (NIR), mid wavelength infrared (MWIR) and long wavelength infrared (LWIR) was studied, modeled, designed and characterized. Using the envelope function approximation, the mathematical model of the quantum phenomena in semiconductor heterostructures was derived. A computational tool was developed to solve self-consistently the Schodinger-Poisson equation using the shooting method, allowing the theoretical evaluation of the absorption coefficient. A three-color (NIR, MWIR and LWIR) GaAs-based QWIP sample and a two-color (NIR and MWIR) InP-based QWIP sample were designed, both comprised of stacks of uncoupled wells for each band detection. The 67 layers of the GaAs sample was grown using molecular beam epitaxy (MBE). Intersubband absorption in the sample was measured for the MWIR and LWIR using Fourier transform spectroscopy (FTIR) and the measured peak positions, found at 5.3 μm, 8.7 μm, and 13.8 μm are within 0.3 μm of the theoretical values, indicating that the model accurately predicts the absorption wavelengths. A two-dimensional ordered grating pattern was selected and optimized separately for both MWIR and LWIR desired peaks. Finally the photodetector device configurations were designed to permit to the measurement of the NIR band through photocurrent spectroscopy and performance analysis. The fabrication and characterization of the prototypes are a matter for future work.

THIS PAGE INTENTIONALLY LEFT BLANK

TABLE OF CONTENTS

LIST OF FIGURES

LIST OF TABLES

THIS PAGE INTENTIONALLY LEFT BLANK

ACKNOWLEDGMENTS

THIS PAGE INTENTIONALLY LEFT BLANK

EXECUTIVE SUMMARY

Recent military applications have demanded photodetectors with high sensitivity, high selectivity and multispectral capability. Both mecrurium cadmiun telluride (HgCdTe) photodiodes and quantum well infrared photodetectors (QWIP) offer multi-color capability in the medium-wave IR (MWIR) and long-wave IR (LWIR) spectral regions. Each of these technologies has its advantages and disadvantages. However, the possibility to achieve multicolor detection, going from near infrared (NIR) to LWIR, is more likely to be obtained using QWIPs.

Driven by those applications, and in continuity of the work being conducted at the Sensor Research Laboratory (SRL) at the Naval Postgraduate School (NPS), QWIPs capable to detect simultaneously 3 different IR bands within the wavelengths intervals of $0.9 - 1.4$ μm, $3.8 - 5.0$ μm and $8.0 - 12.0$ μm were studied, modeled, and designed. The work was performed bounded by technological, financial and temporal limitations, aiming the fabrication of proof-of-concept QWIP prototypes to be investigated and optimized in future work.

When one semiconductor layer (well) is sandwiched between two layers of larger bandgap material (barriers), it forms a quantum well. The potential profile is defined by the bands offset, allowing the existence of the quantized energy levels, confined inside the wells, while continuum states are possible outside. When a quantum well photodetector is exposed to an incident photon flux, transitions between quantized energy levels can occur. The photon flux can be sensed when bias is applied to the structure and the transitions allow the extraction of the electrons from the well, to the barrier regions leading to a photocurrent.

The semiconductor material properties along with their availability were considered and two main material groups were selected to be used. GaAs/AlGaAs/InGaAs systems proved easy in growth and fabrication while InP/AlGaAs/AlInAs systems were capable of meeting the requirements for detecting the desired NIR band. A configuration of

three uncoupled quantum wells stacks, one stack for each band, placed between highly doped contact layers, proved to be more suitable to allow separate readouts of the signals.

To be able to estimate the QWIPs' absorption the quantized energy levels inside the wells as well as their respective wavefunctions were computed self-consistently solving the Schrodinger-Poisson equation numerically for the structures. The shooting method was used due to its ability to handle any potential profile making the design more flexible. Finally, a GaAs-based sample for three-color detection, and a InP-based sample for two-color detection were designed, taking into account the limitations on each configuration.

The GaAs sample was fabricated using MBE and the absorption measurements are presented in the fourth chapter. An FTIR spectrometer was used to measure the room temperature absorptance of the MWIR and LWIR bands, and the sample showed absorption in good agreement with the theoretical predictions. Also the heavily doped contact layers introduced a second LWIR absorption band. The measured peaks, $5.3\ \mu m$, $8.7\ \mu m$ and $13.8\ \mu m$, varied less than $0.3\ \mu m$ from the predicted values, mostly due to the uncertainties in the material parameters.

The optical coupling structure was than designed to allow detection of normal incident radiation. A bi-dimensional ordered grating pattern was selected and optimized separately for both MWIR and LWIR desired peaks. Constraints in mask fabrication and wafer processing forced the degradation of the grating performance, to make it feasible. Finally the photodetector device configurations were designed, to permit to performance analysis. The fabrication and characterization of the prototypes are matter for future work.

Despite the financial, temporal and technological limitations, normally present in any research, the objective of this thesis was successfully accomplished. However, further work needs to be done to finalize the devices' fabrication and testing and to improve the mathematical models and the numerical algorithms to be able develop optimal detectors.

I.   INTRODUCTION

Infrared guided weapons have proved to be indispensable in any modern battle-field. Statistics and analysis have shown that the capability to detect and identify the enemy platforms' IR signatures as well as the ability to negate ones own are a significant factors of success in most tactical combat environments [1]. In this scenario, the IR countermeasures play an important role. By emulating the sought platform IR signature and seducing the IR guided weapon, it is possible to reduce significantly the target risk. Modern countermeasures have the capability to produce signatures very close to the target's emissions. Consequently, to be able to distinguish between countermeasure and target, the weapon seeker must have not only high sensitivity but also high selectivity combined with multispectral detection capability.

Systems that gather data in separate IR spectral bands can discriminate both absolute temperature and unique signatures of the target, necessary to distinguish it from the countermeasure. In addition, the imaging capability of the focal plane arrays (FPA) has been explored in the newest generation of seekers, making the weapons even harder to counter.

This combination has been achieved until recently using conventional infrared photodetectors and extensive postprocessing computational efforts [2]. Furthermore, multispectral systems rely on complicated optical techniques that either disperse the optical signal across multiple IR FPAs or use filter wheels to spectrally discriminate the image focused on a single FPA [3]. In addition, beam splitters, lenses, optical bandpass filters as well as a complex alignment configuration are required, making these approaches expensive in size, complexity and cooling requirements.

Currently, both mecrurium cadmiun telluride (HgCdTe) photodiodes and quantum well infrared photodetectors (QWIP) offer multicolor capability in the medium-wave IR (MWIR) and long-wave IR (LWIR) spectral regions. Each of these technologies has its advantages and disadvantages, detailed in Ref. [4]. However, the possibility to achieve multicolor detection, going from near infrared (NIR) to LWIR, is more likely to be obtained using QWIPs.

A.   QUANTUM WELL INFRARED PHOTODETECTORS

The ability to sense optically driven transitions between two quantized energy levels is the origin of the photodetection in quantum well photodetectors. Conventional interband optical absorption involves photoexiting carriers across the bandgap. Since the incident photon energy is greater than the bandgap, both electrons and holes can be created in the semiconductor. In a detector, these carriers are collected, thereby producing a photocurrent. By controlling the bandgap energy, selecting the desired material and controlling the alloy composition, the spectrum of the absorption can be tailored. [5]

In 1969 L. Esaki and R. Tsu [6] started the investigation of the idea that a periodic variation on of the alloy composition or of impurity density introduced during epitaxial growth could create a periodic potential or superlattice, in monocrystalline semiconductors. This structure is responsible for the formation of subbands in both the valence and conduction bands. In consequence, intersubband optical absorptions are possible in quantum well photodetectors, permitting the utilization of large bandgap materials to detect long wavelength infrared radiation. Beyond that, in quantum wells, both interband and intersubband absorption are possible to be detected allowing: monolithically integrated multi spectral detection from NIR to LWIR, very high speed, and narrow and tunable band detection. Most of those characteristics, necessary for the application in discussion, are difficult to be achieved with conventional photodetectors [4].

Several studies and experiments were conducted since Esaki's paper confirming the feasibility of practical devices using this concept. The first quantum well laser [7] was reported in 1975; the first successful fabrication of a high electron mobility transistor (HEMT) [8] was reported in 1980. Finally in 1987 B. F. Levine *et al.* published the experimental results of the first working QWIP [9]. The device was a periodic repetition of AlGaAs/GaAs and based in conduction band bound-to-bound transitions. In the following years, various configurations have been tested with great improvement in the detection characteristics, reaching the state of art with the first 640x512 pixel four-band QWIP FPA camera, described in detail in [10].

In 2002, a series of investigations in dual color and band-tunable QWIPs started to be conducted at the Sensor Research Laboratory (SRL) at the Naval Postgraduate

School (NPS). The results, published in [11], [12], [13], [14], and [15], showed the potential of these devices in military applications. The unique characteristic of the SRL work is the inclusion of the NIR band in its QWIPS, using interband transitions in asymmetric quantum wells. Currently the research has reached a stage that demands more elaborated numerical models, devices capable of detecting normal incident IR radiation and more than two bands of military interest monolithically detected.

B. PURPOSE AND ORGANIZATION OF THIS THESIS

Driven by those applications, and in continuity of the work being conducted at the SRL, *the purpose of this thesis was to study, to model, and to design a QWIP capable to detect 3 different IR bands within the wavelengths intervals of 0.9 - 1.4* μm*, 3.8 - 5.0* μm *and 8.0 - 12.0* μm. The work was performed bounded by technological, financial and temporal limitations, aiming at the fabrication of proof-of-concept QWIP prototypes to be investigated and optimized in future work.

In order to document the conducted research work, this thesis is organized as follows. This chapter elucidates the motivation of this work as well as gives a brief introduction of the research realm of QWIPs. A short description of the organization of the document is also presented.

The second chapter explores the physics of the semiconductor heterostructures and quantum wells. The envelope function approximation is described along with the one-dimensional potential solutions of the Schrodinger's equation. The density of states and the charge distribution potential are analyzed providing a theoretical background to understand the transitions between quantized energy levels within the hetereostructures. The possible quantum well transitions are analyzed and used to derive the absorption coefficient in all cases of interest of this work. The chapter ends by providing the necessary background information to be employed in designing issues. The mathematical models of the main figures of merit, such as absorption spectra, quantum efficiency, responsivity, dark current, and detectivity are also discussed.

The third chapter is the core of the document and starts with the initial design considerations. The basic device configuration is defined based on the material analysis,

limitations, and constraints, as well as the desired detection conditions, light coupling and restrictions on the bands. A specific numerical model that mathematically describes the quantum well structures, predicts the absorption line shapes and helps to design band-specific photodetectors is developed, based on the self-consistent Schrodinger-Poisson solutions.

The fourth chapter presents the experimental results. Absorptance measurements using Fourier transform infrared spectroscopy of the molecular beam epitaxially (MBE) grown wafer are presented and compared with the estimated values. The analysis and conclusions are shown and the possible future improvement and optimization are discussed. Sequentially, the optical coupling is analyzed and a two-dimensional grating structure is designed to couple the desired IR bands. The final device structure, as well as several photodetector configurations, are designed to meet the standards and rules of fabrication. The layout of the masks is finalized in accordance with the processes and budget restrictions.

The conclusive chapter summarizes the research work, discussing the main assumptions, along with the technological, temporal and financial limitations faced during the thesis work period. Also the lessons learned are addressed. The chapter ends pointing the scientific contribution of the work and identifying the most important needs of improvement and continuity of the research.

II. QUANTUM WELL INFRARED PHOTODETECTORS PHYSICS

The understanding of the physical concepts involved in IR photodetection by quantum well devices lies in the quantum physics realm, as the name suggests. The ability to control such phenomena requires the capability to mathematically model quantum effects caused by semiconductor structures and its interacting fields. This chapter provides the theoretical background necessary to physically understand and practically design QWIPs through the manipulation of the mathematical models.

Initially, the one-dimensional potential present in heterostrucures is described by Schordinger's equation, along with the concepts necessary to understand how quantum well devices absorb IR and how to evaluate and predict such absorption. After that, QWIPs are described and their figure of merit are derived to permit predicting and analyzing their performances.

A. SEMICONDUCTOR HETEROSTRUCTURES

One of the most important characteristics of semiconductors is the existence of forbidden energy bands, responsible for separating the electrons in the highly populated valence band from those in the poorly populated conduction band. The energy gap and bands are determined by the periodic potential of the crystalline material. When one semiconductor layer is grown on top to the other, a heterojunction is formed. This can be obtained using selected semiconductors with compatible crystal structures and lattice spacings. Using modern techniques such as Molecular Beam Epitaxy (MBE) and Metal Organic Chemical Vapor Deposition (MOCVD), under carefully controlled conditions, the compositional transition between two materials can be made almost perfectly abrupt with the heterointerfaces being defined on a monolayer scale. [16]

Away from the heterojunction, the electrons are subjected to the bulk properties of each material. At the heterojunction, the potential changes abruptly from one material to the other. Moreover, a transfer of electrical charge occurs over the scale of a few atomic layers near the interface. This redistribution of charges creates an interface dipole

responsible for a sharp jump in the electrostatic potential that is superimposed to the crystalline potential. On each side, the electrons take on the characteristics of the constituent semiconductors. The relative positions of the bands, however, are considered, from a macroscopic viewpoint, as a discontinuity or "offset" in the valence and conduction bands, that depends uniquely on the pair of materials forming the heterojunction. [5]

In terms of the band discontinuities three types of structures are possible, classified into four groups [16]: type I, type II-misaligned, type II-staggered, and type III. Type I occurs when the entire gap of the small bandgap semiconductor resides within the conduction and valence bands of the large bandgap material. Type II, alternatively, occurs when one (staggered) or both (misaligned) band offsets are larger than the difference between the semiconductors bandgaps. Finally, type III occurs when the heterojunction is formed by one semiconductor with positive bandgap and the other with a negative bandgap. The last behaves like semimetals, since the conduction and valence bands overlap.

Taking into account the bulk properties of the semiconductors, it is possible to create virtually any potential profile along the crystal growth direction, by depositing sequences of different materials. Limitations such as the material availability and their capability to be grown epitaxially as well as the difference in lattice constants must be considered in any design. In the rest of the chapter a detailed discussion on the electron states in heterostructures is presented.

1. Envelope Function Approximation

The electron wavefunctions in a heterostructure can be described using the envelope function approximation, as described in Ref. [5].

A semiconductor heterostructure can be considered as possessing a periodic potential $V_c(\mathbf{r})$, due to the crystal lattice, and a slowly varying electrostatic potential $V_e(\mathbf{r})$ due to different layers of the heterojunction. Here $\mathbf{r}$ represents the position vector. The Hamiltonian for an electron, given this combination of potentials can be written as [5]:

$$H = \frac{p^2}{2m_0} + V_c(\mathbf{r}) + V_e(\mathbf{r}). \tag{2.1}$$

The momentum operator p is described as

$$p = \frac{\hbar}{i}\left[\frac{\partial}{\partial x}, \frac{\partial}{\partial y}, \frac{\partial}{\partial z}\right],$$

(2.2)

where $\hbar$ is the Plank constant h divided by 2π and i is the imaginary unit. Along with some very demanding algebra, some physically consistent approximations [5] can be made under the assumption that the electron in the nth band is therefore a particle possessing effective mass associated with the nth band and subjected to a potential $V_e(\mathbf{r})$. Furthermore, considering that influence of the periodic potential $V_c(\mathbf{r})$ is taken into account through the effective mass m^*_n and the energy E_{n0} of the nth band at $\mathbf{k} = 0$ ($\mathbf{k}$ being the crystal momentum), the Schrodinger's equation for the envelope function can be written as [5]:

$$H\Psi_n(\mathbf{r}) = (E - E_{n0})\Psi_n(\mathbf{r}).$$

(2.3)

Here, H is the Hamiltonian described by Equation (2.1) (replacing m_0 by the effective mass) and E represents the energy eingenstates of the wavefunction Ψ_n. The full wavefunction can be written as [5]

$$\Psi_n \cong \psi_n(\mathbf{r})u_{n0}(\mathbf{r}),$$

(2.4)

where ψ_n is the envelope function, and u_{n0} is the Bloch function possessing the periodicity of the lattice. When the electrostatic potential is zero, the solution is [5]

$$\Psi_n \cong \frac{1}{\sqrt{\Omega}}e^{i\mathbf{k}\cdot\mathbf{r}}u_{n0}(\mathbf{r}),$$

(2.5)

where Ω is the crystal volume.

Further simplifications are possible, taking into account the one-dimensional characteristic of the heterostructure potential $V_e(\mathbf{r})$ and the effective mass along the growth axis z. Consequently the envelope function can be written in the form [5]

$$\psi(\mathbf{r}) = \psi(z)e^{i\mathbf{K}\cdot\mathbf{\rho}}.$$

(2.6)

It is important to distinguish between **r** (that is the 3-D position vector) and **ρ** (that is the 2-D position vector in the *x-y* plane). Also, while **k** represents the 3-D crystal momentum, **K** is the 2-D representation of the momentum in the *x-y* plane.

The *z* component of the envelope function satisfies [17]

$$-\frac{\hbar^2}{2m^*(z)}\frac{d^2}{dz^2}\psi(z)+V(z)\psi(z)=E\psi(z).\tag{2.7}$$

To obtain the stationary states of an electron in the heterostructure, it is necessary to solve Equation (2.7) in each layer, considering the properties of each component separately and to join the solutions at the interfaces [17]. First, the wavefunctions must be continuous at the interface. Mathematically,

$$\psi(z_i^-)=\psi(z_i^+),\tag{2.8}$$

where z_i represents the *z* coordinate of the *i*th interface and the (±) sign refers to the materials on the right and left of the heterojunction. Second, the solution must conserve the probability flux which crosses the interface. This requirement is satisfied when [18]

$$\frac{1}{m^-}\frac{\partial}{\partial z}\psi(z_i^-)=\frac{1}{m^+}\frac{\partial}{\partial z}\psi(z_i^+),\tag{2.9}$$

Finally, the probability interpretation of the wavefunction [17] requires the normalization condition for the bound states potential. Mathematically,

$$\int_{-\infty}^{\infty}\psi^*(z)\psi(z)\,dz=1,\tag{2.10}$$

where (*) represents the complex conjugate.

Some important constrains of this formalism must be mentioned [18]. First, the effective mass was assumed to not depend on **k**, meaning a perfect parabolic band. When the discontinuities in *V(z)* are significant, a correction accounting for band nonparabolicity must be applied. This can be done using the expression [19]

$$m^*(z)=m_p^*(z)\big(1+\beta\big(E-V_e(z)\big)\big),\tag{2.11}$$

where $m_p*(z)$ is the "parabolic" band effective mass profile and β is given by [19]:

$$\beta = \left(1 - \frac{m*(z)}{m_0}\right)^2 \frac{1}{E_g(z)}.$$ (2.12)

Here, m_0 is the electron rest mass and $E_g(z)$ is the bandgap profile along the heterostructure. Second, all parameters characterizing the band structure are temperature dependent This dependence can be modeled by the Varshini equation [19]:

$$E_g(T) = E_{g0} - \frac{\alpha_{tmp}T^2}{T + \beta_{tmp}}$$ (2.13)

where E_{g0} is the bandgap at $T = 0$, and α_{tmp} and β_{tmp} are adjustable Varshini parameters that can be found for several semiconductors compounds in [20].

Finally, the strain placed on the material by growing layers with different lattice constants on top of each other also affects the band structure. This allows an additional degree of freedom in designing heterostructure devices. For lattice-mismatched epitaxial growth on a (001) substrate, the strain tensor is given by [21]

$$\varepsilon_{xx} = \varepsilon_{yy} = \frac{a_S}{a_L} - 1$$

$$\varepsilon_{zz} = -\frac{2c_{12}}{c_{11}},$$ (2.14)

where a_S and a_L stand for the lattice constants of the substrate and the strained layer, respectively, and c_{12} and c_{11} are elastic constants for crystals with cubic cells under small deformations. All off-diagonal terms are zero in this case. Therefore, applying the deformation potential theory, it is possible to compute the bandgap shift [21]. For III-V materials, due to the nature of the atomic bonding, the bandgap increases for compressive strain and the change is given by [20]

$$\delta E_g = (a_v + a_c)(\varepsilon_{xx} + \varepsilon_{yy} + \varepsilon_{zz}),$$ (2.15)

where a_v and a_c are the empirical deformation potentials, also given in [20].

Rigorously, the assumptions made until now cannot be applied to the valence bands that are degenerate with respect to the heavy and light hole bands. A formal treatment for the valence subbands can be found in [21] and the envelope function approximation using a 4x4 **k·p** Hamiltonian approximation can be compiled as

$$
\begin{bmatrix}
P+Q & L & M & 0 \\
L^{\dagger} & P-Q & 0 & M \\
M^{\dagger} & 0 & P-Q & -L \\
0 & M^{\dagger} & -L^{\dagger} & P+Q
\end{bmatrix}
\begin{bmatrix}
\psi^{v1}(\mathbf{k}) \\
\psi^{v2}(\mathbf{k}) \\
\psi^{v3}(\mathbf{k}) \\
\psi^{v4}(\mathbf{k})
\end{bmatrix}
= E(\mathbf{k})
\begin{bmatrix}
\psi^{v1}(\mathbf{k}) \\
\psi^{v2}(\mathbf{k}) \\
\psi^{v3}(\mathbf{k}) \\
\psi^{v4}(\mathbf{k})
\end{bmatrix},
\qquad (2.16)
$$

where ψ^{vi} is the envelope wavefunction of the holes under the spin symmetry specified as follows: $v1$ and $v4$ represents the $|3/2, \pm 3/2\rangle$ heavy hole spin states, and $v2$ and $v3$ represents the $|3/2, \pm 1/2\rangle$ light hole spin states. The symbol (†) stands for adjoint, and the matrix elements are given by [21]:

$$
P = \frac{\hbar^2 \gamma_1(z)}{2m_0}(k_x^2 + k_y^2) - \frac{\hbar^2}{2m_0}\frac{d}{dz}\gamma_1(z)\frac{d}{dz} + V_e(z),
\qquad (2.17)
$$

$$
Q = \frac{\hbar^2 \gamma_2(z)}{2m_0}(k_x^2 + k_y^2) + \frac{\hbar^2}{2m_0}\frac{d}{dz}\gamma_1(z)\frac{d}{dz} + V_e(z),
\qquad (2.18)
$$

$$
L = -\frac{\hbar^2 \sqrt{3}}{2m_0}(k_x - ik_y)\left[\gamma_3(z)\frac{d}{dz} + \frac{d}{dz}\gamma_3(z)\right],
\qquad (2.19)
$$

and

$$
M = \frac{\hbar^2 \sqrt{3}}{4m_0}[(\gamma_2(z) - \gamma_3(z)](k_x - ik_y)^2.
\qquad (2.20)
$$

All parameters in the previous expressions were defined before except for the "Luttinger parameters", γ_i, that can be found, for several III-V compound semiconductors and their alloys, in [20]. It is important to mention that the z dependence of γ_i and V is due the material change along the growth axis.

For practical applications, further simplifications are acceptable. The most common is to consider the valence band represented by two parabolic bands, one for the

heavy holes with effective mass $m_{hh}{}^* < 0$, and other for the light holes with effective

mass $m_{lh}{}^* < 0$. The well potential is then a confining potential for holes and the same

model used for electrons in the conduction band becomes applicable.

In a more practical sense, a heterostructure can be grown to create potential wells, with electrooptical proprieties that can be customized for a wide variety of applications. This practice is commonly called "quantum engineering" or "bandgap engineering".

2.   Quantum Wells

When one thin semiconductor layer (well) is sandwiched between two layers of larger bandgap material (barriers), it forms a quantum well. As mentioned in the previous section, the potential profile is defined by the bands offsets, allowing the existence of the quantized energy levels, confined inside the wells, while continuum states are possible outside. Such structures allow the exploration of quantum effects that have become very useful in optoelectronic devices. [5]

A schematic representation of the electrostatic potential of a structure comprised of multiple quantum wells is shown in Figure 1. The barriers and wells are highlighted with bandgaps, E_{gB} and E_{gW}, respectively. The other parameters in Figure 1 include valence and conduction band offsets, *VBO* and *CBO*, respectively; and the valence and conduction bands confined energy levels E_{vi} and E_{ci}, respectively.
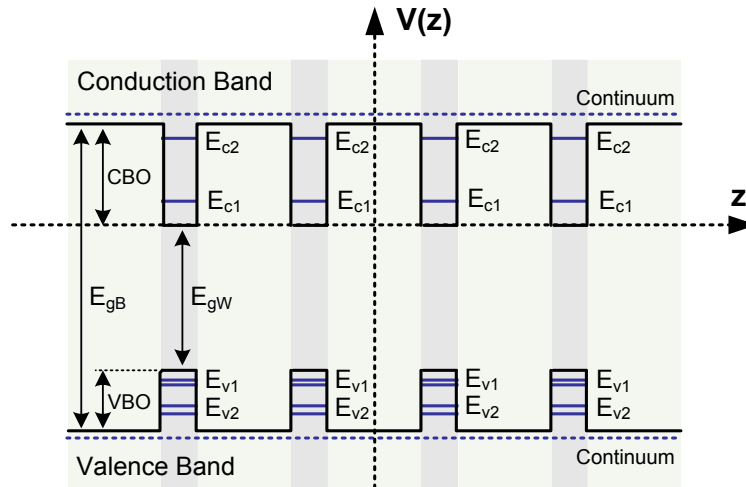
Figure 1   Schematic diagram of a heterostructure potential profile $V_e(z)$ (dark continuous line).

11

The ability to explore this structure as a device requires knowledge of the involved physical phenomena through mathematical models. The behavior of the carriers inside the heterostructure can be described by the Schrodinger's equation along with the appropriate boundary conditions. Complementarily, the concepts of: density of states; subbands population; charge distribution potential; transition rates; and effects of external fields; among others, have to be elaborated in order to allow practical comprehension and required control in designing procedures.

Therefore, the efforts from now on are focused in describing mathematically the most important characteristics of quantum wells, considering their suitability to act as photodetectors.

3.   Schrodinger's Equation Solutions

For the sake of simplicity, we consider, initially, an electron in a conduction band. A schematic diagram of an *N*-layer multiple quantum well structure is shown in Figure 2.
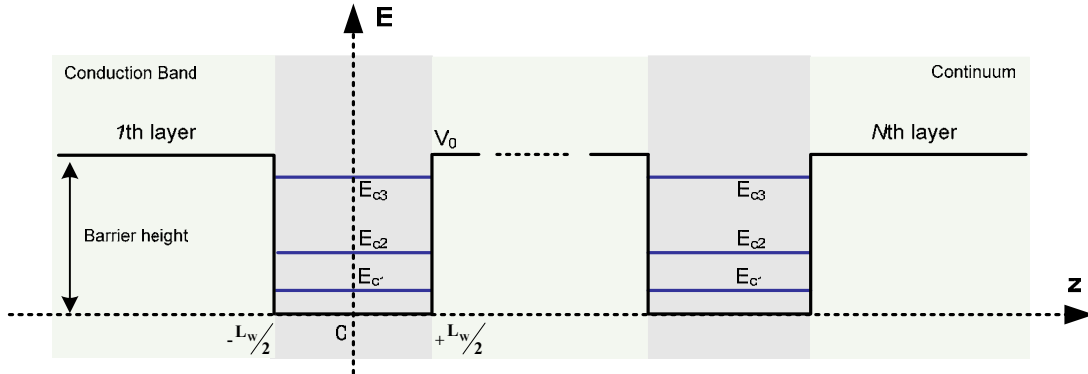
Figure 2   Conduction Band schematics diagram of an *N*-layer structure. The well width is L_W.

The general solution of the Shrodinger equation for the *n*th layer can be written as

$$\psi_n = A_n e^{ik_n z} + B_n e^{-ik_n z} \tag{2.21}$$

where

$$k_n(E) = \sqrt{\frac{2m_n*(E - V_n)}{\hbar^2}} \ . \tag{2.22}$$

The coefficients, A_n and B_n, can be evaluated applying the boundary conditions described by Equations (2.8) and (2.9), leading to the matrix form

$$\begin{bmatrix} A_n \\ B_n \end{bmatrix} = \tilde{M}_n \begin{bmatrix} A_{n+1} \\ B_{n+1} \end{bmatrix}, \tag{2.23}$$

where

$$\tilde{M}_n = \frac{1}{2}\begin{bmatrix} (1+\gamma_n)e^{i(k_{n-1}-k_n)z_n} & (1-\gamma_n)e^{-i(k_{n-1}+k_n)z_n} \\ (1-\gamma_n)e^{i(k_{n-1}+k_n)z_n} & (1+\gamma_n)e^{-i(k_{n-1}-k_n)z_n} \end{bmatrix}, \tag{2.24}$$

and

$$\gamma_n = \frac{m_n * k_{n+1}}{m_{n+1} * k_n}. \tag{2.25}$$

Here, if the structure contains N layers, the coefficients of the first and last layers are re-lated by

$$\begin{bmatrix} A_1 \\ B_1 \end{bmatrix} = \tilde{M}_1^{-1}\tilde{M}_2^{-1}...\tilde{M}_{N-1}^{-1}\tilde{M}_N \begin{bmatrix} A_N \\ B_N \end{bmatrix}, \tag{2.26}$$

where the interior product turns out a 4-by-4 matrix $\tilde{M}$. The wavefunction normalization condition expressed in Equation (2.10) further demands that $\psi(z) \to 0$ and $\partial\psi(z)/\partial z \to 0$, as $z \to \pm\infty$ for bound states. Therefore, since the two outer layers are barriers, and for $E < V_0$, the coefficients B_1 and A_N must be zero. Thus, Equation (2.26) can be rewritten as

$$\begin{bmatrix} A_1 \\ 0 \end{bmatrix} = \begin{bmatrix} m_{11} & m_{12} \\ m_{21} & m_{22} \end{bmatrix}\begin{bmatrix} 0 \\ B_N \end{bmatrix}. \tag{2.27}$$

To evaluate the confined energy states it is necessary to solve, numerically, the equation

$$m_{22}(E) = 0. \tag{2.28}$$

Finally, the wavefunctions can be obtained making $B_N = 1$, for example, and solving se-quentially, for each layer, Equation (2.23).

For $E > V_0$, the structure admits delocalized states where the electron can take on any value of positive energy, forming a continuum state. Since the states are not bound any more, the normalization of the wavefunction becomes a problem. A simple technique to overcome that is described later in this chapter.

This approach is called the Transfer Matrix Method [22]. Despite its simplicity, it has proven to be a powerful tool to handle structures with multiple layers. The confined states as well as their respective wavefunctions are depicted in Figure 3 for a single-well structure.
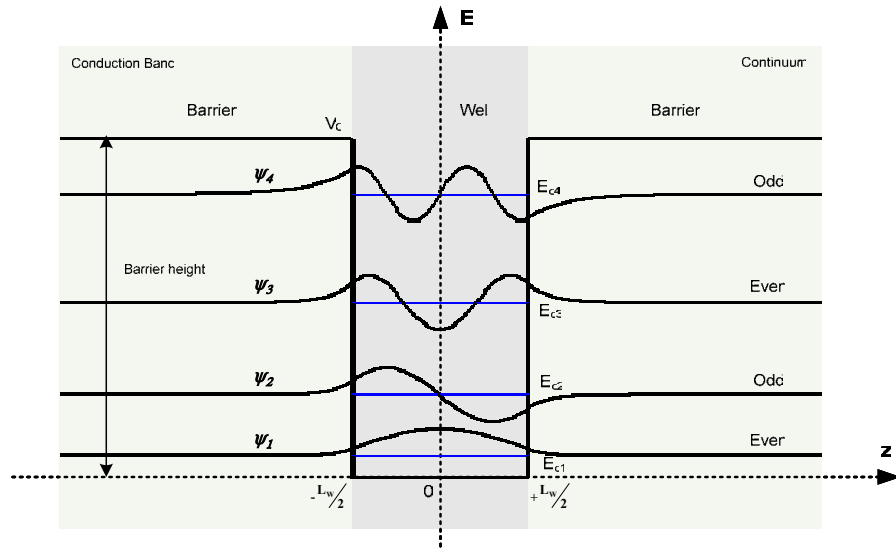
Figure 3   Confined energy states and respective wavefunctions in a single square well.

It is proved [17] that, for symmetric structures like the well in the Figure 3, the wavefunctions are mutually orthogonal, in the sense that

$$\int \psi_n(z)^* \psi_m(z)\, dz = 0 \tag{2.29}$$

whenever $n \neq m$. This result is a key point to establish the electron transition rules.

When the structure *barrier/well/barrier* is periodically repeated, and the carrier de Broglie wavelength is of the order of the barrier thickness, an energy miniband is formed. Thus, the wavefunctions of individual wells tend to overlap due to tunneling. Such configurations are interesting to broaden the absorption spectra as well as allowing photovoltaic detection [23]. Nevertheless, when the barriers are thick (greater than 200Å,

14

in most cases), the wells in the superlattice are uncoupled and the structure exhibits the individual wells with discrete energy levels [21]. This is the case of interest in this work and all treatment onward considers this configuration.

4. Density of States and Subband Populations

To be able to map the distribution of energy and momentum of electrons in a quantum well, it is necessary, first of all, to determine the density of states. Using a two-dimensional electron gas model due to the characteristic of the structure, the density of states of a single subband per unit area ($J^{-1}m^{-2}$) is given by [18]:

$$\rho^{2D}(E) = \frac{m_e^*}{\pi \hbar^2} . \tag{2.30}$$

If there are n confined states within the quantum well, then the density of states at a particular energy is the sum over all subbands below that point and can be written as

$$\rho^{2D}(E) = \sum_{i=1}^{n} \frac{m_e^*}{\pi \hbar^2} \Theta(E - E_i) \tag{2.31}$$

where Θ is the step unit function.

The surface density of carriers in a subband is given by [18]

$$n_n = \int_{subband} f^{FD}(E) \rho^{2D}(E) \, dE , \tag{2.32}$$

where f^{FD} (Fermi Dirac statistics) is the probability of occupation [19]

$$f^{FD}(E) = \frac{1}{1 + e^{\frac{E - E_F}{k_B T}}} . \tag{2.33}$$

Here, E_F represents a quasi-Fermi level which describes the carrier population within a subband. Evaluation of Equation (2.32) gives [5]

$$n_n = \frac{m_e^* k_B T}{\pi \hbar^2} \ln \left[1 + e^{\frac{E_F - E_n}{k_B T}} \right]. \tag{2.34}$$

15

The total electron density in a system is obtained by summing the densities of all subbbands.

In practice, a good approximation is to deduce the number of carriers directly from the doping densities in the well layer or the surrounding barrier layers. This allows the evaluation of the quasi-Fermi energy, the only unknown in Equation (2.34).

This concept is quite important and necessary to determine the band bending caused by potential due to the charge distribution.

5. Charge Distribution Potential

In practical devices, the doping concentration can be high enough to give rise to a significant additional potential on top of the usual band-offsets. In this case, it becomes necessary to solve the electrostatics that describes the system. In quantum well structures it is reasonable to assume the charge density given by the doping density of the well and/or surrounding layers. In a n-doped quantum well structure, the electrons are trapped in the well layer, where the potential energy is the lowest, making this region negatively charged. Consequently the left and right barriers become positively charged. The additional potential, $V_\rho(z)$, arising form this charge distribution, ρ, can be derived using Poisson's Equation [24]

$$\nabla^2 V_\rho = \frac{-\rho}{\varepsilon},$$

(2.35)

where ε is the permittivity of the material. The solution can be obtained determining the electric field strength. The potential and the electric field are related by

$$V_\rho(z) = -\int_{-\infty}^{z} \mathbf{E} \cdot dz.$$

(2.36)

Here, the one-dimensional characteristic of the bandedge potential imposes the one-dimensional charge distribution.

In a doped semiconductor, there are basically two contributions to the charge density, the ionized impurities and the free carriers. While the former can be obtained from

the doping density profile, $d(z)$, the latter can be computed from the probability distributions of the carriers at the heterostructure, $\psi_i{}^*(z)\psi_i(z)$. Thus, the charge density can be expressed as

$$\rho(z) = q\left[N\psi^*(z)\psi(z) - d(z)\right], \tag{2.37}$$

where q is the charge on the extrinsic carriers and N is the total number of carriers. Furthermore, the volumetric charge density $\rho(z)$ can be considered as an surface charge density $\sigma(z)$ with infinitesimal thickness δz. This can be expressed mathematically as:

$$\sigma(z)\delta z = \rho(z). \tag{2.38}$$

When more than one subband is populated, then the contribution to the charge density must be summed over the relevant subbands, resulting in

$$\sigma(z) = q\left[\sum_{i=1}^{n} N_i\psi_i{}^*(z)\psi_i(z) - d(z)\right]\delta z. \tag{2.39}$$

Since in most of the cases the dimensions in the x-y plane are much greater than the z direction, the x-y plane can be considered an infinite uniform charge distribution. Thus, the electric field at z can be written as [18]

$$\mathbf{E}(z) = \sum_{z'=-\infty}^{\infty} \frac{\sigma(z')}{2\varepsilon}\mathrm{sign}(z - z'). \tag{2.40}$$

In Equation (2.40), the summation represents the contribution of each surface density slice to the electric field at the position z. The function "sign" is defined as

$$\mathrm{sign}(z) = \begin{cases} +1 & \text{for } z \geq 0 \\ -1 & \text{for } z < 0, \end{cases} \tag{2.41}$$

and was introduced to account on charge neutrality along the structure.

At this point, all parameters are in place to allow the evaluation of $V_\rho(z)$, given by Equation (2.36). However it should be noticed that the wavefunctions are needed to obtain the density of electrons. This recursive problem can be solved using the so called "Self-Consistent Schrodinger-Poisson Solution." This method is detailed described in the next chapter.

17

6.   Transitions

Transitions between different states in a quantum well can occur in many ways. Nonetheless, two kinds of transitions, caused by a time-varying electromagnetic perturbation, are of interest of this work: an interband transition, in which an electron in the valence subband can be exited to the conduction subband, and an intersubband transition, in which an electron moves from one subband to another while remaining in the same band (conduction or valence). In both cases, depending on the structure characteristic, transitions can occur from a confined state to a continuum state. All four possibilities are discussed in this section.

In the general sense, the transition rate from initial a state represented by $\Psi_{i\mathbf{K}_i}$ to final states represented by $\Psi_{f\mathbf{K}_f}$, due to an interaction potential, V_p, can be calculated using Fermi's golden rule [5]

$$W\left(\Psi_{i\mathbf{K}_i} \to \Psi_{f\mathbf{K}_f}\right) = \frac{2\pi}{\hbar}\left|\left\langle \Psi_{f\mathbf{K}_f}\left|V_p\right|\Psi_{i\mathbf{K}_i}\right\rangle\right|^2 \delta\left(E_{f\mathbf{K}_f} - E_{i\mathbf{K}_i} - \hbar\omega\right). \qquad (2.42)$$

In Equation (2.42), $\hbar\omega$ is the incident photon energy, and the delta function accounts for conservation of energy. The interaction potential, under the dipole approximation, can be written as [25]

$$V_p = \frac{q}{m_e*}\left(\frac{I\hbar}{2\varepsilon_0 n_r \omega c}\right)^{1/2} \hat{\mathbf{e}}\cdot\mathbf{p}e^{i\mathbf{s}\cdot\mathbf{r}}, \qquad (2.43)$$

where q is the electron charge, I is the incident photon flux, c is the speed of light, n_r is the index of refraction, ω is the angular frequency of the incident photon flux, $\hat{\mathbf{e}}$ is the unit vector of the photon polarization, and $\mathbf{p}$ is the vector form of the momentum operator. In the exponential term $\mathbf{s}$ represents the wavevector of V_p. Since the main interest is the interaction with light and the photon momentum is negligible compared to the electron momentum, the exponential term can be dropped out.

The term in the Dirac notation in Equation (2.42) is called electric dipole matrix element. Combining Equations (2.4) and (2.6) to represent the wavefunctions Ψ_n, the matrix element can be expanded, resulting in

$$\left\langle \Psi_{f\mathbf{K}_f} \middle| V_p \middle| \Psi_{i\mathbf{K}_i} \right\rangle = \frac{1}{A} \left\langle \psi_{f\mathbf{K}_f}(z) u_{f0}(\mathbf{r}) e^{i\mathbf{K}_f \cdot \boldsymbol{\rho}} \middle| V_p \middle| \psi_{i\mathbf{K}_i}(z) u_{i0}(\mathbf{r}) e^{i\mathbf{K}_i \cdot \boldsymbol{\rho}} \right\rangle. \qquad (2.44)$$

Considering the fact that the envelope functions (related to the band-offset/electrostatic potential) vary slowly compared to the Bloch functions (related to the lattice potential) and the initial and final states have the same momentum $\left(\mathbf{K}_f = \mathbf{K}_i \right)$, Equation (2.44) can be rewritten as [25]

$$\begin{aligned}
\left\langle \Psi_f \middle| V_p \middle| \Psi_i \right\rangle &\approx \left\langle u_{f0}(\mathbf{r}) \middle| V_p \middle| u_{i0}(\mathbf{r}) \right\rangle \left\langle \psi_f(z) \middle| \psi_i(z) \right\rangle \\
&+ \left\langle \psi_f(z) \middle| V_p \middle| \psi_i(z) \right\rangle \left\langle u_{f0}(\mathbf{r}) \middle| u_{i0}(\mathbf{r}) \right\rangle.
\end{aligned} \qquad (2.45)$$

This expression can be further simplified considering the specific aspects of each kind of transition.

a.   *Interband Transitions*

In this case, the transitions occur between the valence and conduction bands. Given that $\mathbf{K}_i$ and $\mathbf{K}_f$ are the same and are far from the edge of the Brillouin zone (otherwise the envelope function approximation is not valid), the Bloch functions are orthogonal. This cancels out the second term in the right hand side of Equation (2.45). The expansion of the interaction potential, in the remainder, results in

$$\left\langle \Psi_f \middle| V_p \middle| \Psi_i \right\rangle = \frac{q}{m_e{}^*} \left(\frac{I\hbar}{2\varepsilon_0 n_r \omega c} \right)^{1/2} \left\langle u_{f0}(\mathbf{r}) \middle| \hat{\mathbf{e}} \cdot \mathbf{p} \middle| u_{i0}(\mathbf{r}) \right\rangle \left\langle \psi_f(z) \middle| \psi_i(z) \right\rangle. \qquad (2.46)$$

The insertion of Equation (2.46) into Equation (2.42) results in the rate of transitions per state, given by

$$\begin{aligned}
W &= \frac{\pi q^2}{(m_e{}^*)^2} \frac{I}{\varepsilon_0 n_r \omega c} \left| \left\langle u_{f0}(\mathbf{r}) \middle| \hat{\mathbf{e}} \cdot \mathbf{p} \middle| u_{i0}(\mathbf{r}) \right\rangle \right|^2 \\
&\times \left| \left\langle \psi_f(z) \middle| \psi_i(z) \right\rangle \right|^2 \delta\left(\frac{\hbar^2 K^2}{2m_r{}^*} + E_f - E_i - \hbar\omega \right),
\end{aligned} \qquad (2.47)$$

where E_i and E_f are the initial and the final confined energy levels.

The extra term in the argument of the delta function accounts for the energy displacement due to the value of K (conduction and valence bands are assumed parabolas with opposite concavity). The reduced mass m_r* is defined as

$$\frac{1}{m_r *} = \frac{1}{m_e *} + \frac{1}{m_h *},$$ (2.48)

where m_e* and m_h* are the effective masses of the electron and hole, respectively.

At this point it is necessary to sum over all states (**K**). Considering the **K**-space a continuous space, and taking into account all occupied states in the valence band and the correspondent available states in the conduction band through the occupation statistics, it is possible to express the transition rate as

$$W = \frac{\pi q^2}{(m_e *)^2} \frac{I}{\varepsilon_0 n_r \omega c} \left| \langle u_{f0}(\mathbf{r}) | \hat{\mathbf{e}} \cdot \mathbf{p} | u_{i0}(\mathbf{r}) \rangle \right|^2 \left| \langle \psi_f(z) | \psi_i(z) \rangle \right|^2$$

$$\times \int \frac{A}{(2\pi)^2} d^2\mathbf{K} \left(f_i^{FDv}(E_i) \left[1 - f_f^{FDc}(E_f) \right] \delta \left(\frac{\hbar^2 K^2}{2m_r *} + E_f - E_i - \hbar\omega \right) \right).$$ (2.49)

Here, the term out of parenthesis inside the integral is the 2-D joint density of states involved in the transitions, and $f_i^{FDv}(E_i)$ and $[1 - f_f^{FDc}(E_f)]$ represent the Fermi-Dirac probability of occupancy of the valence band and probability of unocupancy of the conduction band, respectively. The integral in Equation (2.49) is evaluated substituting

$$E = \frac{\hbar^2 K^2}{2m_r},$$ (2.50)

considering the Fermi-Dirac statistics constant for the K values involved and using the properties of the delta function. The result is

$$W = \frac{q^2}{(m_e *)^2} \frac{IA}{\varepsilon_0 n_r \omega c} \left| \langle u_{f0}(\mathbf{r}) | \hat{\mathbf{e}} \cdot \mathbf{p} | u_{i0}(\mathbf{r}) \rangle \right|^2 \left| \langle \psi_f(z) | \psi_i(z) \rangle \right|^2$$

$$\times \frac{m_r *}{\hbar^2} \Theta \left(\hbar\omega - (E_f - E_i) \right) f_i^{FDv}(E_i) \left[1 - f_f^{FDc}(E_f) \right].$$ (2.51)

The modulus square of the Bloch functions matrix element term in Equation (2.51) must be expanded to obtain the strength of the transition. For practical reasons [5], only normal incidence (TE mode) is considered. Thus

$$\left|\hat{\mathbf{e}} \cdot S\mathbf{p}_{vc}\right|^2 = \left|\left\langle u_{f0}(x)\middle|p_x\middle|u_{i0}(x)\right\rangle\cos(\theta) + \left\langle u_{f0}(y)\middle|p_y\middle|u_{i0}(y)\right\rangle\sin(\theta)\right|^2 \qquad (2.52)$$

where $\mathbf{p}_{vc}$ is the Kane matrix element in the bulk material, S stands for selection rule due to the type of transition, and θ is the angle between the $\hat{\mathbf{e}}$ and the x axis. Here, for polarized light one can select, for example $\hat{\mathbf{e}} = e_x$ and drop the y term out. In the general case, it is necessary to take the average incident direction of $\hat{\mathbf{e}}$. The electron momentum x and y components can be considered the same on average, due to the heterostructure characteristics. Hence, Equation (2.52) can be rewritten as

$$\left|\hat{\mathbf{e}} \cdot S\mathbf{p}_{vc}\right|^2 = \left|\left\langle u_{f0}(x)\middle|p_x\middle|u_{i0}(x)\right\rangle\right|^2 \left|\cos(\theta) + \sin(\theta)\right|^2. \qquad (2.53)$$

Moreover, the average in θ for the second term in the right hand side of Equation (2.53) is one. The matrix element left can be evaluated in terms of Kane energy, E_p (eV), and for transitions close to the subband edges, where $K \approx 0$, it can be approximated as

$$\left|\left\langle u_{f0}(x)\middle|p_x\middle|u_{i0}(x)\right\rangle\right|^2 = \frac{m_0}{2}E_p, \qquad (2.54)$$

where E_p is unanimously accepted in the literature as varying between 17 and 25 eV for most of the III-V binaries. An extensive collection of this parameter is given in [20].

Finally the absorption coefficient is defined as the rate of transitions per unit volume divided by the incident photon flux, and can be expressed from the above derivations, for TE incident light with energy $\omega\hbar$, as

$$\alpha_{v_b c_b}^{TE}(\hbar\omega) = \frac{q^2}{(m_e{}^*)^2}\frac{m_r{}^*}{\varepsilon_0 n_r c\hbar(\hbar\omega)}\frac{1}{L}\left(\left(S^{TE}\right)^2\frac{m_0}{2}E_p\right)\left|\left\langle\psi_f(z)\middle|\psi_i(z)\right\rangle\right|^2$$
$$\times\Theta\left(\hbar\omega - (E_f - E_i)\right)f_i^{FDv}(E_i)\left[1 - f_f^{FDc}(E_f)\right]. \qquad (2.55)$$

The selections rules S are derived from the wavefunctions that satisfy Equation (2.16) and can be thought as a correction factor in the valence band simplification made here. For TE configuration [24],

$$S_{lh}^{TE} = 1/\sqrt{6}$$
$$S_{hh}^{TE} = 1/\sqrt{2}, \qquad (2.56)$$

where the indexes *lh* and *hh* stand for light and heavy holes, respectively.

Especially important is to notice that the overlap of the envelope function, $\langle \psi_f(z) | \psi_i(z) \rangle$, in Equation (2.55) imposes selection rules as well. Due to the orthogonality of the envelope functions in symmetric wells, transitions between subbands with different quantum numbers are forbidden. In most of the practical cases, transitions between the first valence subband and the second conduction subband are desired. In this case the symmetry of the quantum well must be broken and it is commonly done using step wells.

Further simplification is possible when undoped wells are used along with low temperatures. In this case, the probability of occupied states can be considered to be one in the valence band and zero in the conduction band. In this sense, Equation (2.55) reduces to

$$\alpha_{v_b c_b}^{TE}(\hbar\omega) = \frac{q^2}{(m_e*)^2} \frac{m_r*}{\varepsilon_0 n_r c\hbar(\hbar\omega)} \frac{1}{L}\left((S^{TE})^2 \frac{m_0}{2} E_p \right)$$
$$\times |\langle \psi_f(z) | \psi_i(z) \rangle|^2 \, \Theta(\hbar\omega - (E_f - E_i)). \tag{2.57}$$

Afterward, the absorption coefficient can be evaluated, applying Equation (2.57) for the case of heavy and light holes.

Interband absorptions are experimentally explored in bulk material and widely used in practical devices. In the case of quantum wells, interband absorptions are interesting mainly in optical modulators [26] or multiband detection [11]. Much more explored in QWIPs are the intersubband transitions that allow long wavelength detections with quite large bandgap materials.

b.   *Intersubband Transitions*
Electronic transitions between subbands within the same band occur in doped quantum wells. Valence band transitions require p-type doped material while conduction band transitions require n-type doped semiconductors. Due to the simplicity of the conduction band compared to the valence band, the conduction-band configuration is more practically explored. That is the case of interest in this work.

Starting with Equation (2.45), the first term in the right hand side vanishes, due to the orthogonality of the envelope functions. In addition, the Bloch overlap, in the same term, goes to one since the Bloch functions are normalized to unity. The expansion of the interaction potential, with the remainder, results

$$\left\langle \Psi_f \left| V_p \right| \Psi_i \right\rangle = \frac{q}{m_e *} \left(\frac{I\hbar}{2\varepsilon_0 n_r \omega c} \right)^{1/2} \left\langle \psi_f(z) \left| \hat{\mathbf{e}} \cdot \mathbf{p} \right| \psi_i(z) \right\rangle. \tag{2.58}$$

Given that the envelope function only depends on z, only the z component of the dot product $\hat{\mathbf{e}} \cdot \mathbf{p}$ applies to $\psi_i(z)$ resulting

$$\left\langle \Psi_f \left| V_p \right| \Psi_i \right\rangle = \frac{q\hbar}{m_e *(z)} \left(\frac{I\hbar}{2\varepsilon_0 n_r \omega c} \right)^{1/2} \left\langle \psi_f(z) \left| \frac{\partial}{\partial z} \right| \psi_i(z) \right\rangle \cos(\phi) \tag{2.59}$$

where ϕ is the angle between the vector $\hat{\mathbf{e}}$ and the z axis.

The insertion of Equation (2.58) into Equation (2.42) results in the rate of transition per state, given by

$$W = \frac{\pi q^2 \hbar^2}{(m_e *)^2} \frac{I}{\varepsilon_0 n_r \omega c} \left| \left\langle \psi_f(z) \left| \frac{\partial}{\partial z} \right| \psi_i(z) \right\rangle \right|^2 \cos^2(\phi) \delta(E_f - E_i - \hbar\omega). \tag{2.60}$$

Notice that the delta function in this case does not depend on K (the subbands are considered identical parabolas displaced by $E_f - E_i$).

At this point it is necessary to consider all occupied states in the initial subband and the correspondent available states in the final subband, introducing the occupation statistics and integrating over all states. The result is given by the total number of carriers, the appropriate occupation statistics, and the oscillator strength. Mathematically,

$$W = \frac{\pi q^2}{(m_e *)^2} \frac{I\hbar^2}{\varepsilon_0 n_r \omega c} \left| \left\langle \psi_f(z) \left| \frac{\partial}{\partial z} \right| \psi_i(z) \right\rangle \right|^2 \cos^2(\phi) \delta(E_f - E_i - \hbar\omega)$$
$$\times ALd f_i^{FD}(E_i) \left[1 - f_f^{FD}(E_f) \right]. \tag{2.61}$$

Recall that d represents the doping density. For low temperature operation, the total number of carriers can be considered d times the volume AL. The oscillator strength is commonly used as a measure of the strength of the transition and is defined as [27]

$$f_{i,f} = \frac{2}{m_e * \hbar\omega} \left| \left\langle \psi_f(z) \left| \frac{\partial}{\partial z} \right| \psi_i(z) \right\rangle \right|^2 \cos^2(\phi),$$
(2.62)

and obeys the rule [27]

$$\sum_f f_{i,f} = 1.$$
(2.63)

This condition is valid for all initial states i and the sum of the extending over all final states f.

Finally, the absorption coefficient, for transitions between two bound states within the conduction band, can be evaluated through

$$\alpha_{c_b c_b}(\hbar\omega) = \frac{\pi q^2}{m_e *} \frac{\hbar^2}{2\varepsilon_0 n_r c} f_{i,f} d f_i^{FD}(E_i) \left[1 - f_f^{FD}(E_f) \right] \delta(E_f - E_i - \hbar\omega).$$
(2.64)

Ideally the bound-to-bound intersubband absorption occurs in a single wavelength; however, in practice, the absorption spectrum is modified by various factors [26] such as nonuniformity in well width and collisions experienced by electrons, among others. The effect of this broadening is represented by replacing the delta function by a Lorentzian function given by

$$g(\hbar\omega) = \frac{1}{2\pi} \frac{\Gamma}{(E_f - E_i - \hbar\omega)^2 + \left(\Gamma/2\right)^2},$$
(2.65)

where Γ is the broadening parameter, which is equal the full width at half maximum of the absorption. The broadening parameter is normally determined experimentally and is about 10 to 20 meV.

Further simplification is possible, when the system is to operate in low temperatures or the difference between the initial and final states is much greater than $k_B T$. In this case, the occupancies probabilities can be considered one for the initial state and zero for the final state, resulting in

$$\alpha_{c_b c_b}(\hbar\omega) = \frac{q^2 d}{(m_e*)^2} \frac{\hbar^3}{\varepsilon_0 n_r c(\hbar\omega)} \left| \left\langle \psi_f(z) \left| \frac{\partial}{\partial z} \right| \psi_i(z) \right\rangle \right|^2$$
$$\times \cos^2(\phi) \frac{\Gamma}{(E_f - E_i - \hbar\omega)^2 + (\Gamma/2)^2}.$$
(2.66)

Analyzing the oscillator strength it is possible to observe the existence of some selection rules. The matrix element shows that for symmetric wells, transitions between states with the same parity are not allowed. This can be overcome by breaking the symmetry similarly to the interband case. Also, for normal incidence (TE mode), $\cos(\phi)$ is zero, and consequently, there is no absorption. Some optical techniques can be applied to overcome this selection rule, such as coupling throughout beveled edges [28] using different angles of incidence, application of several configuration of diffraction gratings [29] [30] to allow normal incidence, introduction of strain in the heterostructure [31], etc.

A strong characteristic of this kind of absorption is its narrow spectrum (about $1\ \mu m$). When a broader absorption spectrum is desired, it is worth to consider transitions between bound states to the continuum [32].

c. *Bound-to-Continuum Transitions*

Bound-to-continuum transitions are relatively weak, when bound-to-bound transitions with high oscillator strength happen in the structure. This can be explained by Equation (2.63). It becomes considerable, however, when only one confined state exists in the conduction band.

To be able to model those transitions, the continuum states must be computed. A simple but powerful technique to do that is to introduce a fictitious square well of width L_F, and infinite barrier height within which the continuum electrons are trapped. This configuration is shown schematically in Figure 4 [5].
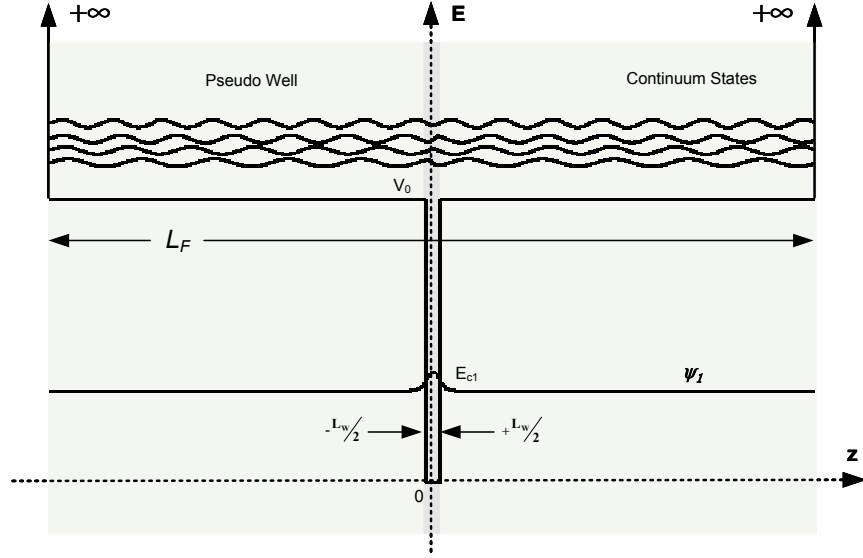
Figure 4   Schematic diagram of the pseudo-quantification technique of the continuous states in of a single square well.

The eigenenergies of such structure is given by [5]

$$E_n = n^2 \frac{\hbar^2 k_{L_F}^2}{2m_{e,b}*} ,$$ (2.67)

where $m_{e,b}*$ is the effective mass of the electron in the barrier, and k_{L_F} is the wavevector represented by

$$k_{L_F} = \frac{\pi}{L_F} .$$ (2.68)

The final states wavefunctions are then, numerically calculated using the pseudo-quantization model for each E_n.

For example, if L_F is of the order of $1\,\mu m$, for example, the energy level separation close to the barrier height is of the order of a hundredth of meV, which can be considered much smaller than the typical interactions or thermal energies (order of meV). The energies are so close that, rather than attempting to take into account individually, they are grouped together by means of infinitesimal batches of the one-dimensional density of states, given by [5]

$$\rho^{1D}(E) = \frac{L_F}{2\pi\hbar}\sqrt{\frac{2m_{e,b}*}{E}} \; . \tag{2.69}$$

Note that as L_F tends to infinity, the density of states increases without bound. More states become available over the same range of energy because the separation between levels decreases. Also, to be consistent with the adopted energy reference, the barrier height is subtracted from the final state energy, leading to

$$\rho^{1D}(E) = \frac{L_F}{2\pi\hbar}\sqrt{\frac{2m_{e,b}*}{E_f - V_0}} \; . \tag{2.70}$$

The density of the continuum states must be included in the transition rate formulation. This procedure allows writing the expressions for the absorption coefficients, for both discussed cases, as:

$$\alpha_{v_b c_c}^{TE}(\hbar\omega) = \frac{q^2}{(m_e*)^2}\frac{m_r*}{\varepsilon_0 n_r c\hbar^2(\hbar\omega)}\frac{L_F}{L\pi}\sqrt{\frac{m_{e,b}*}{2(E_f - V_0)}}$$
$$\times\left(\left(S^{TE}\right)^2\frac{m_0}{2}E_p\right)\left|\left\langle\psi_f(z)\middle|\psi_i(z)\right\rangle\right|^2 \tag{2.71}$$

and

$$\alpha_{c_b c_c}(\hbar\omega) = \frac{q^2 d}{(m_e*)^2}\frac{\hbar^2}{\varepsilon_0 n_r c(\hbar\omega)}\frac{L_F}{\pi}\sqrt{\frac{m_{e,b}*}{2(E_f - V_0)}}$$
$$\times\left|\left\langle\psi_f(z)\middle|\frac{\partial}{\partial z}\middle|\psi_i(z)\right\rangle\right|^2\cos^2(\phi). \tag{2.72}$$

Notice that in this situation the incident light energy can have values that obey

$$\hbar\omega = E_f - E_i, \; \text{for} \; E_f > V_0 . \tag{2.73}$$

Also, the dependence of the absorption coefficients on L_F is removed, since the continuum states wavefunctions are normalized by a factor proportional to the square root of the quantity L_F. This fact is very important because it assures that the computation of the bound-to-continuum absorption coefficients does not depend on the model.

7. Addition of an Electric Field

Actual quantum well photodetectors operate in the photoconductive mode, demanding the application of bias through the structure to be able to extract the photocurrent. Under this condition, a new potential factor is added to the Hamiltonian described in Equation (2.1), that becomes [26]

$$H = \frac{p^2}{2m_0} + V_c(\mathbf{r}) + V_e(\mathbf{r}) - qFz,$$
(2.74)

where the last tem represents the potential change caused by the applied electric field F. Notice that if F is constant, the overall potential bends linearly, as depicted in the Figure 5.
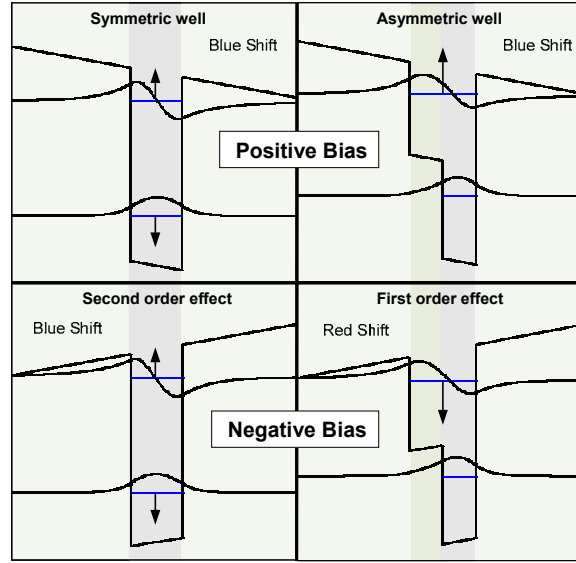
Figure 5   Potential profile diagrams of symmetric and asymmetric quantum wells under the effect of a constant electric field F (bias).

The solutions to the Schrodinger's equation, considering the new Hamiltonian gives the envelope wavefunction [18]

$$\psi(z') = C_1 \, \text{Ai}(z') + C_2 \, \text{Bi}(z'),$$
(2.75)

where Ai and Bi are Airy functions, C_1 and C_2 are constants that can be evaluated using the boundary conditions, and z' is given by [18]

$$z' = \left(\frac{2m^*}{\hbar^2}\right)^{1/3}\left[\frac{V_e(z) - E}{(qF)^{2/3}} - (qF)^{1/3}z\right]. \tag{2.76}$$

It is important to mention that the Airy functions present some difficulties in being evaluated numerically for either very large or very small arguments.

The effect of the static electric field in the confined energy levels within a quantum well is known as quantum confined Stark effect and can be evaluated using the time independent perturbation theory [17].

To determine the change in the difference between the fist and the second confined energy levels, under the influence of low electric field (case of interest in this work), a dipole perturbation Hamiltonian of the form,

$$V_b(z) = -qFz, \tag{2.77}$$

is employed.

When the quantum well is symmetric, the perturbation is null to the first order. The second-order effect is given by [5]

$$\Delta E = 2q^2F^2 \frac{\left|\langle\psi_1|z|\psi_2\rangle\right|}{E_1 - E_2}, \tag{2.78}$$

where ΔE is always positive indicating a blue shift in the photon absorption. This effect is very small and is normally obscured by the linewidth of the absorption spectrum.

In asymmetric quantum wells the first-order perturbation is non-zero and expressed by

$$\Delta E = qF\left[\langle\psi_1|z|\psi_1\rangle - \langle\psi_2|z|\psi_2\rangle\right], \tag{2.79}$$

where the term between rectangular brackets represents the displacement of the average position of the electron from the first to the second confined state. In this case, ΔE can be either positive or negative, depending on the bias signal and the well geometry. For the well depicted in Figure 5, a blue shift occurs when positive bias is applied and a red shift occurs for negative bias. In asymmetric structures the Stark effect becomes significant and it is commonly used in tunable detectors [33].

29

Perturbation theory breaks down when the electron wavefunction extends away from the well due to field assisted tunneling and thus the prediction of absorption peak position becomes more and more inaccurate. [5]

The understanding of the quantum effects present in heterostructures formed by periodic repetition of ultra-thin layers of semiconductors with different bandgaps is necessary step in order to design QWIP to meet specific requirements. Also it is important to understand how these heterostructures can act as photodetectors. This section gathered a set of theoretical tools that facilitates the comprehension of the discussed semiconductor configuration in a general sense. The following discussion, on the other hand, explains how QWIPs work and compiles the mathematical models to evaluate and analyze their performance.

B.   QUANTUM WELL INFRARED PHOTODETECTORS (QWIP)

Quantum well photodetectors are basically periodic repetitions of the *barrier/well/barrier* structure between heavy doped contact layers grown epitaxialy on a semiinsulating substrate. Ideally it is possible to pile as many stacks as the desired detection bands. In practice up to four bands have been demonstrated [34]. In this work, a detector consisting of three stacks with different, uncoupled, periodic repeated well/barrier structure, separated by heavy doped contact layers is considered.

When a quantum well photodetector is exposed to an incident photon flux, transitions between quantized energy levels can occur, as mentioned previously. The photon flux can be sensed when bias is applied to the structure and the transitions allow the extraction of the electrons from the well, to the barrier regions leading to a photocurrent. When the final state is confined, the electrons must tunnel through the potential barriers, made thinner by the applied electric field. Once the electron has escaped the confines of well, it accelerates toward the positive contact until it is captured. Figure 6 shows a schematic diagram of a biased multi quantum well structure and the photocurrent generation process.
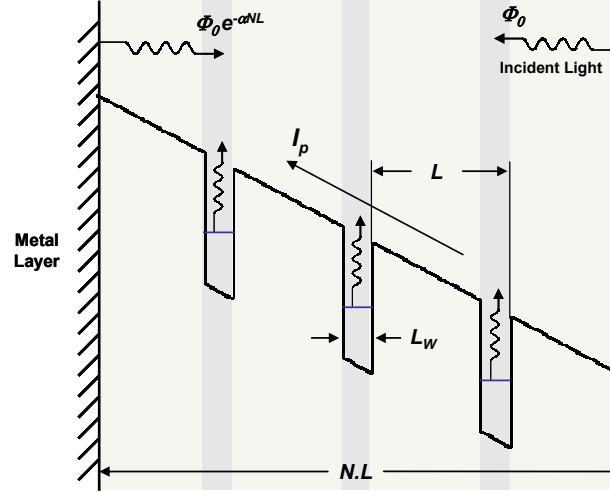
Figure 6   Schematic diagram of the photocurrent generation process in a biased multi quantum well structure.

If the exited state is near the potential barrier, which is true in most practical cases, the probability of an electron to tunnel through the barrier, narrowed by the effect of the bias voltage, can be considered nearly unity and independent of the well position [35]. Thus, a single model is used to estimate the photocurrent for both cases, bound-to-bound and bound-to-continuum transitions.

It is assumed that the absorption occurs only in the wells and the light gets in the structure (N wells), crosses the nth well, reaches the top metal layer and reflects back, crossing the same well twice. Then, if the structure is under an applied electric field, F, the photocurrent can be written as [36]

$$I_p(F) = \sum_{n=1}^{N} \frac{q\Phi_0}{\hbar\omega} \left(e^{-\alpha n L_W} + e^{-\alpha(2N-n)L_W} \right) \alpha l e^{-\frac{nL}{\upsilon(F)\tau}} . \qquad (2.80)$$

Here α is the absorption coefficient, Φ_0 is the incident optical power, $\hbar\omega$ is the photon energy, L is the period of the multiple quantum wells, L_W is the width of the well, $\upsilon(F)$ is the drift velocity under an applied electric field F, and τ is the exited carrier lifetime. Since, typically [36], for quantum well detectors, $\alpha L_W \ll 1$, Equation (2.80) can be simplified to

$$I_p(F) \approx \frac{2q\Phi_0}{\hbar\omega} \alpha L_W \sum_{n=1}^{N} e^{-\frac{nL}{\upsilon(F)\tau}} . \tag{2.81}$$

Finally, in the case of electrons, the drift velocity is given by [19]

$$\upsilon(F) = \frac{\mu_n F}{\sqrt{1+\left(\frac{\mu_n F}{\upsilon_s}\right)^2}}, \tag{2.82}$$

where μ_n is the electron mobility and υ_s is the electron saturation velocity. Both parameters can be found in [19] for the main binaries and its ternaries.

At this point it is worth to mention that under high electric field, the kinetic energy of the first electron, in the current generation process, can be large enough to cause the transition of a second electron, after collision. This process, repeated many times down the chain of wells, causes avalanche multiplication, increasing the photocurrent. This phenomenon is detailed in [35] and [37].

The way to characterize and measure the performance of a photodetector is throughout its figures of merit. The most common used figures of merit for quantum well detectors are discussed in the following section.

C.   FIGURES OF MERIT

1.   Absorption Spectra

The absorption coefficient is the key parameter used in photodetector design. The crystal heterostructures are optimized for the absorption spectra requirements and the absorption coefficient is normally measured after the sample growth, before the device fabrication.

A detailed discussion is presented in Section II.A.6, where the absorption coefficients for the cases of interest in this work are derived. It is worth to notice though, that the absorption coefficient for quantum wells with bound-to-continuum transitions is significantly lower and wider than for those with bound-to-bound transitions. This fact can be attributed to the conservation of the integrated oscillator strength. Mathematically,

$$\alpha_p \frac{\Delta\lambda/\lambda}{d} \approx \text{constant}, \tag{2.83}$$

where α_p is the absorption coefficient peak, $\Delta\lambda/\lambda$ is the absorption bandwidth and d is the well doping density.

Experimental measurement of the absorptance using Fourier Transform Infrared spectrometry permits to obtain the absorption spectra. This procedure is deeply explored in Chapter IV.

2.   Quantum Efficiency and Photoconductive Gain

The photocurrent in photoconductors is defined as [37]:

$$I_p = q\eta \frac{\Phi_0}{\hbar\omega} G, \tag{2.84}$$

where η is the quantum efficiency and G is the photoconductive gain. Comparing Equations (2.84) and (2.81), it is easy to identify that

$$\eta \approx 2\alpha l \tag{2.85}$$

for $\alpha l \ll 1$, and

$$G = \sum_{n=1}^{N} e^{-\frac{nL}{\upsilon(F)\tau}}. \tag{2.86}$$

For moderate electric fields, which is the case in most practical cases, the mean free path, $\upsilon(F)\tau$, is considerably larger than the period of the multiple quantum wells (L) and the summation of Equation (2.86) can be evaluated as

$$G = \frac{\tau}{L/\upsilon(F)}, \tag{2.87}$$

that represents the rate between the exited carrier lifetime and the transit time.

3. Responsivity

The responsivity figure quantifies the amount of photocurrent generated per watt of incident radiant photon power. It can be expressed mathematically as

$$R(F) = \frac{I_p(F)}{\Phi_0}. \tag{2.88}$$

Combining the expressions (2.88), (2.84), (2.85), and (2.87) results in

$$R(F) = (2\alpha l)\frac{q}{\hbar\omega}\frac{\upsilon(F)\tau}{L}. \tag{2.89}$$

It is important to notice the responsivity dependence on the absorption coefficient and bias, through the drift velocity. The absorption coefficient is responsible for the shape (spectrum) and the electric field for the amplitude. Increasing the availability of carriers (doping concentration), the photocurrent will increase and consequently the responsivity.

4. Dark Current

A biased photodetector, when no light is incident, exhibits dark current. Three dark current generation mechanisms in quantum well devices can be easily identified [38]. First, sequential resonant tunneling can happen, causing electrons to "jump" from well to well, through the barriers. This process is independent of temperature and is the dominant source of dark current at very lower temperatures. It can be reduced if larger barriers are used. The second mechanism is thermally assisted tunneling which involves thermal excitation and tunneling through the tip of the barrier into the transport states. This process is the dominant source at medium temperatures and can be reduced by placing the final state as far as possible to the initial state, reducing the probability of thermoionc transitions. The third mechanism is classical thermoionic emission and it is the dominant source at higher temperatures. To reduce this effect, deeper wells must be considered in combination with reduced available carriers (less doping). Obviously this will reduce the photocurrent as well, and a compromise between both must be established.

34

In order to estimate the dark current, it is necessary to estimate the effective number of electrons which are thermally exited out of the well into the continuum transport states as a function o bias. This is given by [39]

$$n^*(F) = \frac{m_w^*}{\pi\hbar^2 L} \int_{E_i}^{\infty} f^{FD}(E) T(E,F) \, dE \tag{2.90}$$

where the term outside the integral is the 2-D density of states divided by the multi quantum well period L, and the Fermi distribution is given by Equation (2.33) where E is replaced by $(E - E_i)$ and E_i represents the bound ground state. The bias-dependent tunneling current transmission factor for a single barrier is represented by $T(E,F)$ and can be described by [40]

$$T(E,F) = \frac{2E}{LV_0} \left(\frac{2(V_0 - E)}{m_b^*} \right)^{1/2} e^{\left[-\frac{4}{3qF\hbar} \sqrt{2m_b^*} (V_0 - E)^{3/2} \right]}. \tag{2.91}$$

Recall that V_0 represents the barrier height.

Equation (2.90) accounts for both thermoionic emission above the barrier height and thermoionically assisted tunneling below the barrier height. It can be solved numerically in order to estimate the dark current, expressed by

$$I_D(F) = q n^*(F) \upsilon(F) A \tag{2.92}$$

where A is the cross sectional area of the device and all other parameters are known.

The main mechanism to reduce the dark current, not mentioned before, is to reduce the temperature of operation. To verify the relationship between dark current and temperature it is possible to assume $T(E) = 0$ for $E < V_0$ and $T(E) = 1$ for $E > V_0$ in Equation (2.90), which is a good approximation for low biased systems. The dark current, then, can be written as

$$I_D(T) = q \upsilon A \frac{m_w^*}{\pi\hbar^2 L} k_B T e^{-\frac{(E_c - E_F)}{k_B T}}, \tag{2.93}$$

where E_c is the cutoff energy $(V_0 - E_i)$ and E_F is quasi-Fermi energy which can be evaluated using Equation (2.34). Therefore, the dark current divided by the temperature is related to the temperature exponentially, as

$$\frac{I_D}{T} \propto e^{-\frac{E_c - E_F}{k_B T}},$$

(2.94)

indicating that it decreases as the inverse of the temperature increases.

5.   Detectivity

The detectivity, D^*, of a detector is a measure of the smallest photon flux that can be measured, and clearly depends on the noise associated with the detector. It is mathematically defined as

$$D_\lambda^* = \frac{\sqrt{A\Delta f}}{NEP}$$

(2.95)

where Δf is the bandwidth of the integration filter, and *NEP* stands for noise equivalent power, that is the noise power that gives a unity signal-to-noise ratio (*SNR*). The last can be estimated using Equation (2.88) as

$$NEP = \frac{i_{ND}(F)}{R_p(F)},$$

(2.96)

where the dark current noise, $i_{ND}(F)$, is given by

$$i_{ND}(F) = \left(4qI_D(F)G\Delta f\right)^{1/2}.$$

(2.97)

Finally, making $\Delta f = 1$ Hz and combining Equations (2.95), and (2.96), the peak detectivity in $[\text{m}\sqrt{\text{Hz}}/\text{W}]$ can be written as

$$D_\lambda^*(F) = \frac{R_p(F)}{i_{ND}} \sqrt{A}.$$

(2.98)

A more relevant figure of merit than the peak detectivity is the blackbody detectivity with is obtained by calculating the spectral overlap of the responsivity with a

blackbody emission spectrum at temperature T_{BB}. Thus, the blackbody detectivity becomes

$$D_{BB}^* = \frac{R_{BB}}{i_{ND}} \sqrt{A} \,,$$ (2.99)

where the bias dependence was omitted for convenience, and R_{BB} is given by

$$R_{BB} = \frac{\int_{\lambda_1}^{\lambda_2} R(\lambda) W_{BB}(\lambda)\, d\lambda}{\int_{\lambda_1}^{\lambda_3} W_{BB}(\lambda)\, d\lambda} \,.$$ (2.100)

Here the power radiated per unit wavelength interval at wavelength λ, per unit area of a blackbody at temperature T_{BB} (blackbody spectral density) is given by

$$W_{BB}(\lambda) = \frac{2\pi c h^2}{\lambda^5} \frac{1}{e^{\left(\frac{hc}{\lambda k_B T_{BB}}\right)} - 1} \,.$$ (2.101)

It is worth noting that, for most applications, the blackbody responsivity R_{BB} is reduced only a relatively small amount from the peak value R_p. Also, QWIP detectivity increases almost exponentially with decreasing temperature [41]. This fact can be explained by the strong dependence of the dark current on thermoionic emission and thermoionic assisted tunneling. Also it must be considered that the improvement on detectivity implies reduction in dark current noise.

Another important aspect is the dependence on the detectivity on doping. Applying the same simplification used to determine the dark current dependence on temperature, it has been proved [28] that

$$D^* \propto \frac{\rho}{\sqrt{e^{\rho} - 1}}$$ (2.102)

where ρ is linearly proportional to the doping density in the well. This indicates that the detectivity will increase with the increasing doping density until reaches a maximum and starts to decrease again. It is worth mentioning that the maximum region is very wide, allowing the doping density to be used to optimize the responsivity instead.

Although the mathematical models discussed above rely on a great number of simplifications, it has been shown (in the references cited in this section) that they are appropriate for the practical situations of interest.

The figures of merit discussed in this section should be considered in both the design and the characterization phases. In the design they act as requirements and great care is necessary since the maximization of one figure may imply the minimization of other. In the characterization phase they are a measure of the performance and the requirement compliance.

This chapter assembled the minimum theoretical background necessary to build the mathematical models that allows us to design and analyze the performance of QWIP. Specificities of the photodetectors in discussion were considered and used as simplification factors in the models. Supported by this theory the next chapter presents the practical considerations towards the actual devices, the computational tools developed to support the design and the final proof-of-concept QWIP design that meets the requirements stated in the introductory chapter.

III. QWIP DESIGN

The previous chapter covered the theoretical aspects of quantum well photodetectors. Nevertheless, to be able to design actual devices it is necessary to perform a quantitative analysis of the physical behavior, already described. This is done sequentially in this chapter, introducing numerical solutions of the mathematical models, adapted for the design specificities of the detectors requirements.

The first requirement for a photodetector is the operation spectrum. As specified before, the interest here is to have a QWIP capable to detect simultaneously wavelengths within three distinct bands: 0.9 to 1.4 μm (near infrared); 3.8 to 5.0 μm (mid infrared); and 8.0 to 10.0 μm (long wavelength infrared).

A. INITIAL CONSIDERATIONS

There is no established sequence in QWIP design. Several analyses and considerations must be done and most are interactive, forcing the designer to go back and forth. This section discusses the preliminary assumptions and analysis towards the basic photodetector configuration.

Many ways have been used to achieve multiband detection using quantum wells [28]. However, currently, two ways predominate, coupled quantum wells [42] and multi-stack quantum wells [34]. The former has the advantage of using a fixed bias voltage to detect all bands simultaneously. Conversely it is hard to distinguish those without further spectral analysis. The requirement of discriminating between the bands demands separated readouts, possible to implement in the last configuration.

The multi-stack of uncoupled wells configuration, selected in this work, is shown schematically in the Figure 7. Three different stacks of quantum wells with different absorption characteristics are piled between contact layers. The readout bias can be optimized for each band independently. It is important to mention, though, that this configuration demands high accuracy of epitaxial growth due to the large number of different layers needed.

39
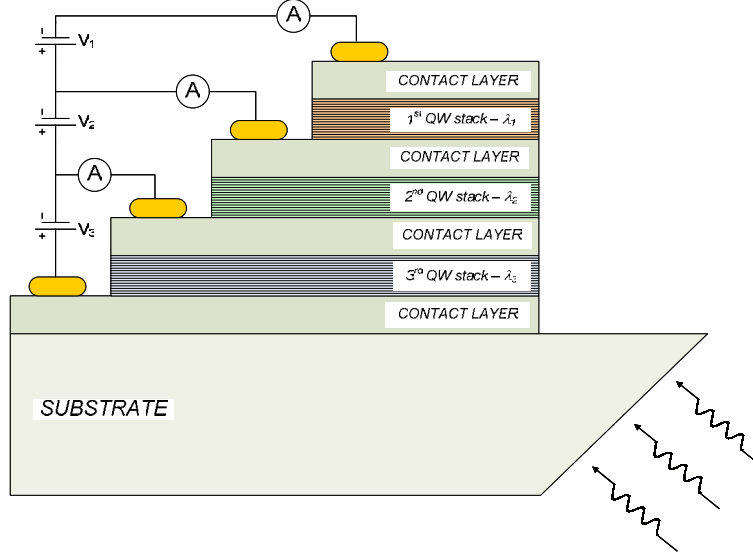
Figure 7   Schematic diagram of a multi-stack quantum well photodetector with independent readouts.

Considering this configuration, to minimize the dark current and maximize responsivity and detectivity, the second bound state in the conduction band (final state) is more likely to be placed just bellow the top of the well ($E_f \approx V_0$).

The first well stack is responsible for detecting the near infrared. The lowest wavelength detected due to intersubband transitions reported on the literature [28] is 2.7 μm . Thus, inerband transitions must be used for the NIR band. Furthermore, according to the selections rules for interband transitions, the well must be asymmetric to allow the transition the ground state of the valence band to the first exited state of the conduction band. Thus, a step well configuration seems to be more apporpriate. Moreover, only intrinsic carriers participate in the transitions from the valence to the conduction band, eliminating the necessity of doping these wells. The main constraints here are to control the depth of the well to achieve the right wavelength, as well as to adjust the asymmetry to maximize the transition strength.

The second well stack is responsible for mid-infrared detection. This can be accomplished by intersubband transitions in a deep quantum well. The main constraint here is to achieve a deep well without having too much strain in the system. Also the doping concentration of these wells must be adjusted to maximize the figures of merit.

The third stack is responsible for the long-infrared detection. This is the most commonly used configuration and can be achieved without much dificulty using shallow wells. The principal constraint here is to control the dark current. In shallow wells, the thermoionic emission is strong; hence the doping concentration must be reduced to control this process.

All the three stacks are schematically represented in the Figure 8, in terms of potential diagram. It is worth noting that all considerations from now on focus on the optimization of the performance of the three stacks together. Since this work aims a verification of the concept, a few compromises on the requirements are acceptable to make it feasible.

Figure 8   Schematic diagram of the potential profile of the basic detector configuration, including all three quantum well stacks.

In selecting the configuration, the materials must be chosen, based upon their properties, availability, growing process maturity, and cost, among other factors. Figure 9 shows a plot of energy bandgaps vs. lattice constants for major III-V compounds [43].

41

Ternary alloys are denoted by lines between binaries and quaternary alloys are represented by the colored areas.
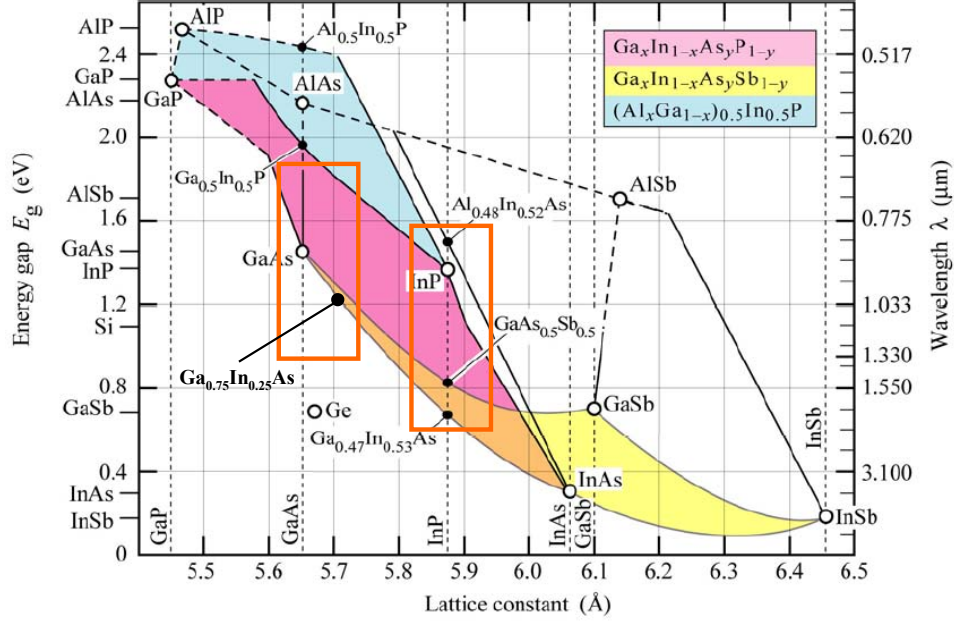
Figure 9   Plot of energy bnadgaps vs. lattice constants for major III-V compounds. The solid lines and the dashed lines represent the direct-gap and indirect-gap regions, respectively. Ternary alloys are denoted by lines between binaries and quaternary alloys are represented by colored areas. (After Ref. [43].)

The requirement of closely matching lattice constants separates these semiconductors into five distinct families in terms of compatible substrate materials [5]. The best controlled of these families is GaAs/$Al_xGa_{1-x}As$, and all the compositional aluminum fractions are accessible, as the lattice constant does not vary significantly from GaAs to AlAs. $Ga_xIn_{1-x}As$ can be grown on GaAs substrates if the composition of indium is not very high ($x < 0.4$), and the strain effects for this system are well known (see for example [44]). Another important system includes $In_xGa_{1-x}As_yP_{1-y}$ and $Al_xIn_{1-x}As$, which can be grown on InP substrates and is commonly used in lasers applications [45]. Also, $In_xAs_{1-x}Sb$ and $Al_xGa_{1-x}Sb$ are normally grown on GaSb substrates. Finally, the lattice constants available to $Hg_{1-x}Cd_xTe$ are suitable to deposit on a CdTe substrate and allow a large range of accessible bandgaps. Recently more combinations have been tested [28].

In addition to the lattice constant and bandgap energies, the band offsets are utterly important to determine the band edge potentials and consequently the depth of the wells. Some theoretical models are available to roughly estimate the band offsets; although, to design quantum well devices, much more accurate values than those obtained from the theoretical models are required. Methods such as absorption measurement, photoluminescence measurement, and x-ray core level photoemission spectroscopy are used for experimental determination of band-offsets [26]. Even experimental methods cannot assure accurate values of band offset, making this parameter a considerable constraint when working with certain families of materials [45]. A good collection of band-offset parameters can be found in [20].

The analysis on available data from the families of compounds mentioned above, including cost and fabrication potentialities led to two possibilities, $GaAs/Al_xGa_{1-x}As/In_xGa_{1-x}As$ on GaAs substrate and $(In_{0.53}Ga_{0.47}As)_y(InP)_{1-y}/Al_{0.48}In_{0.52}As$ on InP substrate. These families are highlighted in red in Figure 9 For simplicity, from now on, both are addressed by their substrate, as the GaAs system and the InP system.

Very reliable material data (properties) and mature and cheaper fabrication processes are advantages of the GaAs system. However, to assemble deep wells necessary for mid-infrared detection it is necessary to increase the Indium composition, raising the strain in the system due to the lattice mismatch. Limitations on indium composition are well documented in [44] [46] and [47], and lead to a design limit of 0.25 if used in thin wells. Furthermore, the critical layer thickness that represents the maximum thickness of the $Ga_xIn_{1-x}As$ under which the large lattice mismatch is totally accommodated by uniform elastic strain, is dependent on the indium quantity [45]. Therefore, the higher the indium composition, the lower the critical thickness, limiting the design possibilities. Also, since AlAs is an indirect semiconductor, the aluminum concentration must be kept lower than 0.4, to have a direct $Al_xGa_{1-x}As$ ternary. Moreover the high bandgap of GaAs and the limitation on the indium composition indicates that it might be difficult to comply with the near infrared requirement.

The InP system, on the other hand, presents very controversial band offset data [45], and uses more difficult and expensive fabrication processes. The absence of strain,

due to the matched lattice, is an advantage. Also the lower bandgaps of the compounds indicates the possibility to achieve the desired near-infrared detection spectrum. Adaptations on the requirements are also considered in order to make it feasible.

A significant limitation concerning the material composition is the growing process. When using MBE, for example, a limited amount of the basic compounds vapor sources are available. Therefore the number of different compositions of the same ternary or quaternary is limited. For example, using two sources of Al in different temperatures, it is possible to grow $Al_xGa_{1-x}As$ with 3 different fixed-values of x determined by: the first source (when only its shutter is open), the second source (when only its shutter is open), and both (when both shutters are open). This restricts the structure in having only 3 different compositions of $Al_xGa_{1-x}As$, limiting the designing degrees of freedom.

Lastly it is necessary to consider the angle of incidence selection rules to be able to design the optical coupling. According to the previous chapter, intersubband transitions are forbidden in symmetric quantum wells, thus diffraction gratings must be etched on the top of the last contact layer, just before the metallization. Also a high purity non-alloyed gold and silver must be considered, in order to maximize the reflection [48]. A complicating factor is that the grating must be optimized for two different bands. Several configurations have been proposed [49] [50], however the limitations on mask lithography and processing capabilities restrict the possibilities.

Another complicating factor is the fact that the wavelengths of the LWIR are almost two times the wavelengths of the MWIR. As will become clear in the Section IV.2, it is impossible to optimize, simultaneously, the grating pattern for wavelengths that are multiples to each other. Therefore, a good strategy is to place the detection peaks closer of each other. Then, considering that smaller dimensions are required for smaller wavelengths and that the small dimensions (less than $1\,\mu m$) are difficult to implement, the detection peaks for the MIWR and LWIR should be placed as close to each other as possible. This is also an advantage if just one grating pattern is possible to be applied to satisfy both spectral regions.

Having established the basic detector configuration, based on the requirements, constraints, and data availability, the first design step is to quantitatively determine the bound states in the conduction and valence bands and their respective wavefunctions.

B.   SELF CONSISTENT SCHRODINGER-POISSON SOLUTIONS

The self-consistent Schrodinger-Poisson solutions are necessary to account on the potential distortion caused by the charge distribution. This approach can be summarized as follows. First, the band edge potential $V_e(z)$ is computed from the structure material properties. Then the perturbation potential $V_b(z)$, due to applied electric field, is computed and added to the band edge potential ($V(z) = V_e(z) + V_b(z)$). Next step is to solve the Schrodinger's equation for the structure, to obtain the bound states E_i and their respective wavefunctions ψ_i, that will be used as the first guess to compute the charge distribution potential $V_\rho(z)$, through the solution of the Poisson's equation of the structure. The potential $V_\rho(z)$ is then added to the original ($V(z) = V_e(z) + V_b(z) + V_\rho$) and the Schrodinger's equation is solved to the new potential. The iterations repeat until the bound states energies converge. This procedure is schematically depicted in Figure 10. The details in the figure, including equations and the respective parameters are discussed in the following sections.
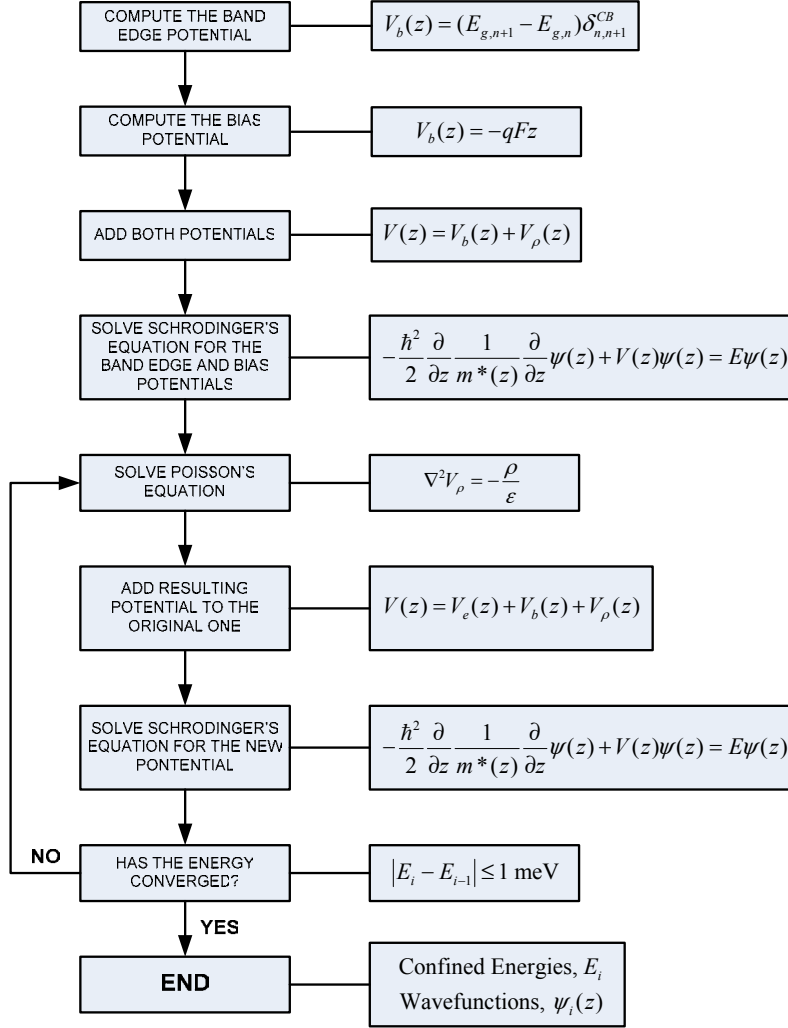
Figure 10   Schematic diagram of the self-consistent Schrodinger-Poisson solution main steps. All equations and parameters are explained on the text.

The first step to solve a quantum well Shrodinger's equation is to compute the band edge potential profile. This can be done, basically, taking the bandgap energies of the material layers along with their band offset ratios.

1.   Bandgap and Effective Mass Parameters

The bandgap parameters, for both the GaAs system and InP system, shown in the Figure 9 are tabulated in [20]. For the ternary $A_x B_{1-x} C$, the following expression is used:

$$E_g(A_x B_{1-x} C) = x E_g(AC) + (1-x) E_g(BC) - x(1-x) C_b(ABC) \qquad (3.1)$$

46

where the so called bowing parameter C_b accounts for the deviation from a linear interpolation between the endpoints two binaries AC and BC. For the lattice matched quaternaries $(A_xB_{1-x}C)_y(DE)_{1-y}$, the corresponding band parameter is expressed as

$$E_g\left((A_xB_{1-x}C)_y(DE)_{1-y}\right)= yE_g(A_xB_{1-x}C)+(1-y)E_g(DE)- y(1-y)C_b(ABCDE). \quad (3.2)$$

The temperature dependence of the bandgap must also be considered and is given by Equation (2.13). Thus, the substitution of the GaAs and InP systems material parameters into Equations (2.13), (3.1) and (3.2) gives the needed bandgap values.

The effective mass profile is directly deduced by the properties of each layer. For the binary compounds, the effective masses along the crystal direction [100] are given by the following expressions [20]:

$$\frac{m_0}{m_e*}=(1+2F_K)+\frac{E_p\left(E_g+(2\Delta_{so}/3)\right)}{E_g(E_g+\Delta_{so})}, \quad (3.3)$$

$$\frac{m_0}{m_{hh}*}=\gamma_1-2\gamma_2, \quad (3.4)$$

and

$$\frac{m_0}{m_{lh}*}=\gamma_1+2\gamma_2 \quad (3.5)$$

where F_K is the Kane parameter, E_p is the Kane energy, Δ_{so} is the spin-orbiting splitting parameter, and γ_i are the Luttinger parameters. All these parameters are obtained experimentally and are listed, for the binaries in question, in [20]. For the ternaries and lattice matched quaternaries of the type A_xB_{1-x}, the effective masses can be obtained by the linear interpolation of the extremes (A and B) through the expression

$$\frac{1}{m*(A_xB_{1-x})}=x\frac{1}{m*(A)}+(1-x)\frac{1}{m*(B)}. \quad (3.6)$$

The substitution of the GaAs and InP system material parameters into Equations (3.3) to (3.6) gives a series of equations necessary to obtain the needed effective masses.

2.   Potential Profile

An important remark is that, since the design seeks a detector with uncoupled wells, all development in this section considers a configuration of two external barriers and one quantum well. Also, step wells with one or more steps can be used to create asymmetric structures. In this sense, the bottom of the conduction band of the smallest bandgap layer is considered the potential zero, and the center of the same layer is taken as $z = 0$. Thus the conduction band edge potential profile is given by

$$V_e^{CB}(z) = \begin{cases} \sum_{n=1}^{N-1} \left[(E_{g,n+1} - E_{g,n}) \delta_{n,n+1}^{CB} \right] \Theta(z - z_n) & \text{for } z \geq 0 \\ \sum_{m=-1}^{-M+1} \left[(E_{g,m-1} - E_{g,m}) \delta_{m,m-1}^{CB} \right] \Theta(-z + z_m) & \text{for } z < 0, \end{cases} \tag{3.7}$$

where N is the number of layers in the positive direction, $\delta_{n,n+1}^{CB}$ represents the conduction band offset ratio between the *n*th and *(n+1)*th layers, found in [20] and [45], and z_n is the coordinate of the interface between them. The same interpretation is taken for the negative direction, replacing N by M and n by m. The bandedge potential defined this way can handle several distinct layers to model asymmetric step wells. In the same way, the valence band potential is given by

$$V_e^{VB}(z) = \begin{cases} \left[\sum_{n=1}^{N-1} \left[-(E_{g,n+1} - E_{g,n})(1 - \delta_{n,n+1}^{CB}) \right] \Theta(z - z_n) \right] - E_g^{REF} & \text{for } z \geq 0 \\ \left[\sum_{m=-1}^{-M+1} \left[-(E_{g,m-1} - E_{g,m})(1 - \delta_{m,m-1}^{CB}) \right] \Theta(-z + z_m) \right] - E_g^{REF} & \text{for } z < 0, \end{cases} \tag{3.8}$$

where E_g^{REF} is the lowest bandgap within the structure.

As mentioned before, the most critical parameter to determine the band edge potential is the band offset. This is determined experimentally and, normally, gives values widely spread, depending on the experimental method used, especially for the InP system. The values used were confirmed experimentally in the Sensor Research Laboratory (SRL), Naval Postgraduate School (NPS) [51], for the GaAs system, and an average value suggested by the authors in [20] and [45], for the InP system. When compounds

with slightly different compositions from the experimental data are used, it is suggested on the literature that linear interpolation would be a reasonable correction. The data used in this work is given in [20].

Recall from Equation (2.77) that the potential due to bias applied on the heterostructure is given by

$$V_b(z) = -qFz.\qquad(3.9)$$

The addition of this and the band edge potential is represented by

$$V(z) = V_b(z) + V_e(z),\qquad(3.10)$$

where $V(z)$ is the potential profile without taking into account the electrostatic potential.

At this point, all information is in place to solve the structure Schrodinger's equation and to obtain the confined energy levels as well as the corresponding wavefunctions.

3.   Numerical Solution of the Schrodinger's Equation

The selected method to solve numerically the Schrodinger's equation here was a combination of the *shooting* method and the *finite differences* [52] [18]. The one-dimension Shrodingers's equation in the heterostructure along the growth axis is given by

$$-\frac{\hbar^2}{2}\frac{\partial}{\partial z}\frac{1}{m*(z)}\frac{\partial}{\partial z}\psi(z) + V(z)\psi(z) = E\psi(z),\qquad(3.11)$$

that can be expanded as

$$-\frac{1}{[m*(z)]^2}\frac{\partial}{\partial z}m*(z)\frac{\partial}{\partial z}\psi(z) + \frac{1}{m*(z)}\frac{\partial^2}{\partial z^2}\psi(z) = \frac{2}{\hbar^2}[V(z) - E]\psi(z).\qquad(3.12)$$

First, the continuous z direction is discretized in an evenly spaced grid with step δz. Second, the derivatives are replaced by their second order central finite difference approximations, expressed as

$$\left.\frac{\partial f}{\partial z}\right|_z \approx \frac{f(z+\delta z) - f(z-\delta z)}{2\delta z},\qquad(3.13)$$

for the first derivative, where f represents an arbitrary function, and

49

$$\frac{\partial^2 f}{\partial z^2}\bigg|_z \approx \frac{f(z+\delta z)-2f(z)+f(z-\delta z)}{(\delta z)^2}, \tag{3.14}$$

for the second derivative. Applying Equations (3.13) and (3.14) to Equation (3.12), after some algebra, the result is [18]

$$\frac{\psi(z+\delta z)}{m*(z+\delta z/2)} = \left\{ \frac{2(\delta z)^2}{\hbar^2}[V(z)-E] + \frac{1}{m*(z+\delta z/2)} \right.$$
$$\left. + \frac{1}{m*(z-\delta z/2)} \right\}\psi(z) - \frac{\psi(z-\delta z)}{m*(z-\delta z/2)}. \tag{3.15}$$

Equation (3.15) is the *shooting equation*. The equation shows that knowing two values of the wavefunction, $\psi(z-\delta z)$ and $\psi(z)$, the third point, $\psi(z+\delta z)$, can be predicted. Using the new point together with its predecessor, a fourth point can be calculated and so on. Hence the wavefunction can be deduced for any particular energy value. The solutions for stationary states have wavefunctions which satisfy the standard boundary conditions, expressed as

$$\psi(z) \to 0 \quad \text{and} \quad \frac{\partial}{\partial z}\psi(z) \to 0, \quad \text{as} \quad z \to \pm\infty. \tag{3.16}$$

It has been proved [18] that the general initial conditions that can handle any potential profile is given by

$$\psi(z-\delta z) = 0 \quad \text{and} \quad \psi(z) = 1, \tag{3.17}$$

since multiplying an eigenstate (wavefunction ψ) for a constant does not affect the eigenvalue (bounded energy E).

Sequentially, the energy is varied systematically in δE steps, until the wavefunction switches from diverging to $-\infty$ to diverging to $+\infty$. That can be mathematically expressed as

$$\left(\psi(E)\big|_{z\to+\infty}\right)\left(\psi(E+\delta E)\big|_{z\to+\infty}\right) < 0. \tag{3.18}$$

Clearly an energy level exists between these values for which the wavefunction will tend smoothly to zero. Since the problem now is to find a root of $\psi(E)\big|_{z\to+\infty} = 0$, the energy

grid is refined in the interval $(E,\ E+\delta E)$ and the Newton's method is applied [52]. This is done to accelerate the convergence to the true solution. Recall that, according to the Newton's method, if E_i is the first guess to the solution of $\psi(E)\big|_{z\to+\infty}=0$, then a better estimate is given by

$$E_{i+1}=E_i-\frac{\psi(E_i)\big|_{z\to+\infty}}{\psi'(E_i)\big|_{z\to+\infty}},\qquad(3.19)$$

where the denominator of the quotient at the right side is the first derivative of the wavefunction ψ with relation to E, at E_i, at $z\to+\infty$.

The tolerance of 1 meV in energy values is certainly within the error caused by other uncertainties. In terms of wavelength, for a quantum well structure with absorption peak around $4.5\ \mu m$, the change of 1 meV in the difference between the conduction band bound states would cause a shift of the order of one hundredth of a micrometer on the peak absorption.

In practice, the above mentioned iterative procedure starts and ends at finite distances from $z=0$. This is the same as assuming that, at the lower and upper limits (effective infinites) of the z domain, the barrier potential is infinite, forcing the wavefunction to be zero there. The limits of the z domain should be chosen to be at sufficient extent so as not to affect the eigenvalue. It has been proven [18] that if the energy is the only motivation for this calculation, outer barriers as wide as 150 Å will suffice.

When the wavefunction is needed to compute other parameters, great care must be taken. Even though the eigenvalues can be obtained within the convergence tolerance, for thin outer barriers, the wavefunctions might not satisfy the second boundary conditions, $\psi'=0$ at $z\to\pm\infty$. On the other hand, for thick outer barriers, the wavefunction starts to diverge, due to limitation in numerical precision of the energy values. The definition of thin and thick depend on the structure being solved and should be monitored for each specific problem, in order to find the appropriate limits of the z domain. Since the wavefunction convergence is dependent on the accuracy of energy, the greater the figure accuracy that can be used, the thicker the barriers that can be included in the model. Per-

sonal computer codes normally assign 16-figure accuracy to a double precision number. If the quantum well configurations demand higher precision than that, more sophisticated computational tools must be used.

The last parameter that must be defined is the step length δz. Since the atomic dimension limits the layer thickness, there is no practical reason to use steps smaller than 1Å. Higher values can be used, to reduce the computation time, according to the configuration being solved. For the structures computed in this work, $\delta z = 1$Å was used.

The final wavefunction is then obtained applying the energy value calculated by the Newton's method in Equation (3.15), considering the appropriate limits, steps and tolerances, just discussed.

The wavefunctions obtained for this numerical method are not normalized. This can easily be achieved multiplying the wavefunction by its normalization factor,

$$N_\psi = \frac{1}{\sqrt{\int_{z_{min}}^{z_{max}} \psi^*(z)\psi(z)\,dz}} \, , \tag{3.20}$$

where, the symbol $(*)$ indicates the complex conjugate.

The shooting method, sketched in the Figure 11, is a powerful tool to handle any kind of potential profile. That is very important in solving biased multiple layer structures with a varying doping profile. Because of that, it is very suitable for self-consistent solutions. However, if not carefully implemented, it can be very costly computationally. Also the limitation on the wavefunction convergence for wide outer barriers must be taken care externally. It is normally possible, imposing a zero value to the wavefunction before the divergence region.

TAKE THE SCHRODINGER'S EQUATION DESCRIBING THE STRUCTURE

$$-\frac{\hbar^2}{2}\frac{\partial}{\partial z}\frac{1}{m*(z)}\frac{\partial}{\partial z}\psi(z)+V(z)\psi(z)=E\psi(z)$$

APPLY THE FINITE DIFFERENCE APPROXIMATIONS

$$\left.\frac{\partial^2 f}{\partial z^2}\right|_z \approx \frac{f(z+\delta z)-2f(z)+f(z-\delta z)}{(\delta z)^2}$$

$$\left.\frac{\partial f}{\partial z}\right|_z \approx \frac{f(z+\delta z)-f(z-\delta z)}{2\delta z}$$

ESTABLISH THE Z DOMAIN AND THE INITIAL CONDITIONS

$$\psi(z-\delta z)=0 \quad \text{and} \quad \psi(z)=1$$

$$E_i=\delta E$$

$$z_{max}, z_{min}, \text{ and } \delta z$$

OBTAIN AND SOLVE THE SHOOTING EQUATION

$$\frac{\psi(z+\delta z)}{m*(z+\delta z/2)}=\left\{\frac{2(\delta z)^2}{\hbar^2}[V(z)-E]+\frac{1}{m*(z+\delta z/2)}\right.$$
$$\left.+\frac{1}{m*(z-\delta z/2)}\right\}\psi(z)-\frac{\psi(z-\delta z)}{m*(z-\delta z/2)}$$

$$z=z+\delta z$$

NO — **HAS z REACHED THE POSITIVE LIMIT?**

$$z=z_{max}$$

YES

$$E=E+\delta E$$

NO — **HAS THE WAVEFUNCTION SWITCHED THE DIVERGENCE DIRECTION?**

$$\left(\psi(E)\big|_{z\to+\infty}\right)\left(\psi(E+\delta E)\big|_{z\to+\infty}\right)<0$$

YES

REFINE THE ENERGY STEP AND SOLVE

$$\psi(E)\big|_{z=z_{max}}=0$$

$$E_{i+1}=E_i-\frac{\psi(E_i)\big|_{z\to+\infty}}{\psi'(E_i)\big|_{z\to+\infty}}$$

$$E=E+\delta\delta E$$

NO — **HAS THE ENERGY CONVERGED?**

$$|E_i-E_{i-1}|\le 1\text{ meV}$$

YES

NO — **IS THE ENERGY GREATER THAN THE BARRIER HEIGHT?**

$$E_i>V_0$$

YES

END

Confined Energies, E_i
Wavefunctions, $\psi_i(z)$

Figure 11   Schematic diagram of the shooting method procedure.

The shooting method was implemented in Matlab to obtain the confined energy levels and its respective wavefunctions of single-period heterostructures. Routines containing the material properties of the GaAs and InP system were also programmed to support the calculations. To validate the code, several different structures from the literature were solved and the results were found in good agreement. Figure 12 shows the conduction and the valence band confined energy levels and their respective wavefunctions

of a single step well studied in [51]. The structure dimensions and composition are also shown in the same figure. The wavefunctions have been rescaled for visual purposes.
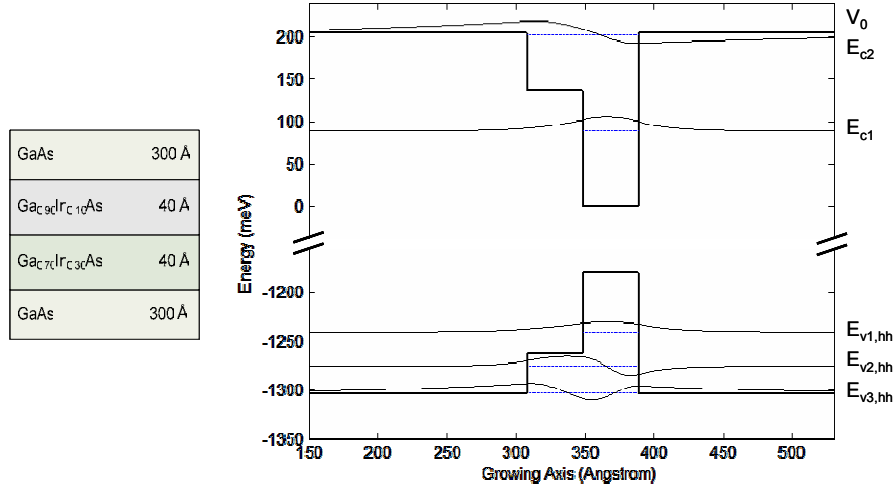
Figure 12   The calculated wavefunctions of the confined energy levels of the asymmetric step well studied in [51].

Figure 13 shows the conduction band confined energy levels and their respective wavefunctions of a more complex configuration, studied in [53]. The structure consists of three different-size coupled quantum wells separated by thin barriers. The dimensions and composition are shown in the same figure.

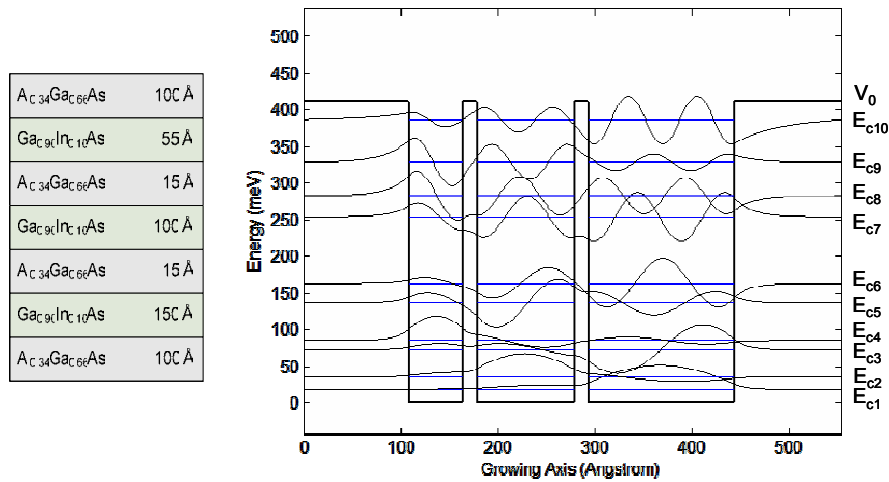Figure 13   The calculated wavefunctions of the confined energy levels of the triple-coupled quantum well studied in [53].

54

The results show that this implementation of the shooting method is valid for the configuration of interest of this thesis and, moreover, it can handle complex coupled structures. Also the effects of the potential bending due applied bias and charge distribution can be included since the method is applicable for any potential profile. This is very appropriate for self-consistent solutions as shown in the next section.

4. Charge Distribution Potential Evaluation

The carrier distribution in a quantum well depends on the quasi-Fermi level, E_F, within the well. The basic idea to determine it was mathematically described in the Section II.A.5. Since it is desired that there be only two confined states in the conduction band, using Equation (2.34), it is possible to express the total number of electrons as [5]

$$N_s = \frac{k_B T}{\pi \hbar^2} \left(m_1^{av} * \ln \left[1 + e^{\frac{E_F - E_1}{k_B T}} \right] + m_2^{av} * \ln \left[1 + e^{\frac{E_F - E_2}{k_B T}} \right] \right) \tag{3.21}$$

were E_1 and E_2 represents the first and second bound states, respectively, and $m_i^{av} *$ is the average effective mass, accounting on the probability of the electron location along the structure, for each energy level. It can be evaluated through [5]

$$m_i^{av} * = \sum_{i=1}^{N_l} \left[m_i * \int_{l_i} \psi_i *(z) \psi_i(z) \, dz \right], \tag{3.22}$$

where the effective mass of the ith layer, $m_i *$, is weighed by the total probability of finding an electron at that layer, represented by the integral term. Since the total number of carriers can be obtained directly by the doping concentration, the only unknown in Equation (3.21) is the quasi-Fermi energy. Using the iterative Newton's root finder to solve the equation

$$f(E_F) = N_s - \frac{k_B T}{\pi \hbar^2} \left(m_1^{av} * \ln \left[1 + e^{\frac{E_F - E_1}{k_B T}} \right] + m_2^{av} * \ln \left[1 + e^{\frac{E_F - E_2}{k_B T}} \right] \right) = 0 , \tag{3.23}$$

where the first guess of E_F can be obtained considering, initially, only the first state populated ($T = 0$), which is given by [5]

55

$$E_F^{ini} = E_1 + k_B T \log\left(e^{\left(\frac{-N_s \pi \hbar^2}{m_1^{av} * k_B T}\right)} - 1 \right). \tag{3.24}$$

Hence, a better estimate can be obtained by repeating [52]

$$E_F^{i+1} = E_F^i - \frac{f(E_F^i)}{f'(E_F^i)} \tag{3.25}$$

until the convergence. A tolerance of 1 meV is suitable for this evaluation.

Having calculated the quasi-Fermi level, the total number of carrier populating each subband is obtained using Equation (2.34). For very low temperature and deep wells, this can be avoided and it is reasonable to consider all electrons populating the ground state (first subband).

The next steps are to calculate the net surface charge density, the electric field along the structure, and finally the charge distribution potential. Those can be obtained directly from Equations (2.39), (2.40), and (2.36), respectively.

The evaluation of the charge distribution potential, through the Poisson's equation solution, sketched in Figure 14, becomes important in heavily doped structures, such as the proposed in this work. Also, the possibility to monitor non-measurable parameters such as electric field and charge density inside the structure, allows deeper physical analysis.
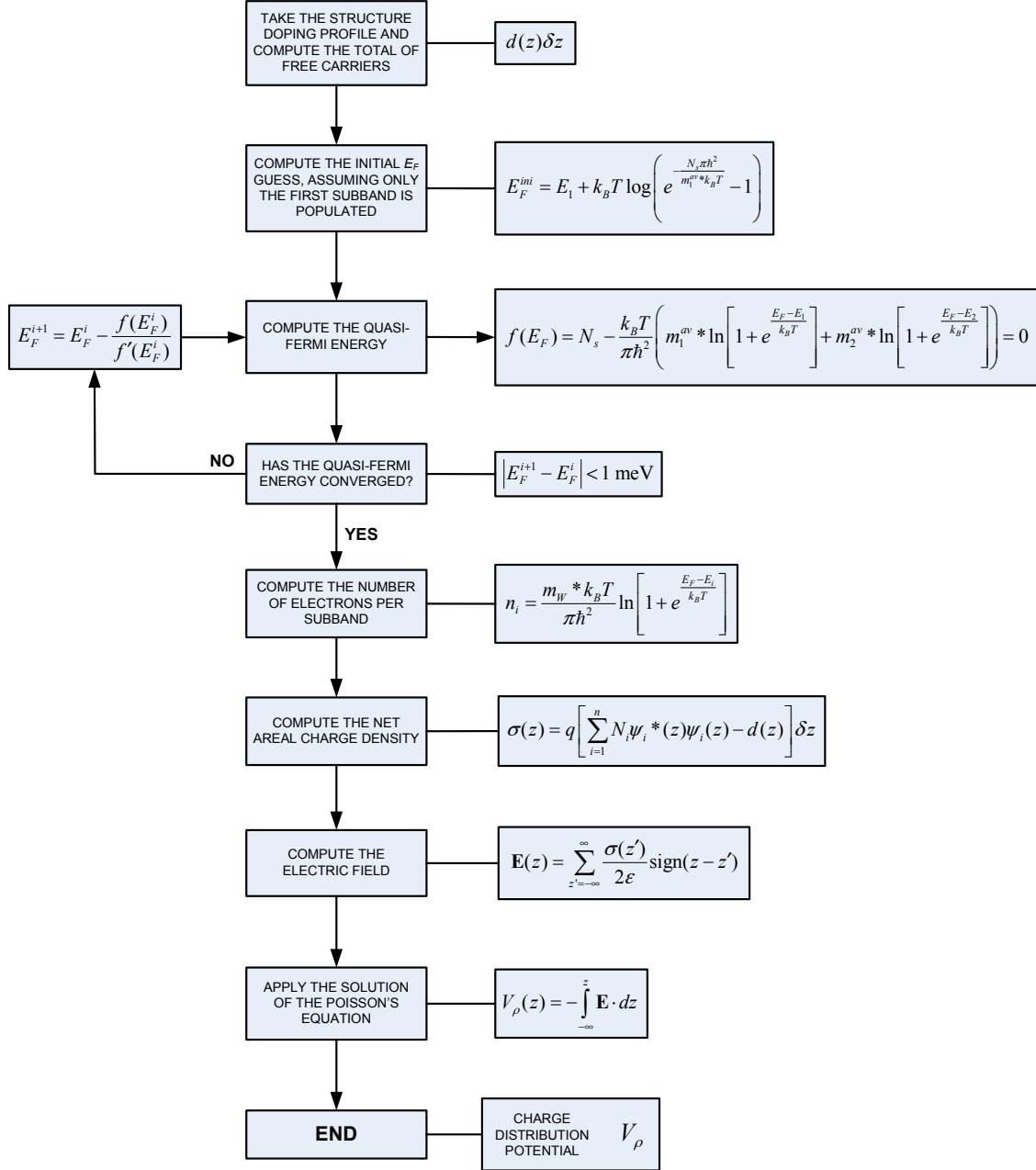
Figure 14 Schematic diagram of the charge distribution potential evaluation

The charge distribution potential computation was included in the Matlab code as part of the self-consistent approach. The self-consistent Schrodinger-Poisson program was validated through the solutions of several structures from the literature. The results were found in good agreement. For example, Figure 15 shows the potential profile, the confined energy levels and their respective wavefunctions for the structure studied in

[54]. Huang *et al* studied a GaAs-based step well with the barriers doped in the middle (modulation doping).

(a)   (b)
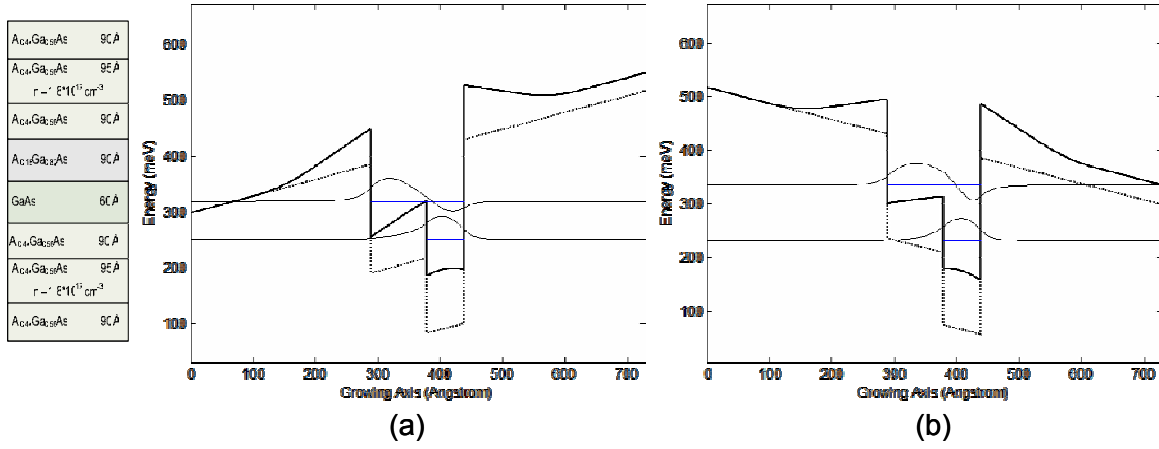
Figure 15   Self-consistent potential profile with normalized wave functions for the two lowest energy levels under a 30-kV/cm electric field (a) and a – 30-kV/cm electric field (b), for the structure studied in [54]. Dashed line is the potential profile without the charge distribution effects.

Figure 16 shows the individual potential contributions as well as the doping profile, charge density and electric field behaviors in the structure under a 30-kV/cm electric field, corresponding to Figure 15 (a).

Figure 16   Individual potential contributions in the structure (left) and the doping profile, charge density and electric field behaviors (right).

58

At this point, using the developed and validated computational tool, it is possible to calculate the confined energy levels and their respective wavefunctions of several types of heterostructures in a wide variety of configurations. Furthermore, using the absorption coefficient expressions derived in Section II.A.6, it is also possible to estimate the absorption 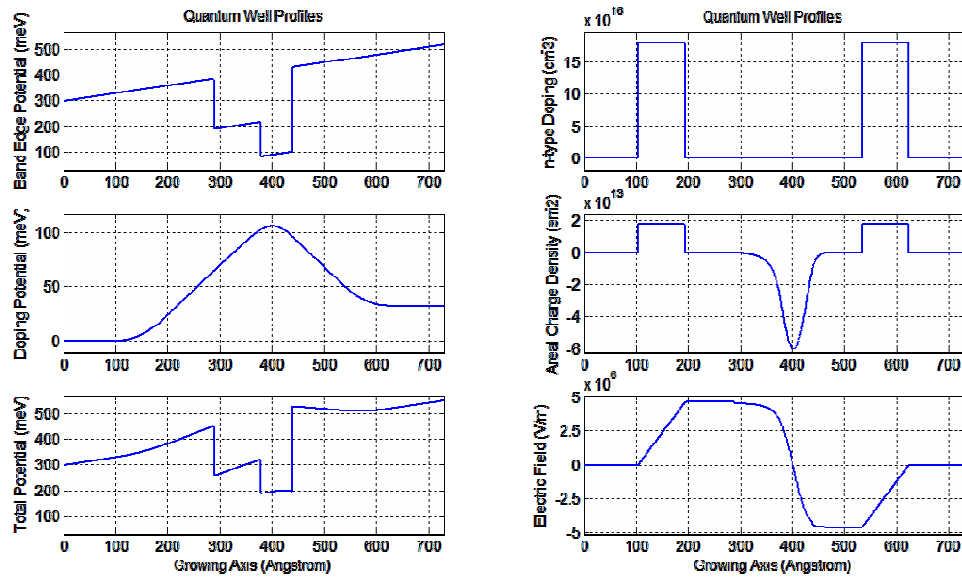coefficient of the quantum well systems. This was done for both the GaAs and the InP systems, considering the guidelines discussed in Section III.A in order to maximize the absorption coefficient on the spectral regions of interest. The next section brings this discussion and the final designed structure configurations.

E. DESIGN OF THE QWIP SEMICONDUCTOR HETEROSTRUCTURES

The computational tools developed to support this work are not optimized for design purposes. Optimization algorithms must be considered and more computational capability must be available to obtain that. However it is possible to select the configurations and material composition based on the arguments listed in Section III.A and to run the programs to analyze the results. Changes in the inputs must be made based on the physical properties and the desired result. After some interactions it is possible to refine the inputs to obtain the desired outputs (requirements). This was done for both systems aiming to maximize the absorption coefficient, placing the peak at the desired wavelength.

1. GaAs System

In terms of available technology and cost predictions, the GaAs-based configuration is the most attractive. In view of the guidelines and taking into account the limitations discussed in Section III.A, the following design requirements were set for the detectors based on GaAs system:

a.   The peak absorption of the three different bands for temperatures below 77K should be: the maximum value obtainable for NIR (limited by the GaAs bandgap); as close as possible to 5.0 μm for MWIR (limited by the grating pattern); and below 9.0 μm (limited by the grating pattern and leakage current due to thermoionic emission).

b.   Bound-to-quasibound transitions should be preferred to minimize the possibility of thermoionic transitions, maximize the oscillator strength and reduce the amount of bias needed for photocurrent readout.

c.   The stacks of each band should be limited to 20 repetitions of the basic *barrier/well/barrier* cell (due to the complexity to fabricate and to process a large amount of different crystal layers).

d.   The stacks should be grown onto the substrate in the following sequence: NIR, MWIR, and LWIR. This is to prevent the undesired absorption mechanisms from sequentially blocking the IR bands of passing through their respective detector stacks. Thus, the longer bandgap stacks should be placed before (bottom) the smaller ones. Also, the MWIR and LWIR should be the second (mid) and the third (top) in order to apply the respective grating pattern.

e.   The indium compositions in $In_xGa_{1-x}As$ as well as the aluminum compositions in $Al_xGa_{1-x}As$ should be restricted to no more than 3 different values each in the entire crystal. This is due to MBE growing limitations discussed previously.

f.   The contact layers should be heavily n-doped (about 2.10^{18} cm^{-3}) in order to improve the contact uniformity in long pixels.

g.   The cap layer (top) and the contact layer between the MWIR and LWIR quantum well stacks should be thick enough to allow the application of the respective grating patterns.

Following the considerations given above, several trials were executed varying the dimensions and the compositions of each band separately. The final stack configurations with the respective energy and detection wavelength are shown in Figures 17, 18, and 19. Its important to remark that, since the photodetectors operate cooled, all the design computations were carried using 77K material parameters.

Figure 17   Parameters of the NIR quantum well stack (left) and its respective basic cell potential profile with the confined energy levels (right).

The NIR quantum wells are basically asymmetric step wells where the overlap between the initial (valence band) and final (conduction band) envelope functions, the major contributor for the strength of the transition, was maximized, bounded by the limit in indium concentration and the location of the conduction band exited state. The well is not doped to minimize the undesired intersubband transitions.

The MIR quantum wells are basically symmetric step wells where the intersubband oscillator strength was maximized, bounded by the same parameters of the previous configuration. In this case, two GaAs layers were placed on the sides of the $In_{0.25}Ga_{0.75}As$ layer to better accommodate the $Al_{0.40}Ga_{0.6}As/In_{0.25}Ga_{0.75}As$ lattice constant mismatch and to reduce the amount of indium in the structure. All the three layers of the well were heavily doped to increase the absorption coefficient.

61
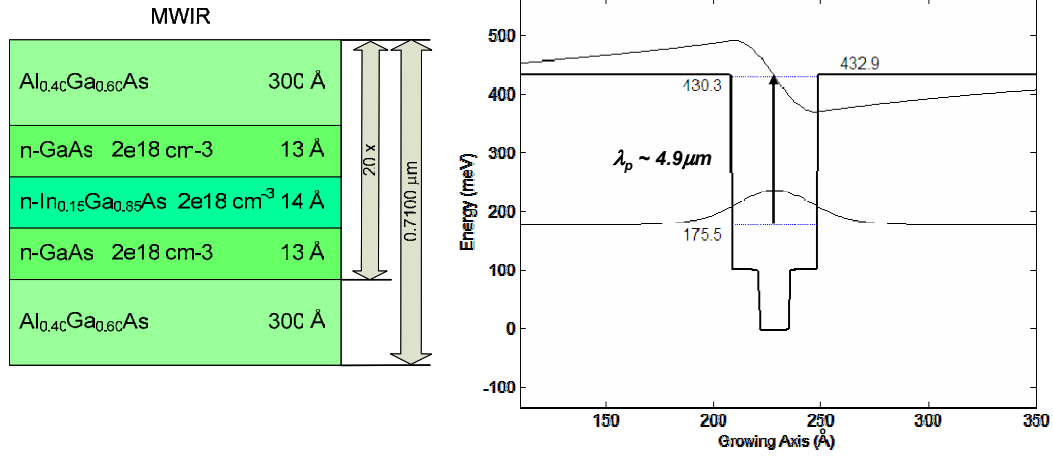
Figure 18   Parameters of the MWIR quantum well stack (left) and its respective basic
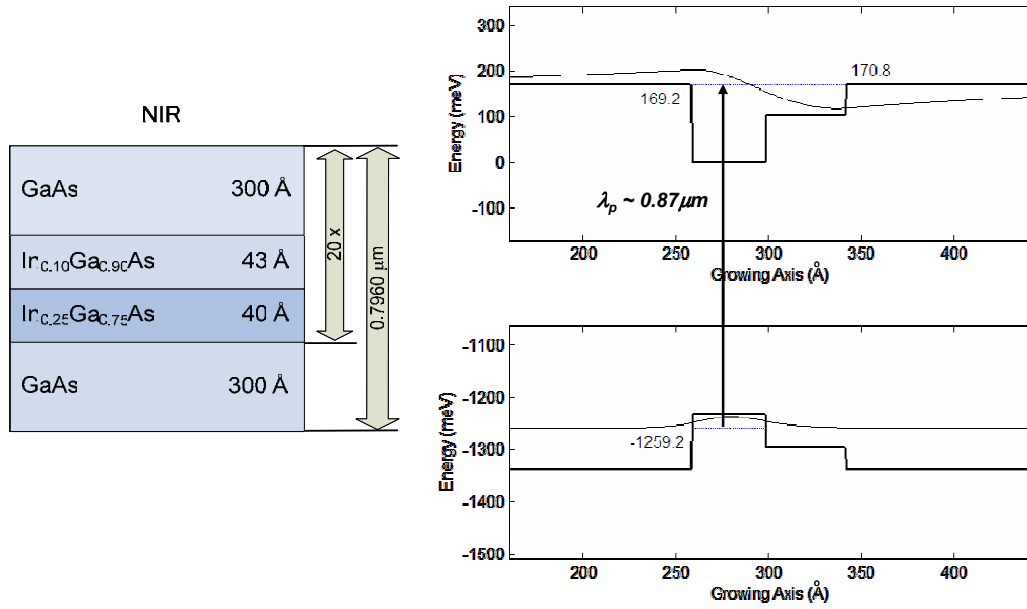cell potential profile with the confined energy levels (right).
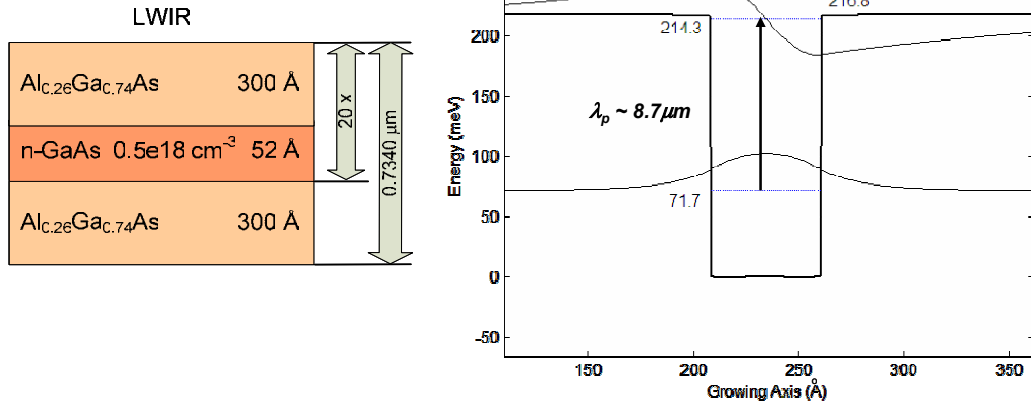
Figure 19   Parameters of the LWIR quantum well stack (left) and its respective basic cell
potential profile with the confined energy levels (right).

The LWIR quantum wells are symmetric and shallow square wells where the doping concentration was kept lower than the previous configuration to reduce the leakage current due to thermoionic emission. This is a very common GaAs/AlGaAs configuration [28].

The entire structure is composed by 68 layers, including the substrate. Table 1 compiles the parameters needed to grow the crystal. The band diagram of the structure is

shown in Figure 20. The allowed transitions for each quantum well configuration are also depicted and those maximized by design are highlighted. Notice that, in the figure, the layer numbers correspond to those in the Table 1.

Table 1   GaAs based QWIP sample description.

|	PROFILE		THICKNESS Å	DOPANT	CONC. ±10%
1	n-GaAs		7,000	Si	2×10^{18} cm^{-3}
2	i-Al$_{0.26}$Ga$_{0.74}$As	X20	300	None	------------------
3	n-GaAs		52	Si	0.5×10^{18} cm^{-3}
4	i-Al$_{0.26}$Ga$_{0.74}$As		300	None	------------------
5	n-GaAs		5,000	Si	2×10^{18} cm^{-3}
6	i-Al$_{0.40}$Ga$_{0.60}$As		300	None	------------------
7	n-GaAs	X20	13	Si	2×10^{18} cm^{-3}
8	n-In$_{0.15}$Ga$_{0.85}$As		14	Si	2×10^{18} cm^{-3}
9	n-GaAs		13	Si	2×10^{18} cm^{-3}
10	i-Al$_{0.40}$Ga$_{0.60}$As		300	None	------------------
11	n-GaAs		5,000	Si	2×10^{18} cm^{-3}
12	i-GaAs		300	None	------------------
13	i-In$_{0.10}$Ga$_{0.90}$As	X20	43	None	------------------
14	i-In$_{0.25}$Ga$_{0.75}$As		40	None	------------------
15	i-GaAs		300	None	------------------
16	n-GaAs		7,000	Si	2×10^{18} cm^{-3}
17	S.I. GaAs Substrate		-----------------	------------	------------------
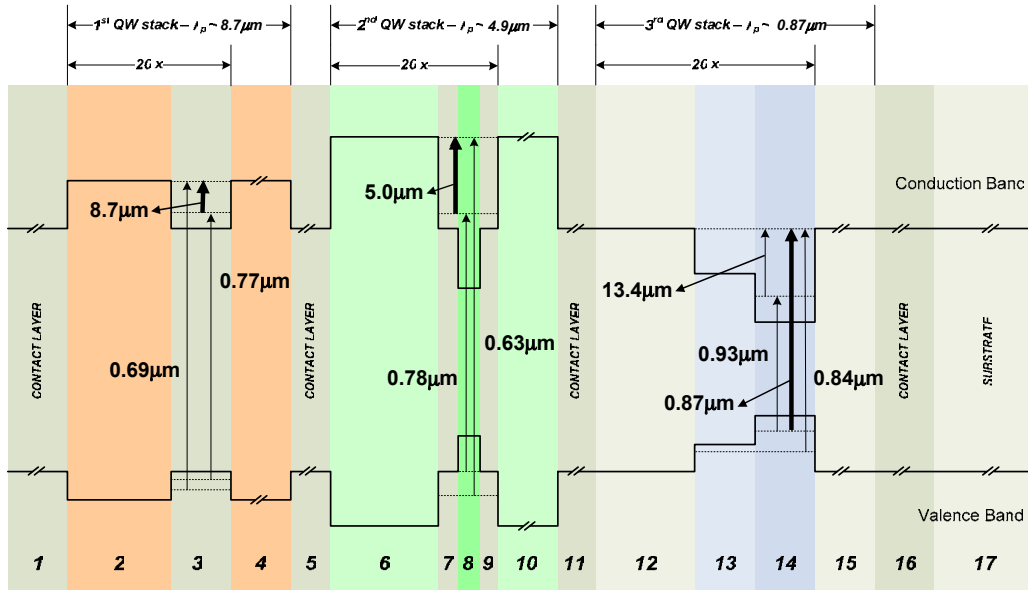
Figure 20   Band diagram of the GaAs based QWIP sample. The layer numbers correspond to those described in Table 1.

Despite the restrictions imposed by the limitations thoroughly discussed, the GaAs-based sample was fabricated by means of contract by IQE Inc. and succeeded in covering part of the three desired spectral regions (the results are presented and discussed in the next chapter). To some extent, the InP system presents even more restrictions, as described in the following section.

2. InP System

Semiconductor structures on InP substrates are more difficult to grow, fabricate, and process. Furthermore the band offset data, one of the most important parameter in designing QWIPs, is very controversial, as mentioned before, making the risk in such attempts, very high. Nonetheless, the bandgap of InP is smaller than GaAs, making this choice very attractive for the NIR region. In addition, the lattice matched combinations eliminate the strain restrictions widening the design possibilities.

Again considering the discussed possibilities, restrictions, and the lessons learned with the GaAs based sample results (discussed in the next chapter) the following design requirements were set for the detectors based on InP system:

a.   The InP based QWIP should detect only two IR spectral regions instead of three originally set. This is in attempt to reduce the complexity and consequently the costs,

b.   The peak absorption of the two different bands should be: above 1.2 μm and below 1.3 μm for NIR (to verify the ability to detect higher wavelengths in this band, allowing the necessary room to accommodate the band offset uncertainties), and as close as possible to the middle of the band for MWIR ($\sim$4.0 μm).

c.   For the MWIR quantum wells, it would be preferable to use the ternaries $In_{0.53}Ga_{0.47}As$ (well) and $Al_{0.48}In_{0.52}As$ (barrier) due to the consistency in their properties data [20].

d.   Bound-to-continuum transitions should be preferred to broaden detection spectrum of the MWIR detection.

e.   The stacks of each band should have no more than 40 and no less than 30 repetitions of the basic *barrier/well/barrier* cell. This is to increase the absorption coefficient peak, naturally lower than the previous design, caused by the bound-to-continuum transitions.

f.   The stacks should be grown onto the substrate in the following sequence, NIR and then MWIR. Beyond the reasons mentioned in the previous design, the MWIR has to be on the top of the device to receive the grating pattern.

g.   The contact layers doping concentration should be reduced (1.10^{18} cm^{-3}) in contrast to the GaAs-based QWIP, to reduce the probability of electrons diffusing to lower potentials, populating the non-doped wells. This was experienced in the GaAs-based sample. Also the bottom layer should be p-doped in order to create a p-i-n structure and deplete of electrons the NIR wells reducing the possibility of undesired intersubband transitions even more.

h.   A stop-etch layer should be included right below the cap layer to improve the precision in processing the grating pattern. This was not considered in the previous design counting on the higher controllability on etching GaAs-based semiconductors.

Attempting to consider all the defined requirements, several trials (using the computational tool) were executed varying the dimensions and the compositions of each band independently. The final stack configurations are shown in Figures 21 and 22. The temperature considerations are the same as the previous design.

Similar to the previous design, the NIR quantum wells are basically asymmetric step wells. In this case, there are no strain limitations; the asymmetry is clearly higher than the GaAs sample, favoring the desired interband transitions. Again, the well is not doped to minimize the undesired intersubband transitions.
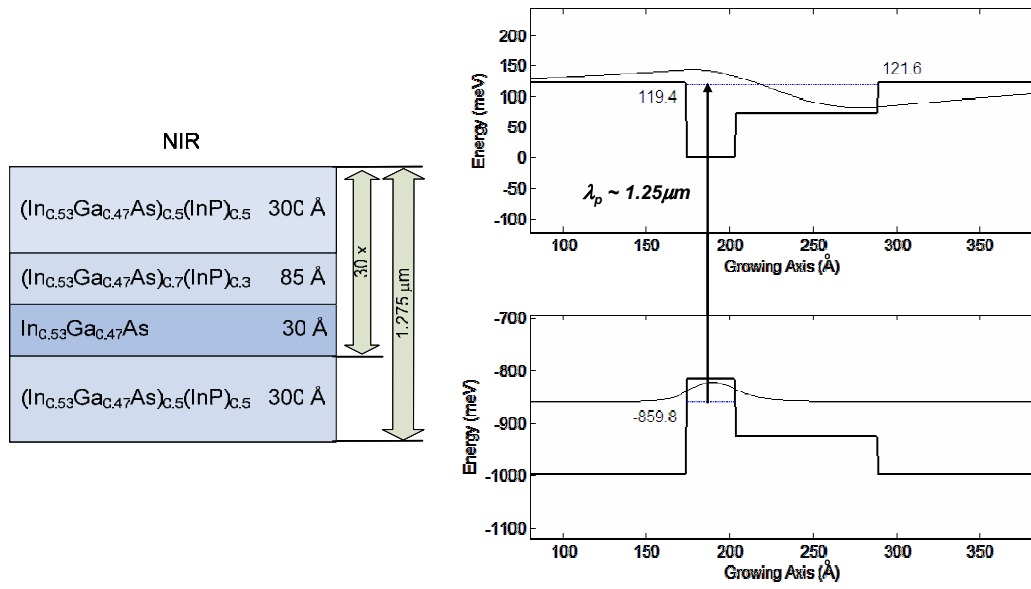
Figure 21   Parameters of the NIR quantum well stack (left) and its respective basic cell
potential profile with the confined energy levels (right).
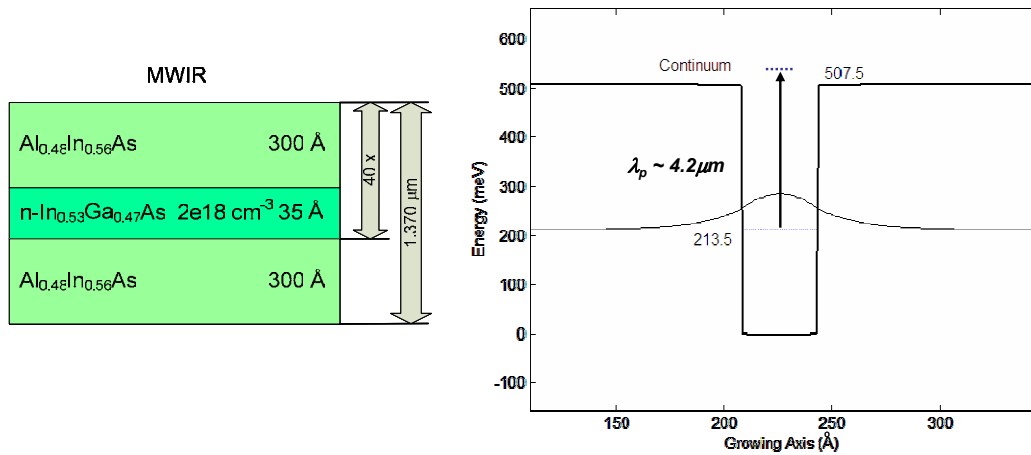
Figure 22   Parameters of the MWIR quantum well stack (left) and its respective basic
cell potential profile with the confined energy levels (side).

The MWIR quantum wells are highly doped, symmetric, and deep wells. In this
case there is only one confined level forcing the bound-to-continuum transitions. Notice
that the ternaries $In_{0.53}Ga_{0.47}As$ (well) and $Al_{0.48}In_{0.52}As$ (barriers) provide an absorption
peak very close to the middle of the band. Similar configurations were reported success-
fully in [32].

The entire structure is composed by 77 layers, including the substrate. Table 2 compiles the parameters needed to grow the crystal. The band diagram of the structure is shown in Figure 23. The allowed transitions for each quantum well configuration are also depicted, and those maximized by design are highlighted. Notice that in the figure, the layer numbers correspond to those in the Table 2.

Table 2   InP based QWIP sample description.

|	PROFILE		THICKNESS Å	DOPANT	CONC. ±10%
1	n-InP		3,800	Si	1×10^{18} cm^{-3}
2	n-Al$_{0.48}$In$_{0.56}$As		300	Si	1×10^{18} cm^{-3}
3	i-Al$_{0.48}$In$_{0.56}$As	X40	300	None	-----------------
4	n-In$_{0.53}$Ga$_{0.47}$As		35	Si	2×10^{18} cm^{-3}
5	i-Al$_{0.48}$In$_{0.56}$As		300	None	-----------------
6	n-InP		7,000	Si	1×10^{18} cm^{-3}
7	i- (In$_{0.53}$Ga$_{0.47}$As)$_{0.50}$(InP)$_{0.50}$		300	None	-----------------
8	i- (In$_{0.53}$Ga$_{0.47}$As)$_{0.70}$(InP)$_{0.30}$	X30	85	None	-----------------
9	i-In$_{0.53}$Ga$_{0.47}$As		30	None	-----------------
10	i- (In$_{0.53}$Ga$_{0.47}$As)$_{0.50}$(InP)$_{0.50}$		300	None	-----------------
11	p-InP		7,000	Be	1×10^{18} cm^{-3}
12	S.I. InP Substrate		----------------	------------	-----------------
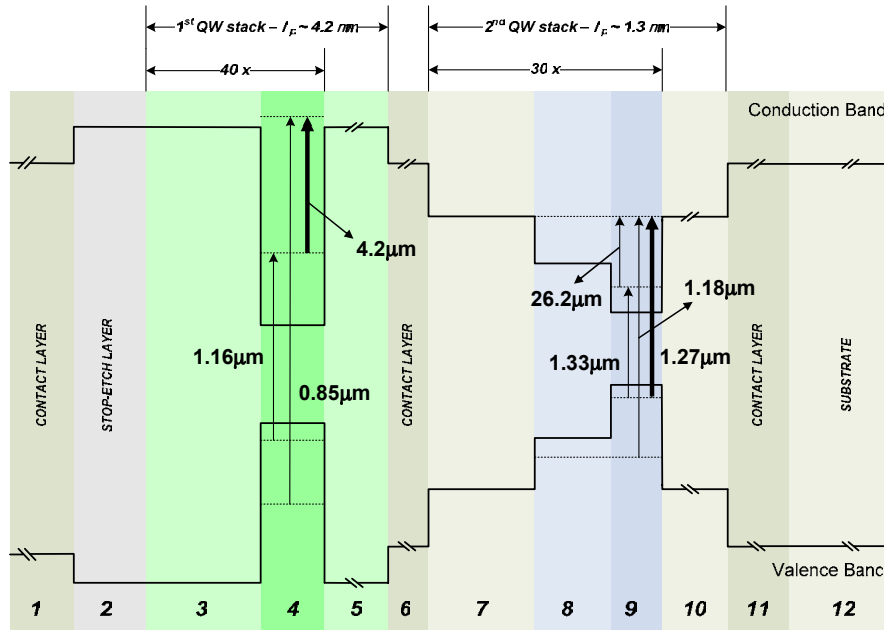
Figure 23   Band diagram of the InP based QWIP sample. The layer numbers correspond to those described in Table 2.

Although the InP sample is more attractive to meet the requirements, the implementation of such crystalline structure is very expensive and risky, due to the reasons previously discussed. In an attempt to make the photodetector feasible, it was restricted to a two-color detector and data as reliable as possible were used from [20], [32], and [45]. In addition, the feedback from the GaAs sample absorption measurements induced some changes in the design approach, making the InP a rich tool of learning. The sample was sent to fabrication and its characterization, testing and processing are matter for future work.

This chapter covered the aspects of the QWIPs' design. First, groups of semiconductors were analyzed and strained GaAs-based and matched InP-based systems proved more suitable to simultaneously detect the NIR, MWIR and LWIR. Heterostructures formed by stacks of uncoupled wells were chosen and the sequence of detection bands was defined. Second, considering the specificities of the selected configurations, computational tools were developed and the structure self-consistent Schrodinger-Poisson solutions were obtained by the shooting method. Finally, two QWIP samples were designed. The first, for three-color detection, is based on $GaAs/Al_xGa_{1-x}As/$ $In_xGa_{1-x}As$ on GaAs substrate and the second, for two-color detection, is based on $(In_{0.53}Ga_{0.47}As)_y(InP)_{1-y}/$ $Al_{0.48}In_{0.52}As$ on InP substrate. The GaAs-based sample was fabricated via contract by IQE Inc. and its characterization is addressed in the next chapter along with the design of the photodetector devices.

IV.   EXPERIMENTAL RESULTS AND FABRICATION

The GaAs QWIP sample was grown by way of contract by IQE Inc. using MBE on a semiinsulating GaAs wafer with 3 inches diameter, following the specifications discussed in the last chapter. The room temperature absorption measurements were carried out and the results are discussed in this chapter along with the optical coupling and the mask design for detector processing.

A.   ROOM TEMPERATURE ABSORPTION MEASUREMENTS

There are many ways to characterize QWIP samples. One way is to measure the transitions that can occur inside the crystal. As shown in Figure 20, the GaAs sample exhibits both interband and intersubband possible transitions. Cathodeluminescence and photoluminescence [12] can be used to measure interband transitions between ground states and Fourier transform infrared spectroscopy (FTIR) [11] can be used to measure interband transitions. Very comprehensible descriptions of the FTIR working principle are given in [11] and [53], and can be summarized as follows.

The infrared absorption measurements of the MIWR and LWIR bands were carried out in SRL using a Nicolet-750 FTIR. Unlike normal optical spectroscopy, which uses diffraction grating monochromators in the visible and ultraviolet, FTIR uses an Michaelson interferometer. A broadband radiation source is directed towards a beam splitter where the light is divided into two equal beams. One beam is directed to a fixed mirror and the other to a moving mirror. The beams are reflected back to the beam splitter which combines them and directs them towards the sample. A detector, placed behind the sample, measures the combined beam intensity after passing through the sample. [53]

In this configuration, the detector sees the original signal superimposed by a time-delayed copy of itself. This represents the autocorrelation function of the radiation field, commonly called interferogram. The spectrum is obtained by taking the Fourier transform of the interferogram. The center of the interferogram corresponds to the white light position (WLP), where the optical path is the same in both branches of the Michaelson interferometer. The entire source radiation band is reflected towards the sample. The phase

difference between partial waves outside the WLP is wavelength dependent. The spectral resolution of the FTIR is determined by the displacement length of the moving mirror. [53]

The FTIR spectrometer uses a computer to control the movable mirror and record the detector data. The mirror is moved through its entire range at a speed controlled by the user and the detected intensity is recorded as a function of data points. The data points are converted to a time scale using the velocity of the mirror and the sampling frequency. This procedure is repeated several times and the data are averaged to improve the signal-to-noise ratio. The controlling software performs the Fourier transform of the resulting interferogram. [11]

In order to obtain only the quantum wells' absorption, the undesired effects must be removed from the measured interferogram. That includes the atmospheric and bulk material absorptions. The easiest way to do that is to use a polarizer in front of the detector. By setting the polarization direction parallel to the quantum well layers, no absorption is expected from the quantum wells. Then, all that is measured is considered background and subtracted from the actual measurement.

The samples were prepared in the form of a 4.79 mm long, 13.6 mm wide and 0.66 mm thick waveguide by polishing 45° angle facets to enhance the absorption, following the same procedures described in [11]. The fabricated sample waveguide is shown in Figure 24.

The prepared sample is placed on a gold-plated holder that channels the infrared beam from spectrometer into the waveguide. The light enters the device normal to the 45° face, reflects through the waveguide and transmits out the opposing face (as depicted in Figure 24) towards the polarizer and detector.
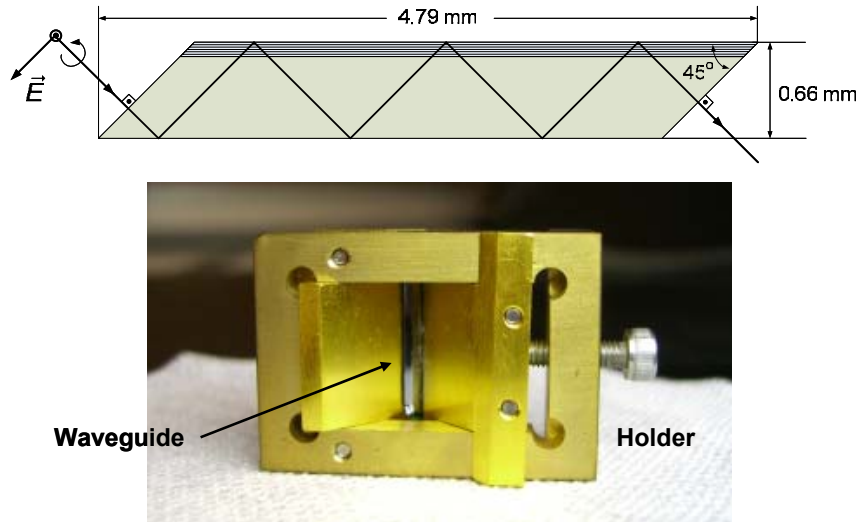
Figure 24   GaAs sample waveguide prepared for the absorption measurements. (Schematic diagram on the top and the actual sample on a holder on the bottom.

The absorptance of the sample was measured at room temperature at polarizations from zero (TM) to 90° (TE) at steps of 10°. The results are presented in Figure 25.
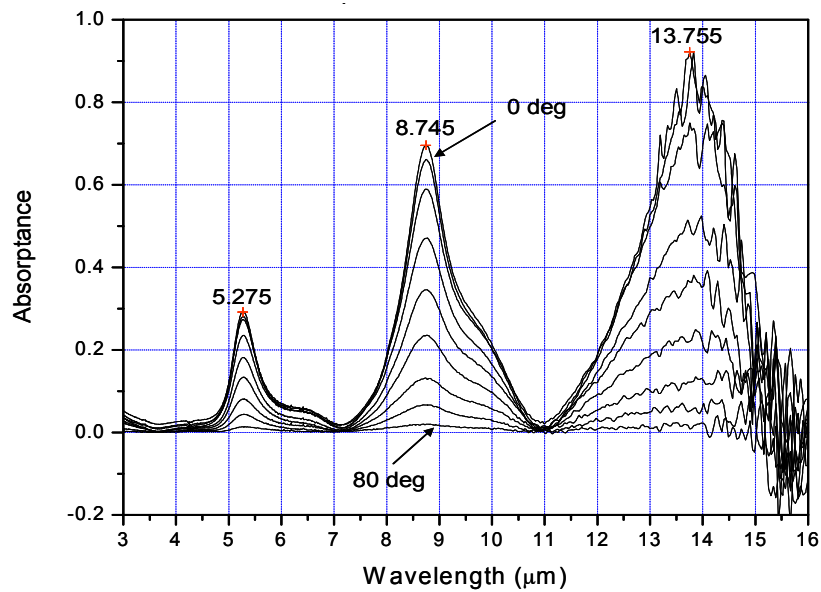

Figure 25   MWIR and LWIR absorptance of the GaAs based sample measured at 90° incident polarizations. The absorption peaks are highlighted.

The absorption peaks for MWIR and LWIR are 5.275 μm and 8.745 μm, respectively. Notice that the presence of an additional high LWIR absorption with peak around 13.8 μm. The presence of this absorption is discussed later in this section. The dependence of the absorption peaks strength with the polarization angle is shown in Figure 26. The absorption peak strength decreases with the square of cosine of the polarization angle, confirming that the absorptions are due to the quantum wells (discussion in Section II.A.6).
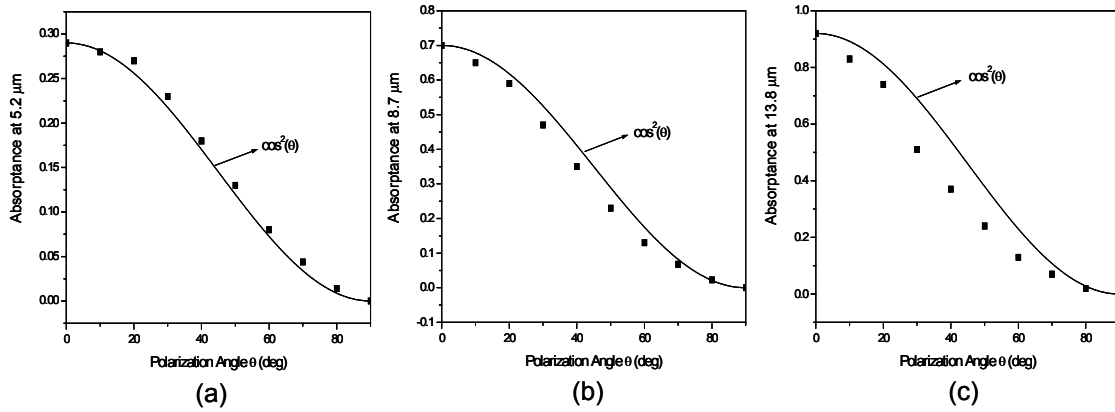
Figure 26   MWIR (a) and LWIR (b and c) absorption peak strengths as a function of the polarization angle.

At first view, some interesting facts can be identified. The MWIR absorption at 5.3 μm was expected to be stronger than the LWIR due to its higher doping concentration. The LWIR peak at 13.8 μm was not expected since the quantum wells responsible for that absorption are not doped (see Table 1 and Figure 20). A possible explanation for these observations is summarized in Figure 27.

The figure shows the configuration of the sample layers with their doping concentrations and the band diagram. The transitions of interest are represented by black arrows. The graphical insertion represents the measured absorption in the sample. The straight red arrows indicate which well stack is responsible for which absorption region. Also the unexpected LWIR absorption peak is highlighted along with its intersubband transition.

72

Figure 27   Schematic diagram of the effects of the electrons drift and tunneling to the NIR and LWIR, respectively, due to the high doping concentration of the contact layers.

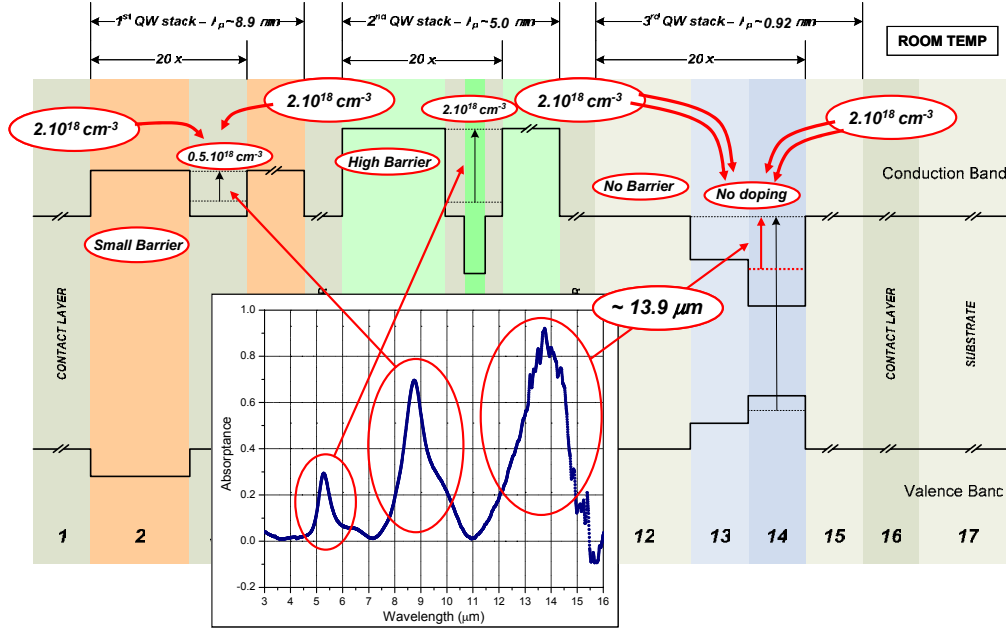Due to the difference in potential between layers, the electrons from the highly doped surrounding contact layers can diffuse into the NIR quantum wells (indicated in Figure 27 by the "curved" double red arrows), populating these wells with electrons, allowing the intersubband transition around 13.9 μm. Also, the electrons can tunnel through the AlGaAs barriers to the LWIR quantum wells (indicated in Figure 27 by the "curved" single red arrows), increasing the carriers' populations in those layers. With all quantum wells having nearly the same electron concentration, the strength of the transitions is directly proportional to the thickness of the layer and the transition wavelength. This explains the enhancement of absorption peak strength with increasing wavelength.

Those effects are undesired since they will contribute to increase in the dark current due to the high probability of thermoionic emission from shallow wells. One approach to avoid that in future designs is to reduce the contact layers doping concentration. In addition a p-doping in the bottom layer would make a p-i-n structure which depletes electrons in the NIR quantum wells, eliminating the probability of intersubband transition

there. This approach was used in the InP-based QWIP design, as discussed in Section III.E.2.

The absorption coefficient, α, can be obtained, for each band, given that the absorptance, A, is [11]

$$A = -\log_{10}\left(e^{-\alpha L_{wg}}\right),$$ (4.1)

where L is the path lengh through the quantum wells, represented by

$$L_{wg} = nNL\cos(45^\circ).$$ (4.2)

Here, n is the number of quantum wells in each pass, N is the number of passes and L is the well period. The absorption coefficient of the sample was computed and compared with the theoretical calculations as shown in Figure 28.
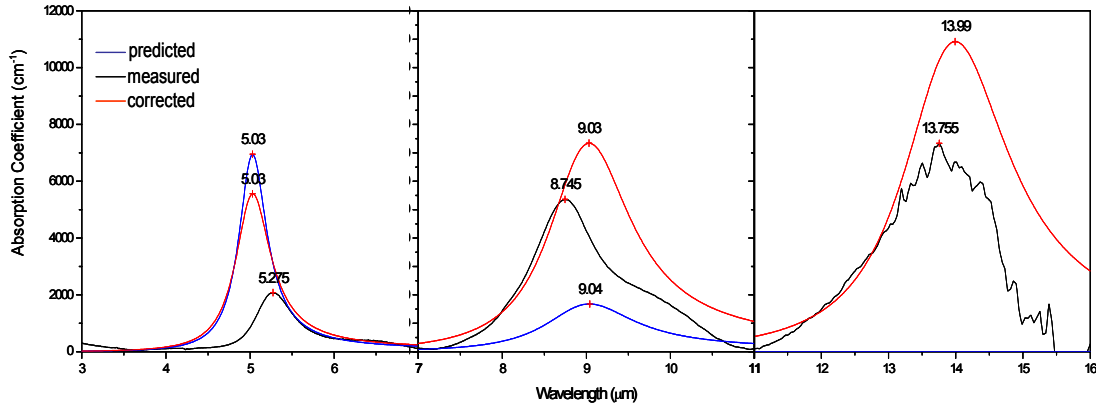
Figure 28   Comparison between the estimated and the measured MWIR and two LWIR absorption coefficients.

The blue curve is the estimated absorption using Equation (2.66) and $\Gamma = 20 \text{ meV}$. The red curve is the estimated absorption considering the effects of the diffusion and tunneling discussed above as well as using the measured broadening parameters. The uncertainties in the estimation of the absorption coefficient are several; however, it is possible to have an idea of the general behavior. Notice that in Figure 28 the red curve is shifted from the black by almost the same amount in all bands.

74

On the other hand, the estimated peak positions are within 0.3 μm of the measured values, which indicates the model gives good description of the absorption. A better visualization is possible, comparing the normalized curves, as shown in Figure 29.
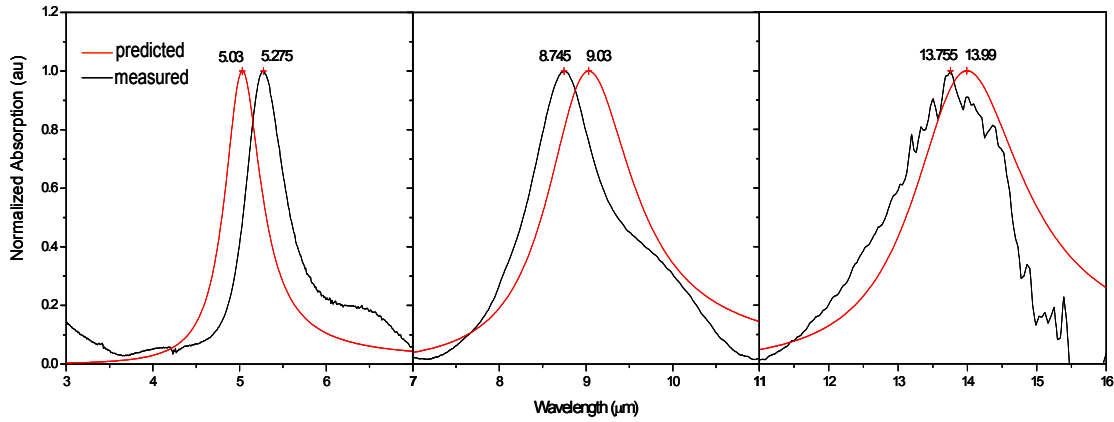
Figure 29   Comparison between the estimated and the measured MWIR and LWIR normalized absorption.

The FTIR measurement did not cover the NIR region due to the limitations on the equipment. However, the detection in this band can be characterized after the devices' fabrication through the responsivity measurement.

The absorptance measurement was important to confirm the MWIR and LWIR detection bands. Also the differences between the estimated and the measured absorption peaks can be used to refine the low temperature material parameters and design the optimized light coupling gratings. The recomputed low temperature absorption peaks are 5.0 μm and 8.5 μm. This is important because the grating acts as a narrow bandpass filter and, if not well tuned with the absorption peak wavelength, it can degrade the photodetector performance. The optical coupling design is addressed in the following section.

B.   OPTICAL COUPLING

As mentioned in Section II.A.6 and confirmed by the results showed in the previous section, the selection rules state that intersubband absorption cannot occur in symmetric structures, for TE mode incident radiation. In practical devices, detection of normal incident IR is desired. In this design it is required. The most efficient way, that has been reported [29] [30] [31] to overcome this selection rule, consists in etching diffraction gratings on the top of the device. Several configurations have being reported and the most common are: random grating [29], when pattern uniformity is the main goal (important for arrays); corrugated grating [30], when multi-band detection is the priority; and bi-directional ordered cross grating [50], when one band detection is desired. The later configuration is simpler than the others, in terms of fabrication, and it has shown potentialities for multi-band detection [55]. Therefore, bi-dimensional ordered grating was chosen for our GaAs-based QWIPs, to be implemented in two different patterns, one maximized for LWIR and other maximized for MWIR.

A thorough theoretical analysis is given in [55]. It is concluded there that the coupling efficiency is very sensitive to the grating period and the dimensions of the cavities. Several fabrication limitations, such as smallest possible dimension and precision in etching, compel us to employ a non-optimum grating with a simpler architecture [29].

Although the two grating parameters are dependent on each other [55], they are treated separately here without disturbing significantly the final result [29]. First the grating period is analyzed, followed by the area and depth of the groves. The parameters are optimized for the detection bands and adapted to meet the fabrication limitations.

A schematic diagram of the diffraction grating in a quantum well device is shown in Figure 30. There, the substrate, contact layers, a quantum well stack and a metal layer are sketched exactly as they are placed in actual devices. The dimensions are off-scale to better show the beam paths.

76
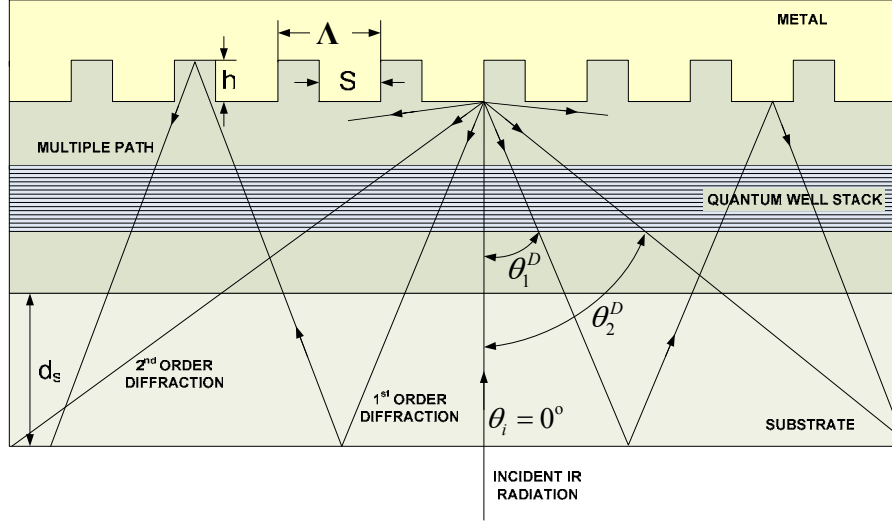
Figure 30   Schematic diagram of the diffraction grating

In the figure S represents the groove width, h represents the groove depth, and Λ represents the period of the grating. The backdiffracted beam angle of the ith order is given by the classical grating equation [56]

$$\sin \theta_n^D + \sin \theta_i = n \frac{\lambda}{n_r \Lambda} . \tag{4.3}$$

Here θ_i is the incident beam angle with respect to the normal, n is the diffraction order, and n_r is the refraction index of the material. Consequently, for normal incidence the diffracted angles exhibit the following dependence on the grating period:

$$\theta_n^D = \arcsin\left(n \frac{\lambda}{n_r \Lambda} \right). \tag{4.4}$$

According to Equation (4.4), the maximum first-order broadside diffraction occurs when the grating period has the same size of the incident wavelength inside the material. Hence, the optimum value of Λ is

$$\Lambda_{op} = \frac{\lambda}{n_r} . \tag{4.5}$$

Figure 31 shows the first- and second-order diffraction angle dependence on the grating period, normalized by the wavelength inside the material.

77
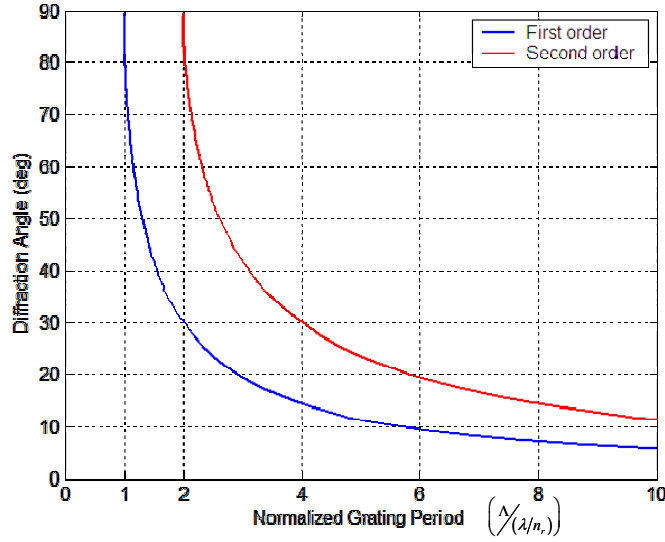
Figure 31   Variation of the first and second order diffracted angles with the normalized grating period.

The high sensitivity of the diffraction angles with the variation of the grating period is clearly shown in Figure 31, mainly for periods smaller than 1.5λ. This becomes important when the desired precision in fabrication cannot be obtained. Using $n_r^{GaAs} = 3.27$ in Equation (4.5), the optimum grating period for MWIR (peak at 5.0 μm) and LWIR (peak at 8.5 μm) were determined as 1.5 and 2.6 μm, respectively. The next step is to determine the area and depth of the groove.

The refraction grating can be viewed as two surfaces where one is retarded relative to the other by a distance h, the groove depth. If one surface area is u times smaller than the other, the area duty cycle turns out to be $1/(1+u)$. Using the same classical analysis used to compute the interference pattern of a Fabry-Perot etalon [56], the optical difference path, Δ_g, between two beams reflected by the two surfaces can be expressed as

$$\Delta_g = n_r h(1 + \cos\theta) \tag{4.6}$$

where θ is the angle between the diffracted beam and the normal (see Figure 30). Consequently, the electric field, proportional to the sum of the two beams can be written as

78

$$F_g \propto e^{ik(x+\Delta_g)} + ue^{ikx} \qquad (4.7)$$

where k is the wave vector and x is the arbitrary distance in the direction of k. The intensity is proportional to $F_g F_g^*$ and can be represented by

$$I_g \propto (1+u^2) + 2u\cos(k\Delta_g). \qquad (4.8)$$

An optimum grating is the one that minimizes the back reflection ($I_g \rightarrow 0$, when $\theta \rightarrow 0$) and maximizes the broadside reflection $(\theta \rightarrow 90°)$.

On one hand, when $\theta = 0$, the optical path difference reduces to

$$\Delta_g = 2n_r h, \qquad (4.9)$$

and Equation (4.8) can be rewritten as

$$\frac{(1+u^2)}{2u} = -\cos(2kn_r h) \quad \text{when } \theta = 0°. \qquad (4.10)$$

Since u represents a positive quantity and the left side of Equation (4.10) must be in the interval $(-1,1)$, the only possible value for u is one ($u_{op} = 1$), indicating that the projected area of the cavity openings should be one half of the total projecting area. Therefore, it is possible to determine the optimum value of h. This result is expressed as

$$h_{op} = \frac{\lambda}{4n_r} + n\frac{\lambda}{2n_r} \qquad n = 0, \ 1, 2, 3, \ ... \ . \qquad (4.11)$$

Figure 32 shows the back-reflected intensity due to grating effects. The parameters u and h are normalized by their deduced optimum values.
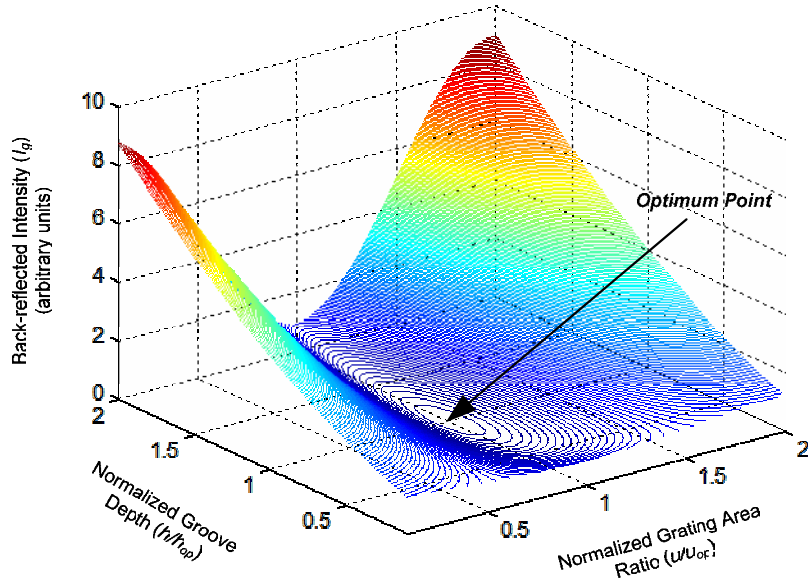
Figure 32   Intensity back-reflection due to diffraction grating.

It is rather interesting to observe the behavior of the backreflected intensity when *h* is varied. Figure 33 shows this dependence for the MWIR and LWIR detection peaks along with the GaAs QWIP layer structure.
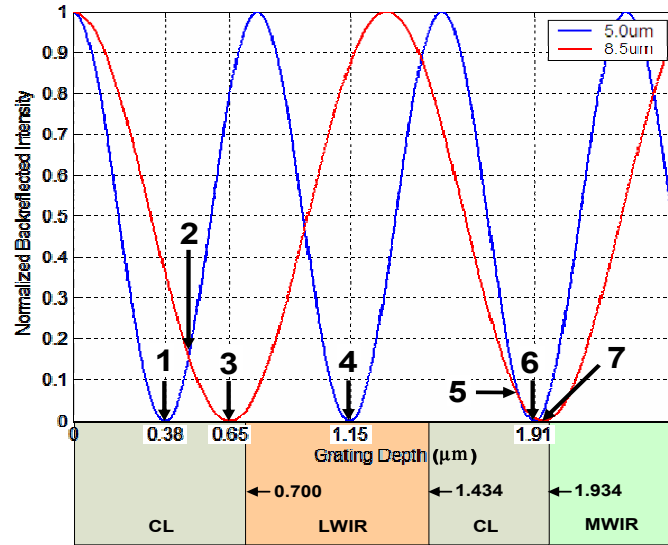
Figure 33   Dependence of the grating backreflected intensity on the cavity depth. The GaAs QWIP layers were placed right below the graph to compare the depth relative to the actual device.

In Figure 33, the optimum points for LWIR detection are points 3 and 7 and for MIWR detection are 1, 4 and 6, indicated by arrows. Points 2 and 5 are the best choices if a single grating would be applied for both bands. Due to fabrication limitations, the grating must be etched from the top of the wafer, while the sample is flat (i.e., before etching). Consequently, for LWIR the h value corresponding to point 1 should be selected. For MWIR, point 1 is intuitively the best choice; however, to be able to read the photocurrent for each band separately as indicated in Figure 7, the grating cavity must reach the second (from the top) contact layer in order to make contact and allow an independent readout. As a result, the only choice that maximizes LWIR is an h corresponding to point 6. This situation is depicted schematically in Figure 34.
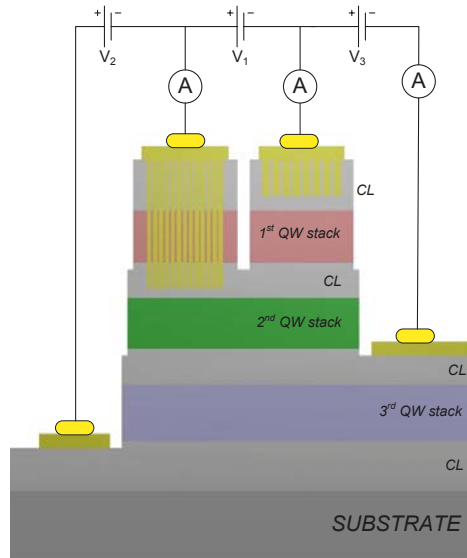
Figure 34   Schematic diagram of the grating configuration to allow three separate photocurrent readouts. The vertical is exaggerated for visual purposes.

An important factor that must be considered is the etching tolerance. Since in both points, 3 and 6 are very close to the respective quantum well stacks. Therefore a small reduction in the grating deepness should be considered in order to assure that the cavity will not reach the quantum wells, even though the grating efficiency degrades. The optimum and the selected values of h are in Table 3 in the end of this section.

To complete the grating specifications, the horizontal dimension of the cavity, as well as the distance between them must be computed. Figure 35 shows a schematic diagram of grating pattern. There, A_1 and A_2 represent the area to receive the grating pattern and the groove area, respectively, and x is the distance between grating squares, called the critical dimension (CD).
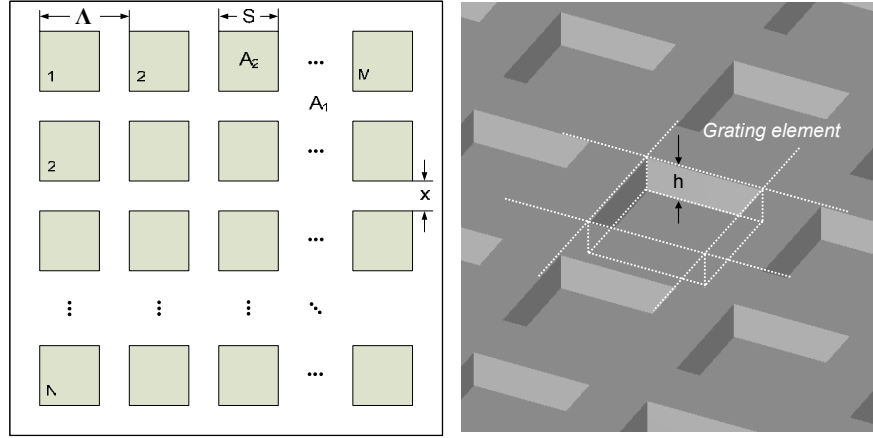
Figure 35   Schematic diagram of a bi-dimensional ordered grating pattern.

Considering that $u_{op} = 1$, the relationship between the areas A_1 and A_2, depicted in Figure 35 is

$$A_1 = 2(NM)A_2.$$

(4.12)

Using Equation(4.12) and after some algebra, the expressions for the dependence of the remaining parameters with relation to the grating period is given by

$$S = \frac{\Lambda}{\sqrt{2}}$$

(4.13)

and

$$x = 0.29\Lambda.$$

(4.14)

Having the grating period previously calculated, the remaining parameters were computed and the results were summarized in Table 3.

A restriction to the grating design is the minimum dimension that can be achieved during fabrication stage. Based on the limitations discussed in the next section, the minimum feature allowed in this design was set as $1\,\mu m$. The grating horizontal parameters were recalculated for $x = 1\,\mu m$ and the results are presented in Table 3. This imposes different losses in efficiency for each detection band as can be predicted using Figure 33.

Table 3   Grating parameters of the GaAs sample. (All units are μm)

	Optimum				Feasible (tolerance $= \pm\, 0.1\,\mu m$)			
	Λ	**S**	**x**	**h**	Λ	**S**	**x**	**h**
MWIR	1.5	1.1	0.45	1.91	3.4	2.4	1.0	1.8
LWIR	2.6	1.8	0.75	0.65	3.4	2.4	1.0	0.6

The grating design was an effort to allow the normal incidence detection for the QWIP devices. It was not an isolated task, since it is very dependent on the fabrication processes and the configuration of the devices. Actually an iterative work was necessary to adjust the grating to the devices and the devices to the grating fabrication possibilities. Although the parameters that maximize the detection on each band were degraded from their optimum values to make the devices feasible, normal incidence detection still can be achieved for both bands.

C.   DEVICES FABRICATION

The ultimate goal, after extensive work was to fabricate the photodetectors in order to execute the performance analysis for each band separately. The device fabrication sequence, procedures, rules, and limitations must be considered at the very first steps of heterostructure design. Initially, the knowledge of the processing possibilities and constraints can determine the thickness of the contact layers, the addition of stop-etch layers

in the structure, and even the sequence of the quantum well stacks. Lastly, the devices' shapes and configurations are strongly dependent on the processing issues.

Our devices will be fabricated by the National Research Council in Canada and their characterization is left for future work due to lack of time; however the photodetector configurations were defined and the mask layouts were drawn, based on the following requirements:

a. The mask plates should have the dimensions of be 4x4 inches (limited by the mask aligner).

b. The useful area of the masks cannot be grater than 44x26 mm (limited by the aligner)

c. The smallest feature permitted in the mask is 1.0 μm (limited by the mask fabrication costs and plate dimensions).

d. The grating patterns should be applied on the top of the wafer, while the surface is still flat enough. Consequently the grating etching should be the first step.

e. The devices should be grouped in not more than 4x4 mm (limited by the package).

f. The contact areas should be not less than 50x50 μm. This is a limitation imposed by the wire bonding equipment.

In addition, considering the necessity of three separate readouts and 2 grating patterns, the general processing sequence was defined [57], simulated using MEMS Pro v5.0 licensed for NPS. The results are shown in Figure 36.
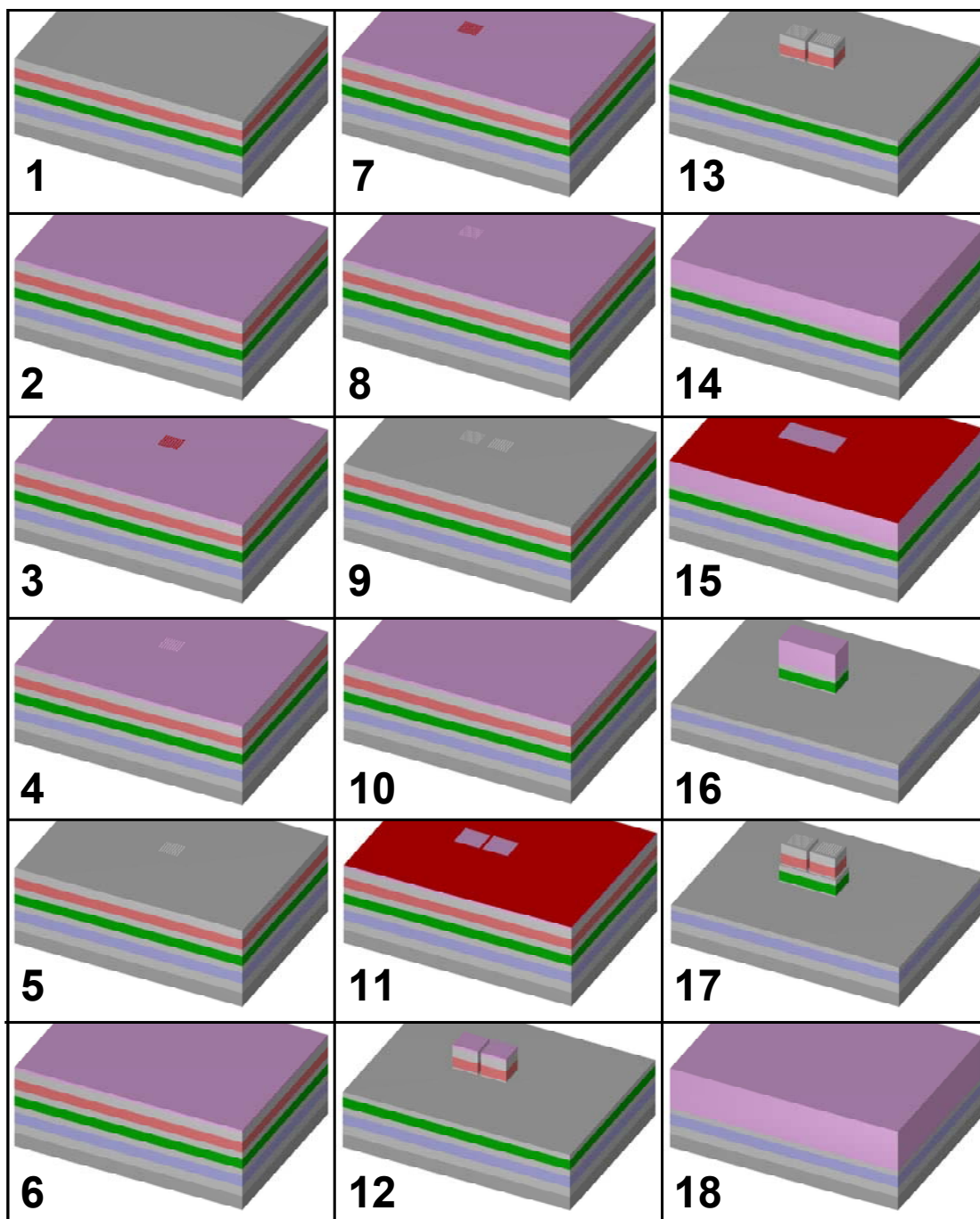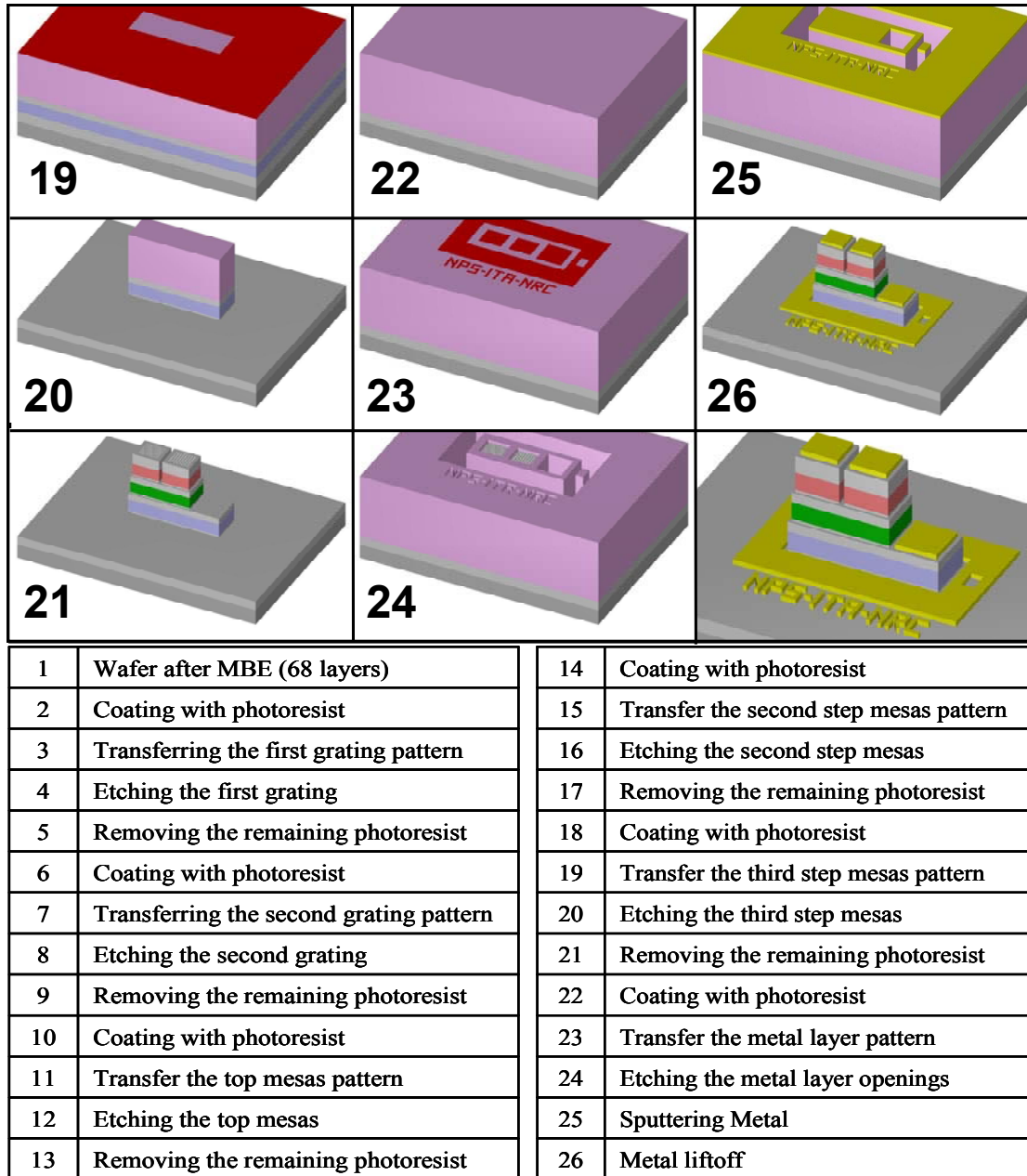
Figure 36   Photodetector devices fabrication sequence.

1	Wafer after MBE (68 layers)	14	Coating with photoresist
2	Coating with photoresist	15	Transfer the second step mesas pattern
3	Transferring the first grating pattern	16	Etching the second step mesas
4	Etching the first grating	17	Removing the remaining photoresist
5	Removing the remaining photoresist	18	Coating with photoresist
6	Coating with photoresist	19	Transfer the third step mesas pattern
7	Transferring the second grating pattern	20	Etching the third step mesas
8	Etching the second grating	21	Removing the remaining photoresist
9	Removing the remaining photoresist	22	Coating with photoresist
10	Coating with photoresist	23	Transfer the metal layer pattern
11	Transfer the top mesas pattern	24	Etching the metal layer openings
12	Etching the top mesas	25	Sputtering Metal
13	Removing the remaining photoresist	26	Metal liftoff

Finally, to be able to test several properties of the QWIPs such as three color detection, normal incidence detection, effects of contacts in long pixels, detection uniformity, effect of the bias in the detection band, grating pattern effect on the other band, and polarization and angle of incidence effects during the characterization phase, different photodetectors configuration were designed. Figure 37 shows the basic detectors.
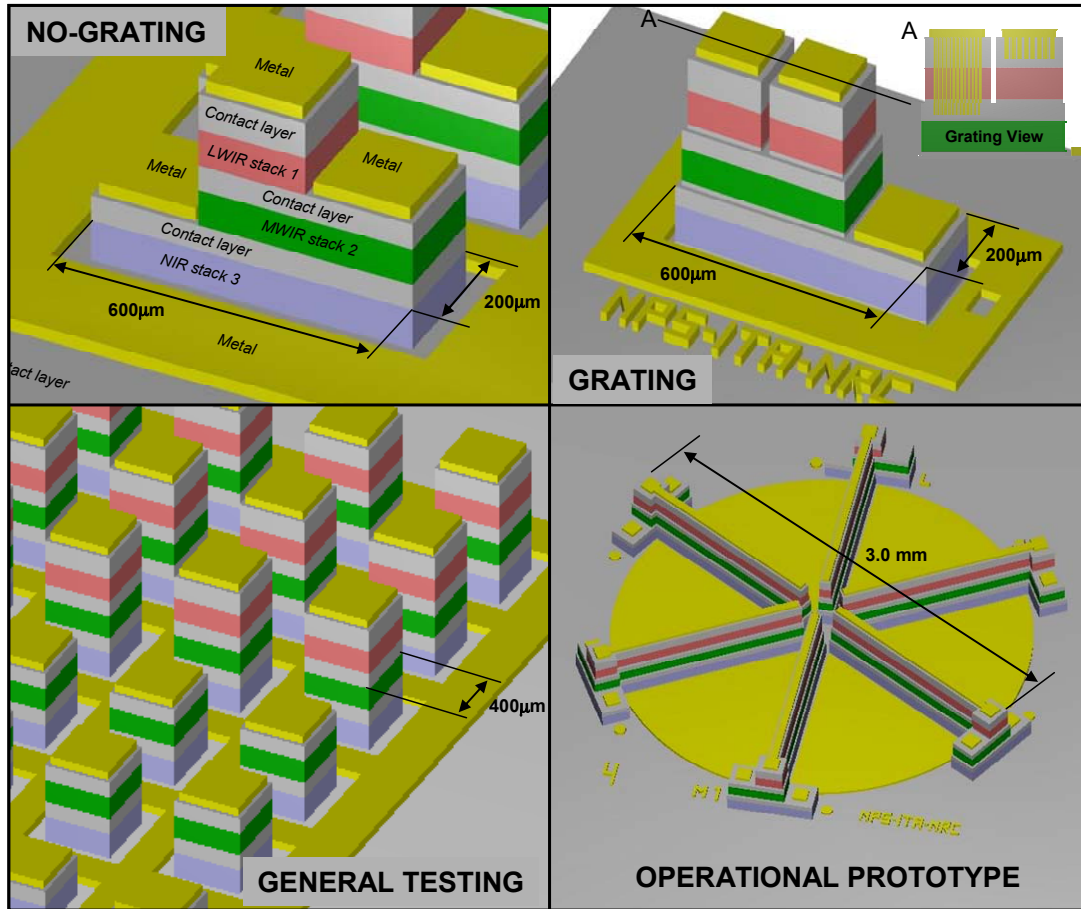
Figure 37   Photodetector devices configurations.

For practical reasons, the fabrication was divided in two phases. In the first phase, devices without gratings will be fabricated and in the second phase, after the preliminary tests, the devices with a grating pattern will be fabricated. However, to fit in the research budget, only two masks accommodating all layers necessary for both phases will be fabricated. The first mask is clear field with the features in chrome, for the mesas etching. The second mask is dark field with the features clear, for the grating patterns and metal layers.

The characterization of the devices will be carried out by SRL and the results will be published in future work.

This chapter presented the characterization of the GaAs-based QWIP sample, showing absorption on the desired bands and some effects of the doping and band struc-

ture of the sample. The results were important as feedback for the next designs. Having the structures tested and working, the optical coupling was designed for the optimum normal incidence detection. Limitations on the fabrication forced the final patterns to be away from the optimum points, but not compromising the overall proof-of-concept. Finally the photodetector devices were designed to permit the measurement of the figures of merit and several other effects. Despite the limitations, the design methodology defined during this research and the experimental results show a great potentiality of this approach, addressed in the conclusion chapter.

V. CONCLUSIONS

The realm of QWIP design is very extensive [28]. The advances in material sciences and semiconductor growth technology have allowed the use of bandgap engineering to cover, ideally, all IR bands [5]. Specifically in the area of QWIPs a great effort was made in the past 20 years to make those devices commercially available for several applications. High sensitivity, high selectivity, and multispectral detection capability are some of the properties of quantum well detectors that make those devices very attractive for military applications. The possibility of combine NIR, MWIR and LWIR in a single detector, motivated the work described in this documented in this text. The successful accomplishments along with the lessons learned and the future possibilities are discussed in this chapter.

A. FINAL CONSIDERATIONS

The purpose of this thesis was to study, to model, and to design a QWIP capable to detect three different IR bands within the wavelengths intervals of 0.9-1.4 μm, 3.8-5.0 μm and 8.0-12.0 μm. This objective was accomplished through the following steps.

In the first chapter, the background theory was organized in order do physically explain the quantum effects in semiconductor heterostructures that make possible the IR detection. The envelope function approximation was used to mathematically model the electron behavior under the influence of the band-offset and charge distribution potentials. The one-dimensional Schrodinger's equation was used to obtain the confined energy levels and their respective wavefunctions. The transitions between different states due to the incident IR radiation were identified and studied. The absorption coefficient was modeled for interband and intersubband transitions, and the strength and selection rules were identified. The effects of the electric field were also included in the mathematical models. The mechanisms of extraction of the electrons from the wells and leads to a photocurrent were also studied and modeled. After that, the main figures of merit, necessary to set requirements and to analyze the QWIPs performance were discussed.

The second chapter brings the practical design implications and procedures. The semiconductor material properties along with their availability were considered and two main material groups were selected to be used. GaAs/AlGaAs/InGaAs system showed easy in growth and fabrication while InP/AlGaAs/AlInAs system was capable of meeting the requirements for detecting the desired NIR band. A configuration of three uncoupled quantum wells stacks, one stack for each band, placed between highly doped contact layers, showed to be more suitable to allow separate readouts of the signals.

Considering the specificities of the configuration and materials, a computational tool was developed to solve self-consistently the Schodinger-Poisson equations for the structure. The shooting method was implemented due to its ability to handle any potential profile, necessary feature for QWIP designs. Finally, a GaAs based sample for three color detection, and a InP based sample for two color detection, were designed, taking into account the limitations on each configuration.

The GaAs sample was fabricated using MBE and the absorption measurements were presented in the fourth chapter. An FTIR spectrometer was used to measure the room temperature absorptance of the MWIR and LWIR bands, and the sample showed absorption in good agreement with the design predictions. Also the heavily doped contact layers introduced a second LWIR absorption band. The measured peaks, 5.3 μm, 8.7 μm and 13.8 μm varied less than 0.3 μm from the predicted values mostly due to the uncertainties in the material parameters.

The optical coupling structure was then designed to allow detection of the normally incident radiation. A bi-dimensional ordered grating pattern was selected and optimized separately for both MWIR and LWIR desired peaks. Constraints in mask fabrication and wafer processing forced the degradation of the grating performance, to make it feasible. Finally the photodetector device configurations were designed, to permit to performance analysis. The fabrication and characterization of the prototypes are matter for future work.

Despite the financial, temporal and technological limitations, normally present in any research, the objective of this thesis was successfully accomplished. However, further work needs to be done to finalize the devices' fabrication and testing and to improve

the mathematical models and the numerical algorithms to be able develop optimal detectors. This is summarized as follows.

B.   FUTURE WORK

The natural follow-on task of this research is the GaAs-based devices' fabrication. The designed configurations allow the analysis of the NIR absorption, through the photocurrent spectroscopy. In addition, figures of merit can be analyzed along with several effects such as: MWIR and LWIR grating efficiency, MWIR grating influence in LWIR detection, LWIR grating influence in MWIR detection, uniformity of grating patterns, incident radiation polarization effects, direction of incidence effects, etc. All the results can be used to optimize the design methodology and models to improve the design accuracy.

Another important aspect is the characterization of the InP-based sample. Since that design incorporates modifications induced by the feedback of the GaAs sample measurements, this would be the natural way to test and validate the new approach.

In addition, the models' weakness and points of improvement identified in the text can be summarized as following:

    a.   The numerical computations were done considering the valence non-degenerate with respect to the heavy and light holes' bands. The simplest way to include the degeneracy effects is to solve numerically the 4x4 $\mathbf{k \cdot p}$ Hamiltonian described in Equation (2.16) to obtain the valence band confined levels.

    b.   The heterostructure electrostatic potential was computed without accounting for the strain effects. This can be included in the model following the approach discussed in [53].

    c.   The absorption coefficient for interband transitions were computed only for the TE mode. The TM absorption can be included using a more rigorous approach suggested in [24].

d.   The Stark shift, included in the absorption coefficient algorithms was not properly verified against experimental results. This can be done along with the GaAs-based devices' responsivity measurements.

e.   The photocurrent as well as the figures of merit estimation should be included in the computational tools. The mathematical models can be refined after the GaAs-based devices characterization.

Finally, the work done through the models, computational tools and design approach discussed in this thesis, corroborated by the experimental results, can be iteratively improved by fabrication and characterization of new devices.

LIST OF REFERENCES

[1] D. Curtis Schleher, "Electronic Warfare in the Information Age," pp. 429-468, Artech House, Norwood, MA, 1999.

[2] Bruce Glasgow and William Bell, "The future of anti-aircraft imaging infrared seeker missile threats," *Proceedings of Airspace Conference 1999*, Vol. 4, pp. 457-465, IEEE Press, New York, 1999.

[3] Antoni Rogalski, "Third-generation infrared photon detectors," *Optical Engineering*. Vol. 42, No. 12, pp. 3498-3516, 2003.

[4] A. Rogalski, "Comparision of the performance of quantum well and conventional bulk infrared photodetectors," *Infrared Physics and Technology*, Vol. 38, pp. 295-310, 1997.

[5] Emanuel Rosencher and Borge Vinter, *Optoelectronics*, pp. 344-350, Cambridge University Press, London, 2002.

[6] L. Esaki and R. Tsu, "Superlattice and negative differential conductivity in semiconductors," *IBM Journal of Research and Development*, pp. 61-65, 1970.

[7] J. P. van der Ziel, R. Dingle, R. C. Miller, W. Wiegmann and W. A. Nordland Jr., "Laser oscillation from quantum states in very thin GaAs-$Al_{0.2}Ga_{0.8}As$ multilayer structures," *Applied Physics Letters*, Vol. 26, No. 8, pp. 463-465, 1975.

[8] Takashi Mimura, Satoshi Hiyamizu, Toshio Fujii and Kazuo Nanbu, " A new field-effect transistor with selectively doped GaAs/n-$As_xGa_{1-x}As$ heterojunctions," *Japanese Journal of Applied Physics*, Vol. 19, No. 5, pp. L225-L227, 1980.

[9] B. F. Levine, K. K. Choi, C. G. Bethea, J. Walker and R. J. Malik, "New 10 μm infrared detector using intersubband absorption in resonant tunneling GaAlAs superlattices," *Applied Physics Letters*, Vol. 50, No. 16, pp. 1092-1094, 1987.

[10] S. V. Bandara, S. D. Gunapala, J. K. Liu and S. B Rafol, "Four-band quantum well infrared photodetector array," *Proceedings of Device Research Conference 2003*, pp. 159-160, IEEE Press, New York, 2003.

[11] Michael P Touse, "Demonstration of a Near and Mid-Infrared Detector Using Multiple Step Quantum Wells," Master Thesis, Naval Postgraduate School, Monterey, CA, September 2003.

[12] Vu D. Hoang, "Charge Transport Study of INGAAS QWIPS," Master Thesis, Naval Postgraduate Scholl, Monterey, CA, June 2004.

[13] Kevin R Lantz, "Two-Color Photodetector Using an Asymmetric Quantum Well Structure," Master Thesis, Naval Postgraduate School, Monterey, CA, June 2002.

[14] Mihail Giannopoulos, "Tunable Bandwidth Quantum Well Infrared Photodetector (TB-QWIP)," Master Thesis, Naval Postgraduate School, Monterey, CA, December 2003.

[15] Thomas R. Hickey, "Temperature Dependence of Dark Current in Quantum Well Infrared Detectors," Master Thesis, Naval Postgraduate School, Monterey, CA, June 2002.

[16] A. Rogalski, *Infrared Detectors*, pp. 585-586, Gordon and Breach Science Publishers, Amsterdam, 2000.

[17] David J. Griffiths, *Introduction to Quantum Mechanics*, Second Edition, pp. 5-23, Pearson Education, Inc., New Jersey, 2005.

[18] Paul Harrison, *Quantum Wells, Wires and Dots: Theoretical and Computational Physics*, pp. 23-30, John Wiley & Sons Inc., New York, 2001.

[19] Michael Shur, *Physics of Semiconductor Devices*, pp. 38-42, Prentice-Hall, Inc., New Jersey, 1990.

[20] I. Vurgaftman and J. R. Meyer, " Band parameters for III-V compound semiconductors and their alloys," *Journal of Applied Physics*, Vol. 89, No. 11, pp. 5815-5875, 2001.

[21] M. O. Manasreh, Editor, *Semiconductor Quantum Wells and Superlattices for Long-Wavelength Infrared Detectors*, pp. 28-31, Artech House, Inc., Norwood, MA, 1993.

[22] K. K. Choi, S. V. Bandara, S. D. Gunapala, J. K. Liu and J. M. Fastenau, "Detection wavelength of InGaAs/AlGaAs quantum wells and superlattices," *Journal of Applied Physics*, Vol. 91, No. 2, pp. 551-564, 2002.

[23] A. Kastalsky, T. Duffield, S.J. Allen and J. Harbison, " Photovoltaic detection of infrared light in a GaAs/AlGaAs superlattice," *Applied Physics Letters*, Vol. 52, pp. 1320-1322, 1988.

[24] Shun Lien Chuang, *Physics of Optoelectronic Devices*, pp. 22-220, John Wiley & Sons, Inc., New York, 1995.

[25] D. D. Coon and G. Karunasiri, "New mode of IR detection using quantum wells," *Appied Physics Letters*, Vol. 45, pp. 649-652, 1984.

[26] B. R. Nag, *Physics of Quantum Well Devices*, pp. 77-138, Kluwer Academic Publishers, Netherlands, 2000.

[27] M. Helm, "The basic physics of intersubband transitions" in "Intersubband Transitions in Quantum Wells: Physics and Device Applications I," H. C., Liu and F. Capasso, Vol. eds., in *Semiconductors and Semimetals*, R. K.Willardson and E. R.Weber, eds., Vol. 62, pp. 1-91, Academic Press Inc., San Diego, 2000.

[28] B. F. Levine, "Quantum Well Infrared Photodetectors," *Journal of Applied Physics*, Vol. 74, No. 8, pp. 1-81, 1993.

[29] Shmuel I. Borestain, U. Arad, I. Lyubina, A. Segal and Y. Warschawer, "Optimized randon/ordered grating for an n-type quantum well infrared photodetector," *Applied Physics Letters*, Vo. 75, pp. 2659-2661, 1999.

[30] Kwong-Kit Choi, Kok-Ming Leung, Theodor Tamir and Carlos Monroy, "Light Coupling Characteristics of Corrugated Quantum-Well Infrared Photodetectors," *IEEE Journal of Quantum Electronics*, Vol. 40, No. 2, pp. 130-142, 2004.

[31] Chien-Ping Lee and Shiang-Yu Wang, "Normal Incident Quantum Well Infrared Photodetectors," *Proc. of 5th International Conference on Solid-State and Integrated Circuit Technology*, pp. 637-640, IEEE Press, New York, 1998.

[32] G. Hasnain, B. F. Levine, D. L. Sivco and A. Y. Cho, "Mid-infrared detectors in the 3-5 μm band using bound to continuum state absorption in InGaAs/InAlAs multiquantum well structures," *Applied Physics Letters*, Vol. 56, No. 8, pp. 770-772, 1990.

[33] Atakan Konukbay, "Design of a Voltage Tunable Broadband Quantum Well Infrared Photodetector," Master Thesis, Naval Postgraduate School, Monterey, CA, June 2002.

[34] M. Z. Tidrow, Xudong Jiang, Sheng S. Li and K. Bacher, "A four-color quantum well infrared photodetector," *Applied Physics Letters*, Vol. 74, No. 9, pp. 1335-1337, 1999.

[35] B. F. Levine, K. K. Choi, C. G Bethea, J. Walker and R. J. Malik, " Quantum well avalanche multiplication initiated by 10 μm intersubband absorption and photoexited tunneling," *Applied Physics Letters*, Vol. 51, No. 4, pp. 934-936, 1988.

[36] R. P. Karunasiri, J. S. Park and K. L. Wang, " Progress of SiGe/Si Quantum Wells for Infrared Detection," in *Thin Films*, Vol. 21, pp. 77-112, Academic Press Inc., San Diego, 1995.

[37] E. L. Dereniak and G. D Boreman, *Infrared Detector and Systems*, pp. 459-485, John Willey & Sons Inc., New York, 1996.

[38] S. Bandara, G. Gunapala, J. Liu, J. Mumolo, E. Luong, W. Hong and D. Sengupta, "Quantum Well infrared photodetectors: device physics and light coupling," in *Intersubband Transitions in Quantum Wells: Physics and Devices*, Sheng S. Li and Yan-Kuin Su, eds., pp. 43-49, Kluwer Academic Publishers, Massachusetts, 1998.

[39] B. F. Levine, C. G. Bethea, G. Hasnain, V. O. Shen, E. Pelve, R. R. Abbot and S. J. Hsieh, "High sensitivity low dark current 10 μm GaAs quantum well infrared photodetectors," *Applied Physics Letters*, Vol. 56, No. 9, pp. 851-853, 1990.

[40] Zhou Lifu, "Fabrication of quantum well detector array for thermal imaging," Master Thesis, pp. 37-52, National University of Singapore, 2001.

[41] S. D. Gunapala and S. V. Bandara, "Quantum Well Infrared Photodetectors (QWIP) Focal Plane Arrays" in *Intersubband Transitions in Quantum Wells: Physics and Devices*, Sheng S. Li, and Yan-Kuin Su, eds., pp. 197-278, Kluwer Academic Publishers, Massachusetts, 1998.

[42] Danhong Huang and M.O. Manasreh, "Intersubband transitions in a triple-couple quantum wells for three-colors infrared detectors," *Journal of Applied Physics*, Vol. 80, No. 10, pp. 6045-6049, 1996.

[43] E. F. Shubert, Notes for ECSE-6968 (Quantum Mechanics Applied to Semiconductor Devices), Rensselaer Polytechnic Institute, October, 2004 (unpublished).

[44] Y. Gusanov, E. Finkman, G. Bahir and D. Ritter, "The effect of strain in InP/InGaAs quantum-well infrared photodetectors on the operating wavelength," *Applied Physics Letters*, Vol. 79, No. 16, pp. 2508-2510, 2001.

[45] Sadao Adachi, *Physical Properties of III-V Semiconductor Compounds*, pp. 96-109, John Wiley & Sons, Inc., New York, 1992.

[46] H. C. Chui, S. M. Lord, E. Marinet, M. M. Fejer and J. S. Harris Jr., "Intersubbad transitions in high indium content InGaAs/AlGaAs quantum wells," *Applied Physics Letters*, Vol. 63, No. 3, pp. 364-366, 1993.

[47] H. C. Chui, E. Marinet, M. M. Fejer and J. S. Harris Jr., "Short wavelength intersubbad transitions in InGaAs/AlGaAs quantum wells grown on GaAs," *Applied Physics Letters*, Vol. 64, No. 6, pp. 736-738, 1994.

[48] G. Sarusi, B. F. Levine, S. J. Pearton, K. M. S. Bandara and R. E. Leibenguth, "Optimization of two dimensional gratings for very long wavelength quantum well infrared photodetedctors," *Journal of Applied Physics*, Vol. 76, No. 9, pp. 4989-4994, 1994.

[49] J. Y. Anderson and L. Lundqvist, " Near-unity quantum efficiency of AlGaAs/GaAs quantum well infrared detectors using waveguide with a doubly periodic grating coupler," *Applied Physics Letters*, Vol. 59, No. 7, pp. 857-859, 1991.

[50] K. L. Tsai, C. P. Lee, J. S. Tsang, H. R. Chen, and K. H. Chang, "Two-Dimensional Bi-Periodic Grating Coupled One- and Two-Color Quantum Well Infrared Photodetectors," *IEEE Electron Device Letters*, Vol. 16, No. 2, pp.49-51, 1995.

[51] M. P. Thouse, G. Karunasiri, K. R. Lantz, H. Li and T. Mei, " Near- and mid-infrared detection using GaAs/InxGa1-xAs/InyGa1-yAs multiple step quantum wells," *Applied Physics Letters*, Vol. 86, No. 9, pp. 093501/1-3, 2005.

[52] C. F. Gerald and P. O. Wheatley, *Applied Numerical Analysis*, pp. 330-339, Pearson Education Inc., Boston, 2004.

[53] Clayton L. Workman, "Intersubband Transitions in Strained InGaAs Quantum Well for Multi-color Infrared Detector Applications," PhD Thesis, pp. 62-86, University of Arkansas, 2000.

[54] F.Y. Huang, J. Li, Lie-Ming Li and H. Morcoc, "Self-consistent simulation of Stark shift of intersubband transition in modulation-doped step quantum wells," *Applied Physics Letters*, Vol. 63, No. 12, pp. 1669-1671, 1993.

[55] J. Y Anderson and L. Lundiqvist, "Grating-coupled quantum-well infrared detectors: Theory and performance," *Journal of Applied Physics*, Vol. 71, No. 7, pp. 3600-3610, 1992.

[56] S. O. Kasap, *Optoelectronics and Photonics, Principles and Practices*, pp. 1-44, Prentice Hall Inc., New Jersey, 2001.

[57] Martin Byloos, from the National Research Council, Canada, private telephone conversations, July, 2005.

THIS PAGE INTENTIONALLY LEFT BLANK

INITIAL DISTRIBUTION LIST

1.   Defense Technical Information Center
        Ft. Belvoir, Virginia

2.   Dudley Knox Library
        Naval Postgraduate School
        Monterey, California

3.   Pror. Jeff Knorr
        Naval Postgraduate School
        Monterey, California

4.   Prof. John Powers
        Naval Postgraduate School
        Monterey, California

5.   Prof. Gamani Karunasiri
        Naval Postgraduate School
        Monterey, California

6.   Prof. Sherif Michael
        Naval Postgraduate School
        Monterey, California